

**ULTRAFAST OPTICAL SWITCHING
IN THREE-DIMENSIONAL
PHOTONIC CRYSTALS**

**Ultrasnel optisch schakelen
in driedimensionale fotonische kristallen**



Universiteit Utrecht

**ULTRAFAST OPTICAL SWITCHING
IN THREE - DIMENSIONAL
PHOTONIC CRYSTALS**

**Ultrasnel optisch schakelen
in driedimensionale fotonische kristallen**

(met een samenvatting in het Nederlands)

PROEFSCHRIFT

TER VERKRIJGING VAN DE GRAAD VAN DOCTOR AAN
DE UNIVERSITEIT UTRECHT OP GEZAG VAN DE RECTOR
MAGNIFICUS, PROF. DR. W. H. GISPEN, INGEVOLGE
HET BESLUIT VAN HET COLLEGE VOOR PROMOTIES
IN HET OPENBAAR TE VERDEDIGEN OP MAANDAG
6 SEPTEMBER 2004 DES MIDDAGS TE 14.30 UUR

DOOR

Dmitry Anatolievich Mazurenko

geboren op 26 Januari 1974 te Leningrad, USSR

PROMOTOR: PROF. DR. J. I. DIJKHUIS

FACULTEIT DER NATUUR- EN STERRENKUNDE
UNIVERSITEIT UTRECHT

CIP-DATA KONINKLIJKE BIBLIOTHEEK, DEN HAAG

Mazurenko, Dmitry Anatolievich

ULTRAFAST OPTICAL SWITCHING
IN THREE-DIMENSIONAL PHOTONIC CRYSTALS

Dmitry Anatolievich Mazurenko – Utrecht: Universiteit Utrecht,

Faculteit der Natuur- en Sterrenkunde

Thesis Universiteit Utrecht – with a summary in Dutch

ISBN 090-393-3772-1

CONTENTS

1	Introduction	11
1.1	Photonic crystals: novel optical phenomena and applications . . .	11
1.2	History	12
1.3	Fabrication methods	13
1.3.1	Artificial opals	15
1.4	Tunable photonic crystals	15
1.5	Outline of this thesis	19
	Bibliography	21
2	Experimental details	27
2.1	Introduction	27
2.2	Experimental setup with high temporal resolution	28
2.2.1	Experimental setup with high repetition rate	28
2.2.2	Double modulation technique	30
2.2.3	Linear reflection	31
2.3	Experimental setup with low repetition rate	32
	Bibliography	34
3	Optical switching in opal-Si	35
3.1	Introduction	35
3.2	Ultrafast dynamics in bulk silicon	36
3.3	Sample and experimental details	39
3.4	Experimental results	40
3.4.1	Linear reflectance	40
3.4.2	Transient changes in reflectance	41
3.5	Theory	42
3.6	Discussion	46

3.7	Experiments with high excitation power density	49
3.7.1	Linear optical properties of the second-order photonic stop band	49
3.7.2	Optical switching at high optical excitation	50
3.8	Conclusions	51
	Bibliography	51
4	Shifting of a stop-band induced by an ultrafast phase transition in vanadium dioxide	53
4.1	Introduction	53
4.2	Ultrafast phase transitions in solids	54
4.3	Phase transition in VO ₂	56
4.4	Opal-VO ₂ and experimental details	57
4.5	Ultrafast band-shifting	59
4.5.1	Linear optical properties	59
4.5.2	Nonlinear optical properties	60
4.6	Discussion	62
4.7	Conclusion	65
	Bibliography	65
5	Linear optical properties of a core-shell silica-gold photonic crystal	69
5.1	Introduction	69
5.2	Sample and experimental details	72
5.3	Experimental results	74
5.3.1	Reflection from a single hexagonal layer of gold-shell particles	75
5.3.2	Reflection from a multi-layer gold-shell photonic crystal	76
5.4	Theory	77
5.4.1	Layered KKR method	78
5.4.2	Computation results	82
5.5	Discussion	84
5.6	Conclusions	88
	Bibliography	88
6	Ultrafast dynamics in a silica-gold core-shell photonic crystal	91
6.1	Introduction	91
6.2	Experimental details	92
6.2.1	Time-resolved detection of the reflectivity spectra	92

6.2.2	High-selectivity pump-probe detection at a specific wavelength	93
6.3	Ultrafast response of the gold-shell photonic crystal	94
6.4	Nature of the ultrafast changes in reflectivity	95
6.5	Calculation of the transient reflectivity	96
6.5.1	Ultrafast dynamics in gold	96
6.5.2	Two-temperature model	98
6.5.3	Calculation of the transient reflectivity	100
6.5.4	Temperature dependence of the dielectric constant of gold	102
6.5.5	Comparison of the experiment and calculations results	103
6.6	Irreversible changes following excitation above the threshold limit	105
6.7	Conclusions	106
	Bibliography	107
7	Coherent vibrations of submicron gold shells	109
7.1	Introduction	109
7.2	Coherent excitation of acoustic modes	110
7.3	Interpretation of the experimental results	112
7.4	Lamb modes	113
7.4.1	Eigenfrequencies of a solid sphere	114
7.4.2	Eigenfrequencies of a spherical shell	115
7.5	Ringling in a hollow sphere: selection rules.	117
7.6	Nature of the optical response	120
7.7	Origin of the damping of acoustic vibrations	122
7.8	Conclusions and perspectives	123
	Bibliography	123
	Samenvatting	125
	Acknowledgements	129
	List of Publications and Conference Visits	133
	Curriculum Vitae	135

CHAPTER 1

INTRODUCTION

1.1 Photonic crystals: novel optical phenomena and applications

Structures with a periodically modulated index of refraction, so-called *photonic crystals*, have unusual optical properties. Multiple interference of light on a periodic lattice leads to a *photonic stop band* (PSB) and anomalous dispersion [1] because light with a wavelength close to the period of modulation cannot propagate in certain directions [2]. Photonic structures can be found in nature. For example, the beautiful coloration of the Morpho butterfly's wings is caused by a periodic submicron structure within the scale [3, 4]. Of similar origin is the spectacular iridescence of a spine from the sea mouse that produces bright colors with changing the angle of observation [5]. Another famous example of a natural photonic crystal is natural opal [6] with the shining optical properties that are described below.

Photonic crystals are special due to their fundamental optical properties and allow us to test unusual regimes of light propagation. Recent experimental observations demonstrate among others extremely large group-velocity dispersion [7], extraordinary angle-sensitive light propagation [8], slowing down of the pulse of light [9], anomalous coherent backscattering of light [10], optical gap soliton formation in nonlinear photonic crystals [11, 12], anomalously high transmission through an array of sub-wavelength holes in a metal film [13], and highly directional beaming of light propagating through a hole in a periodically corrugated metallic film [14].

Another quite unique fundamental optical property may be realized in so-called left-handed materials, where both the effective permittivity and effective permeability are negative. It was proposed that such left-handed materials may be created on the basis of a so-called metallo-dielectric photonic crystal [15, 16]. Left-handed materials were introduced by Veselago [17] but were already dis-

cussed earlier by Schuster [18] and Sivukhin [19]. As was pointed out by these authors, the propagation of electromagnetic waves in such kind of materials is possible, but the wavevector, the electric field vector, and magnetic field vector form a left-handed set instead of a right-handed one, which is the case in usual materials. As a result, the Poynting vector and wavevector point in opposite directions and the refractive index is negative. This implies that the electromagnetic wave at the interface between positive and negative refractive index materials should refract in opposite directions relative to the normal situation (negative refraction). The phenomenon of negative refraction was recently demonstrated experimentally [20]. However, the question of the existence of negative refraction in left-handed materials is currently under controversial debate [21, 22]. A quarter of a century ago Silin [23] proposed to use left-handed materials for fabricating plane-parallel lenses that are free of aberrations. Recently, Pendry [24] revealed another fascinating property of these lenses, namely plane-parallel lenses with a negative refractive index that surpass the limit of conventional lenses and are capable to form an image with subwavelength resolution. This challenging idea has been recently tested experimentally in a two-dimensional dielectric photonic crystal [20].

Less controversial potential applications of photonic crystals include ultrafast optical switches, reconfigurable optical networks, holographic memories, low-threshold lasers, optical computers, and novel types of harmonic generators [25, 26]. Some of them, e.g. low-threshold lasing in one- [27], two- [28], and three-dimensional [29] photonic crystals, have already been demonstrated and others are even commercially available at present such as dielectric mirrors and photonic crystal fibers [30]. We finally mention that photonic structures made of tungsten were recently proposed for enhancing a quantum efficiency of bulb lamps [31, 32].

1.2 History

The study of the photonic crystals in fact has a long history in science. Perhaps, the first person who ever systematically studied the propagation of waves in a periodic structure was Lord Rayleigh [33]. In 1946 Purcell [34] proposed that spontaneous emission of atoms should be significantly altered in an optical resonator. His idea was developed further by Bykov [35] who suggested in 1972 to control spontaneous emission in a one-dimensional photonic crystal. His idea can be illustrated by considering an atom placed in a one-dimensional photonic crystal (see Fig. 1.1). Now, if a spontaneous emission frequency is chosen to fall into the PSB of the photonic crystal, the atom will be unable to emit light in the directions perpendicular the planes of photonic crystal simply because there are

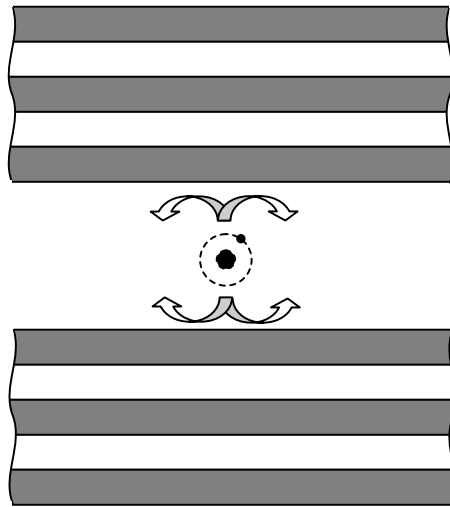


FIGURE 1.1 Inhibition of spontaneous emission in a photonic crystal.

no travelling electromagnetic states available to which light can escape and the spontaneous emission rate must change. In 1987 Jablonovitch and John [36, 37] pointed out that spontaneous emission must even vanish completely in case of a three-dimensional (3D) photonic crystal if the frequency of the atom happens to fall into a photonic band gap – a spectral range where light cannot propagate in *any* direction. A photonic crystal with a complete band gap in the microwave range was created already in 1991. The structure was fabricated by drilling holes in high-refractive-index material. However, it appeared to be far from trivial to reach a full photonic band gap in the visible spectral range. This was achieved only recently [38–40]. The reason is that one needs a sufficiently high refractive index contrast between the composed materials of a photonic crystal. For example, a close-packed face-centered-cubic (fcc) lattice requires a refractive index contrast higher than 2.8 (Refs. [41, 42]). Recently, control over light emission in 3D photonic crystals was demonstrated experimentally [43–45].

1.3 Fabrication methods

There exist a large number of methods to fabricate 3D photonic crystals with a lattice parameter of the order of a wavelength of visible light. Here we emphasize the three most common ones: holographic microfabrication, “layer-by-layer”

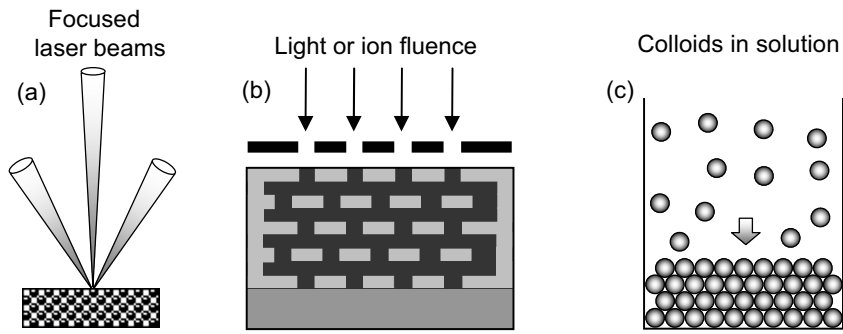


FIGURE 1.2 Fabrication of three-dimensional photonic crystals. (a) Holographic microlithography: photonic structure is created by interference of laser beams in photo-sensitive material and subsequent etching. (b) "Layer-by-layer" fabrication: each layer is created by light or ion beam and suitable mask. (c) Self-assembly of colloids in solution

fabrication, and self-assembly (see Fig. 1.2). The most precise and straightforward method is a femtosecond laser holographic microfabrication [46–48]. The idea of this method is shown in Fig. 1.2(a). Here, the photonic crystal lattice is constructed by a volume interference of several femtosecond laser beams in a photo-sensitive material that is subsequently etched. However, disadvantages of this method include the limited number of materials that can be used for the laser etching and the expensive and rather complicated setup. Unfortunately, most of those materials, have a low refractive index that decreases the possibilities to realize a complete photonic band gap.

In contrast, the direct "layer-by-layer" fabrication method [49, 50] is flexible in relation to the choice of materials and allow for the manufacturing of photonic structures with a very complicated topology [see Fig. 1.2(b)]. The disadvantage of this approach is the time needed for fabrication of reasonably thick 3D photonic structure, and the costs.

Self-assembly of colloidal spheres [38, 39, 51] seems nowadays the most promising way to create 3D photonic crystals with thicknesses of up to hundreds of microns and higher [see Fig. 1.2(c)]. It is cheap and much simpler than the other approaches. The main disadvantage of this method is that it is hard to avoid the appearance of considerable amounts of lattice defects during the fabrication, which may destroy the photonic band gap [52]. Recently, fabrication of ordered arrays of ice [53], titania [54], zinc sulfide [55, 56], gold core-shell particles [57], and other 3D photonic crystals were reported. In this thesis we will exclusively use artificial opals fabricated by self-assembly.

1.3.1 Artificial opals

Opal, a precious stone with a beautiful coloration, is probably the most famous natural photonic crystal [6]. An opal usually consists of an ordered close-packed fcc array of monodisperse silica spheres with a diameter of the order of hundreds of nanometers [58]. As a result, the refractive index is modulated in space on the scale of the wavelength of light. The spectral position of the first-order PSB in such an opal can be roughly estimated from Bragg's law,

$$\lambda = 2d \sqrt{\bar{\varepsilon} - \sin^2 \theta}, \quad (1.1)$$

where λ is the wavelength of light in vacuum, d the lattice period, θ angle of incident light with respect to the plane of opal, $\bar{\varepsilon}$ the average-volume dielectric constant of the opal, defined as the volume integral over the unit cell,

$$\bar{\varepsilon} = \frac{1}{V} \int_V \varepsilon(\mathbf{r}) d^3 \mathbf{r}. \quad (1.2)$$

More accurate formula can be found in a work of Moroz [59].

The spectral width of the PSB is dependent on refractive index contrast and can be changed by filling the voids of opal with suitable substances [60]. Modern technology allows to fill opal voids with various dielectrics [61], semiconductors [38, 60], liquid crystals [62], and metals [63]. As an example, Fig. 1.3 shows a transmission electron microscopy (TEM) image of opal partly filled with silicon.

1.4 Tunable photonic crystals

One of the most promising ideas is to use photonic crystal as the base material for integrated optical circuits. The speed of these circuits are expected to surpass that of traditional electronic devices because of the high velocity of the electromagnetic signals comparing with that of electrons. Since the key function in circuits is switching, it is desirable to fabricate a photonic crystal with tunable optical properties. The idea is to rapidly change the energy position of the PSB of the photonic crystal and switch the channel for light propagation in specific directions, by applying an external impact. To achieve all-optical switching in photonic crystals, precise knowledge and control of the ultrafast non-linear properties is a prerequisite. In this thesis we analyze the ultrafast non-linear properties of three types of 3D photonic materials, one based on opal filled with silicon, one on opal filled with vanadium dioxide, and one on an array of close-packed mul-

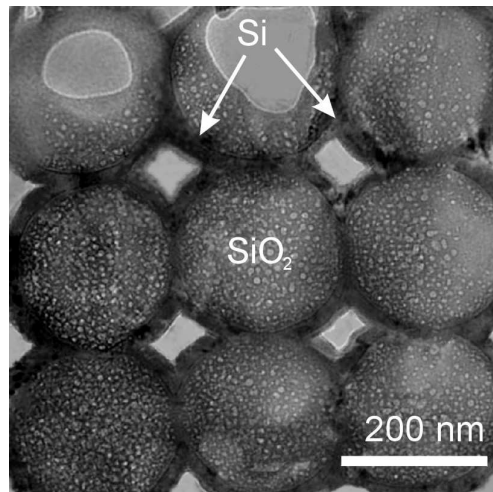


FIGURE 1.3 TEM image of an annealed opal-Si sample taken in diffraction contrast mode. Picture is copied from Ref. [64]

tishells composed of a spherical silica core surrounded by a thin gold shell and silica outer shell.

The control over the PSB can be realized via the modification of the effective complex dielectric constant of the photonic crystal, $\tilde{\epsilon} = \tilde{\epsilon}' + i\tilde{\epsilon}''$. Here, one can distinguish effects on the modulation of $\tilde{\epsilon}'$ that shifts the spectral position of the PSB, and ones that increase $\tilde{\epsilon}''$ that suppresses interference of light inside the photonic crystal and diminishes the interference effects in the PSB. The dynamic shift of the spectral location of a PSB was first analyzed for the case of a one-dimensional photonic crystal [25]. As noted above, in one-dimensional photonic crystals, light propagation is only frustrated in limited directions and changes reached in the photonic density of states are small. Complete dynamic control over the photonic density of states is only possible in 3D photonic structures [36]. Shifting of the photonic bands can be achieved by applying external electric fields, magnetic fields, temperature variation, pressure, or via optical excitation.

(I) Band-tuning by an external electric field. To use external electric fields for tuning PSBs was proposed by Tran [65] in 1995. The tuning can be achieved via the Kerr [65] and Pockels [66] non-linearity. However, to achieve substantial band shifts, this method requires rather high electric fields that are not easy to realize. An important practical scheme that exploits the Kerr nonlinearity was devised by Busch and John [67]. They suggested to fill the void spaces of an opal by

optically birefringent nematic liquid crystals, whose optical properties are known to be quite sensitive to the presence of external electric fields. This idea resulted in extensive experimental investigations and practical implementation followed a few years later [68–71]. An alternative method is to use ferroelectric materials, which was recently demonstrated by Li and co-authors for a ferroelectric inverse opal [72].

(II) Band-tuning by an external magnetic field. Magnetic photonic crystals [73] allow for several methods of PSB control by external magnetic fields. One of them, band-tuning via field dependence of the permeability was discussed in a recent review [74]. A quite different magnetic mechanism has been demonstrated by Saado and co-workers [75] in a 3D photonic crystal composed of metal coated disk-shaped magnetic particles floating at a liquid-air interface. They showed that the lattice constant of an ordered array of these magnetic particles can be controlled by an external magnetic field. Finally, Xu and co-authors pointed out [76] that an external magnetic field can tune the dielectric constant of semiconductor photonic crystals via the magneto-optic effect.

(III) Band-tuning by a temperature variation. Band tuning in three-dimensional photonic crystals via the ambient temperature was first demonstrated in liquid crystal materials [62, 77, 78]. Large band shifts were also shown in opals filled with a suitable material exhibiting a phase transition in a convenient temperature range. When temperature reaches the transition point, the effective refractive index of the photonic crystal abruptly changes and a PSB shifts. Recently, PSB shifting, assisted by a ferroelectric phase transitions, has been experimentally demonstrated [79]. However, the largest shift of a PSB in 3D photonic crystals, was observed in a photonic crystal built from an opal filled with VO₂ [80] that exhibits a semiconductor-metal phase transition. At the phase transition, the change in the effective refractive index of the opal results in PSB shifts of 40-nm [81]. The opal-VO₂ structure can even be inverted by etching away the silica spheres, which further increases the feasible PSB shift.

(IV) Band-tuning by an elastic strain. Strain-induced band-tuning in a piezoelectric photonic crystal was analyzed by Kim and Gopalan [82]. In their approach a field driven strain distorts the symmetry of the photonic crystal from a regular hexagonal to a quasihexagonal lattice resulting in a band shift. Recently, tuning the photonic band by stretching was studied for the particular case of an inverted fcc opal structure [83]. The first experimental evidence of a strain-induced change in a photonic band structure was reported by Yoshino and co-workers [84]. They observed a reversible red shift of a PSB along the [1 1 1] direction of a polymer opal under static mechanical stress applied in the perpendicular direction.

In contrast, a blue shift of the [1 1 1] PSB was observed for pressure applied in the parallel direction [85]. These phenomena can be explained by elongation and contraction of the lattice in the [1 1 1] direction depending on the directions of the applied uniaxial stresses. However, a photonic crystal lattice is fragile and can be easily destructed even by moderate pressures. For example, irreversible changes in polystyrene opals were already registered at 10 MPa [86]. It is interesting to note that a dynamic shift of a PSB can be induced by a propagating strain-wave. Recently, Reed and co-authors [87] pointed out that a shock wave moving through a photonic crystal may even result in a very interesting and intriguing optical phenomenon: the reversed Doppler effect. However, up to now, fast strain-induced shift of a photonic gap has not been demonstrated yet and remains a challenge for experimentalists. In Chapter 7, we show that coherently excited standing strain-waves induce large changes in the reflectivity of a 3D core-shell metallo-dielectric photonic crystal suggesting that the strain-wave induced switching is feasible. However, the rate of the strain-wave-induced shifting is obviously limited by the oscillation frequency of the propagated strain-waves with a wavelength of the order of the photonic crystal lattice parameter. In case of PSB's in the visible spectral range, the switching time will thus be on the order of tens picoseconds or longer.

Unfortunately, tuning a PSB by an external electric field, a magnetic field, temperature variations, or dynamical tensions takes place on an unpractically long time scales. The by far fastest way of band-tuning would be by femtosecond excitation.

(V) Band-tuning by optical excitation. The dynamic shift of the PSB induced by the action of the optical nonlinearity was first analyzed by Scalora and co-workers in one-dimensional photonic crystals [25], the theory was extended for the case of two [88] and three dimensions [89, 90]. The first optically induced switching in a 3D photonic crystal was observed in crystalline colloidal arrays of dyed poly-spheres on the nanosecond timescale [91]. Later, distinct changes in reflectivity induced by nanosecond optical pulses were reported in opals filled with vanadium dioxide [92] (VO_2). In this experiment the induced shift of the PSB was associated with a heat-induced phase transition of the VO_2 . However, band-shifting via optical free-carrier excitation was predicted to be much faster [90]. Recently, optical nonlinearity on a picosecond time scale was registered both in an opal filled with carbon nanotubes [93] and in an array of ordered polystyrene spheres [94]. At the same time, the required conditions for efficient band-shifting are conflicting. On the one hand, one has to optimize the PSB properties, implying that the photonic crystal should be non-absorbing. On the other hand, one

needs to create free-carriers via optical absorption. One solution to this problem is to use two-photon absorption in transparent materials and another is to choose weakly absorbing materials for free-carrier excitation. These ideas were implemented for ultrafast band-tuning in one- [95] and two-dimensional [96] silicon structures and in two-dimensional AlGaAs photonic crystals [97]. In silicon photonic crystals free carriers were excited via infrared two-photon absorption, while in AlGaAs photonic crystals, carriers were excited by weak absorption at the edge of the electronic bandgap of AlGaAs.

1.5 Outline of this thesis

This thesis explores the potential of ultrafast control over the propagation of light in three-dimensional photonic crystals by ultrashort optical pulses. In our approach, the tuning of PSBs is triggered by femtosecond optical pulses that rapidly modify the mean dielectric constant of the photonic crystal. As a result, reflectivity and transmission of the photonic crystal change with a speed and to a degree depending on the duration and power of an optical excitation and the materials that form the photonic crystal. In this thesis we analyze various schemes for all-optical switching. In opal-Si composites, the optical nonlinearity is induced by photoexcited free carriers (Chapter 3), in the opal-VO₂ composites by an optically induced phase transition of vanadium dioxide (Chapter 4), in a silica-gold core-shell photonic crystal by heating the free-electron gas in the gold shells (Chapter 6), and, finally, in the same sample by impulsive mechanical expansion of the material (Chapter 7). We show that in all demonstrated schemes (except those induced by the mechanical expansions as discussed in Chapter 7) optical switching in 3D photonic crystals occurs on the subpicosecond time scale. We also point out that depending on whether the real or the imaginary part of the mean dielectric constant of a photonic crystal is affected, the PSB switching occurs in quite different fashions: In Chapter 3 and Chapter 4, we show that in case the imaginary part increases the PSB effects weaken, while in case the real part of the dielectric constant is changed the spectral position of a PSB shifts. This thesis is organized as follows:

In Chapter 2, we describe two pump-probe setups used for our ultrafast dynamic optical measurements. Standard pump-probe setups are extended with two features that are not commonly used, e.g. a phase modulation to avoid interference between pump and probe optical pulses and increase the sensitivity, and the possibility to separate the specular reflected beam from the surface of the photonic crystal, and the diffracted beam from the photonic crystal lattice. The latter

procedure has not been used in earlier dynamic experiments, but turns out to be very important to be able to study the dynamical optical properties of finite photonic crystals. The reason is that the surface specular reflection and the volume diffracted reflection have a completely different nature and, as a consequence, respond in a quite different fashion to the optical excitation.

In Chapter 3, we demonstrate ultrafast switching of the PSB in an opal-silicon composite. In this photonic crystal the optical nonlinearity is governed by photoexcited carriers and appears instantaneously with the optical excitation. The special design of our pump-probe setup allows us to separate the contribution of ordinary transient surface reflection from those of the transient Bragg reflectivity originating from the volume of the photonic crystal. By analyzing the changes in the Bragg reflection at different wavelengths, we arrive to the conclusion that the changes in PSB spectra are governed by photoinduced absorption, i.e. by the transient modification of the *imaginary* part of the effective dielectric constant of the opal-silica photonic crystal. The obtained experimental results are compared with calculations made in the framework of “two-band mixing” theory.

In Chapter 4, we show the second type of switching of a PSB, namely in opal filled with vanadium dioxide. In this sample the optical switching is triggered by an optically induced ultrafast phase transition in vanadium dioxide that produces a shift of the spectral position of a PSB on the subpicosecond time scale. In contrast to the experiment of Chapter 3, optical excitation leads to changes of predominantly the *real* part of the effective dielectric constant of the photonic crystal.

In Chapter 5, we introduce metallo-dielectric photonic crystals, which turn out to be more complicated. Here, the interplay between surface plasmons and the periodic structure of the photonic crystal, results in the appearance of quite interesting phenomena already in the linear regime. We study the linear optical phenomena in a recently fabricated 3D photonic crystal composed of silica-core gold-shell spheres. The interference between the surface plasmon resonances of the individual spheres and enhanced interparticle interaction of the photonic arrangement results in quite complicated reflection spectra in the visible spectral range. We analyze these spectra and attempt to classify the observed reflection maxima and minima. We also compare the measured spectra with the *ab-initio* calculated ones using the so-called photonic Karringa-Kohn-Rostocker method. We further find evidence of beaming of the diffracted light on a single layer, in the form of the observed hexagonal diffraction pattern with divergence angles as small as 8° . This effect can be traced back to interference between surface plasmons and propagating surface waves.

In Chapter 6, we study the non-linear picosecond dynamics of the metallo-dielectric photonic crystal. Depending on the selected wavelength, we observe both transient absorption and bleaching on the subpicosecond time scale. We attribute the observed changes to photoinduced absorption in gold and the resulting broadening of the plasmon resonance. The observed dynamics is analyzed in the framework of the so-called “two-temperature model”.

In Chapter 7, we finally analyze the dynamics of the silica-core gold-shell photonic crystal on the subnanosecond timescale. We discovered that the reflectivity is strongly affected by standing-wave acoustic vibrations in the form of coherent expansions and contractions of the gold shell. This observation, perhaps, forms the bridge between *photonic* and *phononic* crystals, in which the acoustic wave instead of the light wave undergoes resonant scattering on a periodic lattice. The detected period of the acoustic oscillations was found to be in perfect agreement with the vibration period of thin free spherical gold shells calculated in the framework of Lamb theory. To best of our knowledge, this is the first demonstration of acoustic vibrations of a free nanoscale shell detected in a pump-probe experiment. Furthermore, this result can be relevant for switching photonic crystals by strain waves.

Our studies form a step towards complete ultrafast control over the dynamical optical properties of three-dimensional photonic crystals. We demonstrate that already at the present level of technology, the switching in a three-dimensional photonic crystals can be made as fast as several tens of femtoseconds with the efficiency of 50% and higher.

References

- [1] A. Imhof, W. L. Vos, R. Sprik, and A. Lagendijk, *Phys. Rev. Lett.* **83**, 2942 (1999).
- [2] C. M. Soukoulis, *Photonic Crystals and Light Localization in the 21st Century*, vol. 653 of *Nato Advanced Studies Institute, Series C: Mathematical and Physical Sciences* (Kluwer, Dordrecht, 2001).
- [3] P. Vukusic, J. R. Sambles, C. R. Lawrence, and R. J. Wootton, *Proc. R. Soc. Lond. B* **266**, 1403 (1999).
- [4] S. Kinoshita, S. Yoshioka, and K. Kawagoe, *Proc. R. Soc. Lond. B* **269**, 14171421 (2002).
- [5] A. R. Parker, R. C. McPhedran, D. R. McKenzie, L. C. Botten, and N.-A. P. Nicorovici, *Nature (London)* **409**, 36 (2001).
- [6] J. V. Sanders, *Nature (London)* **204**, 1151 (1964).
- [7] M. Notomi, K. Yamada, A. Shinya, J. Takahashi, and I. Yokohama, *Phys. Rev. Lett.* **87**, 253902 (2001).

-
- [8] H. Kosaka, T. Kawashima, A. Tomita, M. Notomi, T. Tamamura, T. Sato, and S. Kawakami, *Phys. Rev. B* **58**, R10096 (1998).
- [9] Y. Vlasov, S. Petit, G. Klein, B. Hönerlage, and C. Hirlimann, *Phys. Rev. E* **60**, 1030 (1999).
- [10] J. Huang, N. Eradat, M. E. Raikh, Z. V. Vardeny, A. A. Zakhidov, and R. H. Baughman, *Phys. Rev. Lett.* **86**, 4815 (2001).
- [11] B. J. Eggleton, R. Slusher, C. M. de Sterke, P. A. Krug, and J. E. Sipe, *Phys. Rev. Lett.* **76**, 1627 (1996).
- [12] J. W. Fleischer, M. Segev, N. K. Efremidis, and D. N. Christodoulides, *Nature (London)* **422**, 147 (2003).
- [13] T. W. Ebbesen, H. J. Lezec, H. F. Ghaemi, T. Thio, and P. A. Wolff, *Nature (London)* **391**, 667 (1998).
- [14] H. J. Lezec, A. Degiron, E. Devaux, R. A. Linke, L. Martín-Moreno, F. J. Garcia-Vidal, and T. W. Ebbesen, *Science* **297**, 820 (2002).
- [15] D. R. Smith, D. C. Vier, W. Padilla, S. C. Nemat-Nasser, and S. Schultz, *Appl. Phys. Lett.* **75**, 1425 (1999).
- [16] D. R. Smith, W. J. Padilla, D. C. Vier, S. C. Nemat-Nasser, and S. Schultz, *Phys. Rev. Lett.* **84**, 41844187 (2000).
- [17] V. G. Veselago, *Usp. Fiz. Nauk* **92**, 517 (1967), [*Sov. Phys. Usp.* 10, 509 (1968)].
- [18] A. Schuster, *An Introduction to the Theory of Optics* (Edward Arnold, London, 1904), p. 313.
- [19] D. V. Sivukhin, *Opt. Spektrosk.* (in Russian) **3**, 308 (1957).
- [20] R. A. Shelby, D. R. Smith, and S. Schultz, *Science* **292**, 7779 (2001).
- [21] P. M. Valanju, R. M. Walser, and A. P. Valanju, *Phys. Rev. Lett.* **88**, 187401 (2002).
- [22] S. Foteinopoulou, E. N. Economou, and C. Soukoulis, *Phys. Rev. Lett.* **90**, 107402 (2003).
- [23] R. A. Silin, *Opt. Spektrosk.* **44**, 109 (1978), [*Opt. Spektrosk. USSR* 44, 189 (1978)].
- [24] J. B. Pendry, *Phys. Rev. Lett.* **85**, 3966 (2000).
- [25] M. Scalora, J. P. Dowling, C. M. Bowden, and M. J. Bloemer, *Phys. Rev. Lett.* **73**, 1368 (1994).
- [26] V. Berger, *Phys. Rev. Lett.* **81**, 4136 (1998).
- [27] V. I. Kopp, B. Fan, H. K. M. Vithana, and A. Z. Genack, *Opt. Lett.* **23**, 1707 (1998).
- [28] O. Painter, R. K. Lee, A. Scherer, A. Yariv, J. D. O'Brien, P. D. Dapkus, and I. Kim, *Science* **284**, 1819 (1999).
- [29] W. Cao, A. Muoz, P. Palfy-Muhoray, and B. Taheri, *Nature Materials (London)* **1**, 111 (2002).
- [30] P. S. J. Russell, *Science* **299**, 358 (2003).
- [31] J. G. Fleming, S. Y. Lin, I. El-Kady, R. Biswas, and K. M. Ho, *Nature (London)* **417**, 52 (2002).
- [32] S.-Y. Lin, J. G. Fleming, and I. El-Kady, *Appl. Phys. Lett.* **83**, 593 (2003).
- [33] L. Rayleigh, *Philos. Mag.* **34**, 481 (1892).
- [34] E. M. Purcell, *Phys. Rev.* **69**, 681 (1946).
- [35] V. P. Bykov, *Sov. Phys. JETP* **35**, 269 (1972).

- [36] E. Yablonovitch and T. J. Gmitter, Phys. Rev. Lett. **63**, 1950 (1989).
- [37] S. John, Phys. Rev. Lett. **58**, 2486 (1987).
- [38] A. Blanco, E. Chomski, S. Grabtchak, M. Ibisate, S. John, S. W. Leonard, C. Lopez, F. Meseguer, H. Miguez, J. P. Mondia, et al., Nature (London) **405**, 437 (2000).
- [39] Y. A. Vlasov, X. Z. Bo, J. C. Sturm, and D. J. Norris, Nature (London) **414**, 289 (2001).
- [40] E. Palacios-Lidón, A. Blanco, M. Ibisate, F. Meseguer, C. López, and J. Sánchez-Dehesa, Appl. Phys. Lett. **81**, 4925 (2002).
- [41] H. S. Sözüer, J. W. Haus, and R. Inguva, Phys. Rev. B **45**, 13962 (1992).
- [42] R. Biswas, M. M. Sigalas, G. Subramania, and K.-M. Ho, Phys. Rev. B **57**, 3701 (1998).
- [43] Y. A. Vlasov, K. Luterova, I. Pelant, B. Hönerlage, and V. N. Astratov, Appl. Phys. Lett. **71**, 1616 (1997).
- [44] M. J. A. de Dood, A. Polman, and J. G. Fleming, Phys. Rev. B **67**, 115106 (2003).
- [45] S. Ogawa, M. Imada, S. Yoshimoto, M. Okano, and S. Noda, Science **305**, 227 (2004).
- [46] M. Campbell, D. N. Sharp, M. T. Harrison, R. G. Denning, and A. J. Turberfield, Nature (London) **404**, 53 (2000).
- [47] M. Straub, M. Ventura, and M. Gu, Phys. Rev. Lett. **91**, 043901 (2003).
- [48] S. Shojia, H.-B. Sun, and S. Kawata, Appl. Phys. Lett. **83**, 608 (2003).
- [49] S. Y. Chou, C. Kelmel, and J. Gu, Nature (London) **417**, 835 (2002).
- [50] G. M. Gratson, M. Xu, and J. A. Lewis, Nature (London) **428**, 386 (2004).
- [51] A. van Blaaderen, K. P. Velikov, J. P. Hoogenboom, D. L. J. Vossen, A. Yathiraj, R. Dullens, T. van Dillen, and A. Polman, in *Photonic Crystals and Light Localization in the 21st Century*, edited by C. M. Soukoulis (Kluwer, Dordrecht, 2001), vol. 653 of *Nato Advanced Studies Institute, Series C: Mathematical and Physical Sciences*, p. 239.
- [52] A. F. Koenderink, Ph.D. thesis, Universiteit Amsterdam (2003).
- [53] S. H. Im and O. O. Park, Appl. Phys. Lett. **80**, 4133 (2002).
- [54] J. E. G. J. Wijnhoven, L. Bechger, and W. L. Vos, Chem. Mater. **13**, 4486 (2001).
- [55] K. P. Velikov, A. Moroz, and A. van Blaaderen, Appl. Phys. Lett. **80**, 49 (2002).
- [56] K. P. Velikov, Ph.D. thesis, Universiteit Utrecht (2002).
- [57] C. Graf, D. L. J. Vossen, A. Imhof, and A. van Blaaderen, Langmuir **19**, 6693 (2003).
- [58] Y. Xia, B. Gates, Y. Yin, and Y. Lu, Adv. Mater. **12**, 693 (2000).
- [59] A. Moroz, J. Opt. A : Pure Appl. Opt **1**, 471 (1999).
- [60] V. N. Astratov, V. N. Bogomolov, A. A. Kaplyanskii, A. V. Prokofiev, L. A. Samoilovich, S. M. Samoilovich, and Y. A. Vlasov, Il Nuovo Cimento **17 D**, 1349 (1995).
- [61] Y. A. Vlasov, V. N. Astratov, O. Z. Karimov, A. A. Kaplyanskii, V. N. Bogomolov, and A. V. Prokofiev, Phys. Rev. B **55**, R13357 (1997).
- [62] K. Yoshino, S. Saton, Y. Shimoda, Y. Kawagishi, K. Nakayama, and M. Ozaki, Jpn. J. Appl. Phys **38**, L961 (1999).

- [63] O. D. Velev, P. M. Tessier, A. M. Lenhoff, and E. W. Kaler, *Nature (London)* **401**, 578 (1999).
- [64] V. G. Golubev, J. L. Hutchison, V. A. Kosobukin, D. A. Kurdyukov, A. V. Medvedev, A. B. Pevtsov, J. Sloanc, and L. M. Sorokin, *J. Non-Cryst. Solid.* **299-302**, 1062 (2002).
- [65] P. Tran, *Phys. Rev. B* **52**, 10673 (1995).
- [66] H. Takeda and K. Yoshino, *Phys. Rev. E* **69**, 016605 (2004).
- [67] K. Busch and S. John, *Phys. Rev. Lett.* **83**, 967 (1999).
- [68] D. Kang, J. E. Maclennan, N. A. Clark, A. A. Zakhidov, and R. H. Baughman, *Phys. Rev. Lett.* **86**, 4052 (2001).
- [69] Q.-B. Meng, C.-H. Fu, S. Hayami, Z.-Z. Gu, O. Sato, and A. Fujishima, *J. Appl. Phys.* **89**, 5794 (2001).
- [70] Y. Shimoda, M. Ozaki, and K. Yoshino, *Appl. Phys. Lett.* **79**, 3627 (2001).
- [71] P. Mach, P. Wiltzius, M. Megens, D. A. Weitz, K.-H. Lin, T. C. Lubensky, and A. G. Yodh, *Phys. Rev. E* **65**, 031720 (2002).
- [72] B. Li, J. Zhou, L. Li, X. J. Wang, X. H. Liu, and J. Zi, *Appl. Phys. Lett.* **83**, 4704 (2003).
- [73] M. M. Sigalas, C. M. Soukoulis, R. Biswas, and K. M. Ho, *Phys. Rev. B* **56**, 959 (1997).
- [74] B. Gates and Y. Xia, *Adv. Mater.* **13**, 1605 (2001).
- [75] Y. Saado, M. Golosovsky, D. Davidov, and A. Frenkel, *Phys. Rev. B* **66**, 195108 (2002).
- [76] C. Xu, X. Hu, Y. Li, X. Liu, R. Fu, and J. Zi, *Phys. Rev. B* **68**, 193201 (2003).
- [77] K. Yoshino, Y. Shimoda, Y. Kawagishi, K. Nakayama, and M. Ozaki, *Appl. Phys. Lett.* **75**, 932 (1999).
- [78] G. Mertens, T. Röder, R. Schweins, K. Huber, and H.-S. Kitzerow, *Appl. Phys. Lett.* **80**, 1885 (2002).
- [79] J. Zhou, C. Q. Sun, K. Pita, Y. L. Lam, Y. Zhou, S. L. Ng, C. H. Kam, L. T. Li, and Z. L. Gui, *Appl. Phys. Lett.* **78**, 661 (2001).
- [80] V. G. Golubev, V. Y. Davydov, N. F. Kartenko, D. A. Kurdyukov, A. V. Medvedev, A. B. Pevtsov, A. V. Scherbakov, and E. B. Shadrin, *Appl. Phys. Lett.* **79**, 2127 (2001).
- [81] V. G. Golubev, D. A. Kurdyukov, A. B. Pevtsov, A. V. Sel'kin, E. B. Shadrin, A. V. Il'inskii, and R. Boeyink, *Semiconductors* **36**, 1043 (2002).
- [82] S. Kim and V. Gopalan, *Appl. Phys. Lett.* **78**, 3015 (2001).
- [83] V. Babin, P. Garstecki, and R. Hołyst, *Appl. Phys. Lett.* **82**, 1553 (2003).
- [84] K. Yoshino, Y. Kawagishi, M. Ozaki, and A. Kose, *Jpn. J. Appl. Phys* **38**, L786 (1999).
- [85] G. Subramania, R. Biswas, K. Constant, M. M. Sigalas, and K. M. Ho, *Phys. Rev. B* **63**, 235111 (2001).
- [86] N. P. Johnson, A. Z. Khokhar, M. A. McLachlan, D. W. McComb, and R. D. de la Rue, in *Photonic Crystal Materials and Nanostructures*, edited by R. M. de la Rue, P. Viktorovitch, C. M. Sotomayor-Torres, and M. Midrio (2004), vol. 5450

- of *Proc. SPIE*, p. 62.
- [87] E. J. Reed, M. Soljačić, and J. D. Joannopoulos, *Phys. Rev. Lett.* **91**, 133901 (2003).
 - [88] A. Fegotin, Y. A. Godin, and I. Vitebsky, *Phys. Rev. B* **57**, 2841 (1998).
 - [89] Y.-K. Ha, J.-E. Kim, H. Park, C.-S. Kee, and H. Lim, *Phys. Rev. B* **66**, 075109 (2002).
 - [90] P. M. Johnson, A. F. Koenderink, and W. L. Vos, *Phys. Rev. B* **66**, 081102(R) (2002).
 - [91] G. Pan, R. Kesavamoorthy, and S. A. Asher, *Phys. Rev. Lett.* **78**, 3860 (1997).
 - [92] A. V. Akimov, A. V. Virchenko, V. G. Golubev, A. A. Kaplyanskii, D. A. Kurdyukov, A. B. Pevtsov, and A. V. Shcherbakov, *Phys. Solid State* **45**, 240 (2003).
 - [93] H. Han, S. Vijayalakshmi, A. Lan, Z. Iqbal, H. Grebel, E. Lalanne, and A. M. Johnson, *Appl. Phys. Lett.* **82**, 1458 (2003).
 - [94] X. Hu, Q. Zhang, Y. Liu, B. Cheng, and D. Zhang, *Appl. Phys. Lett.* **83**, 2518 (2003).
 - [95] A. Haché and M. Bourgeois, *Appl. Phys. Lett.* **77**, 4089 (2000).
 - [96] S. W. Leonard, H. M. van Driel, J. Schilling, and R. Wehrspohn, *Phys. Rev. B* **66**, 161102(R) (2002).
 - [97] A. D. Bristow, J.-P. R. Wells, W. H. Fan, A. M. Fox, M. S. Skolnick, D. M. Whittaker, A. Tahraoui, T. F. Krauss, and J. S. Robert, *Appl. Phys. Lett.* **83**, 851 (2003).

CHAPTER 2

EXPERIMENTAL DETAILS

Abstract

We describe two pump-probe setups designed for studying the dynamical ultrafast optical properties of photonic crystals down to the femtosecond time domain.

2.1 Introduction

The measurement of the dynamical optical properties on the femtosecond time scale cannot be achieved by electronic devices but require an optical technique. The so-called pump-probe method allows us to resolve the dynamics of optical properties such as reflection, transmission, and absorption in both the visible and infrared spectral range, on the ultrafast time scale, say down to 4 fs [1]. This method uses two short optical pulses, one of which, called *pump* generally has a strong intensity and the other, called *probe*, is taken usually much weaker. The pump pulse excites the sample under study and induces changes in its optical properties. The probe pulse arrives on the excited spot with a variable delay and monitors the induced changes in the optical properties. The delay between pump and probe pulses can be adjusted by an optical delay line with high accuracy allowing for monitoring changes of the optical properties on the femtosecond timescale. The time resolution of this method is limited by the duration of the pump and probe pulses. Unfortunately, the pump-probe method yields only one measurement point per setting of the delay between pump and probe pulses. In order to be able to compose a temporal dependence of the dynamic effects, one needs to perform a set of measurements at different settings of time delay. This imposes the constraint that the optical setup must be stable during the entire measurement run. Another difficulty in pump-probe measurements can be caused by the usually very weak amplitude of the signals that may be comparable or even less than

the background noise level. In this case, one uses phase-sensitive techniques to extract the signal and average out the incoherent noise fluctuations.

The experiments described in this thesis were carried out employing two different pump-probe setups, whose principles of operation are described below. Specific details related to each individual experiment will be described in the corresponding chapters. The first setup allowed us to study the transient reflectivity at high temporal resolution (~ 30 fs) and moderate excitation power density. The second setup has much lower repetition rate and reaches much higher excitation power densities, at the expense of a lower temporal resolution (~ 170 fs).

2.2 Experimental setup with high temporal resolution

The experimental setup with the highest temporal resolution (~ 30 fs) is designed to be able to examine both stationary reflection spectra in the visible and transient changes in the reflectivity induced by ultrashort optical excitation at 800 nm in strongly scattering samples such as a photonic crystal [2, 3]. The setup has a sensitivity better than 10^{-4} and was used to demonstrate ultrafast all-optical switching in opal-Si composites (see Chapter 3).

2.2.1 Experimental setup with high repetition rate

The pump-probe setup with a high repetition rate and temporal resolution has a special design in order to suppress interference of pump and probe pulses during temporal overlap (Fig. 2.1). The beam from a 15-fs Ti-sapphire laser (FEMTO-SOURCE) with a repetition rate of 75 MHz was split in a pump and a probe by a standing wave acousto-optic modulator (AOM) operating at 35.5 MHz. The first-order diffracted beam, acting as the probe, is strongly phase-modulated relative to the zero-order (non-diffracted) beam, acting as the pump. The modulation frequency of the probe beam was chosen far beyond the photodetector bandwidth. As a result, linear interference effects during pulse overlap are reduced to values well below 10^{-4} . In addition, the pump and the probe beams were made cross-polarized that further suppresses interference. To compensate for the chirp induced by the AOM crystal, both pump and probe beams were reflected 16 times from mirrors with a negative dispersion, leading to an overall 30-fs time resolution. The collimated probe beam was passed via a computer-controlled delay line with 1- μ m precision. The pump and probe beams (4 and 2 mm diameter, respectively) were focused on the same 85- μ m spot at the sample surface at near-zero

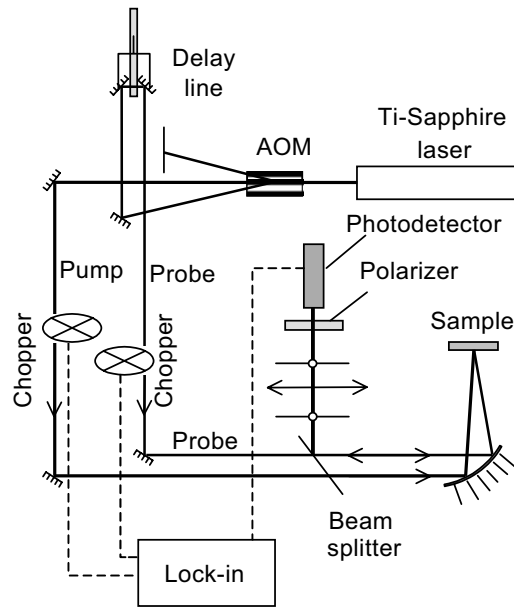


FIGURE 2.1 Pump-probe setup operated at 75-MHz repetition rate. The interference during the temporal overlap between the pump and probe pulses is suppressed by shifting the probe frequency with an AOM.

angle of normal incidence using a parabolic mirror. The energy densities of the probe and pump pulse at the surface were typically $5 \mu\text{J}/\text{cm}^2$ and $70 \mu\text{J}/\text{cm}^2$, respectively. The reflected probe light was picked up by a beam splitter, passed through the spatial filter, and focused on a photodiode. Scattered pump light was rejected by a polarizer.

This method allows us to study effects close to zero time delay. In order to increase the signal-to-noise ratio further, each beam was chopped before the sample at frequencies ν_1 and ν_2 , respectively, and the nonlinear changes in the probe intensity were extracted with an accumulation time of 1 s by a calibrated lock-in amplifier operating at the sum frequency $\nu_1 + \nu_2 \sim 1 \text{ kHz}$. At each position of the delay line, we performed 10 measurements, which were subsequently averaged. Obtained values were divided by the intensity of the reference beam split off from the probe beam prior to the sample.

2.2.2 Double modulation technique

The principle of the double modulation technique used in this thesis can be explained as follows. For small changes induced by the pump pulse, the intensity of light reflected from the sample, I_r , can be written as

$$I_r = RI_{probe} + \gamma I_{probe} I_{pump}, \quad (2.1)$$

where R is the linear reflectivity of the sample, I_{probe} and I_{pump} the intensities of the probe and the pump pulses, respectively, and γ a constant describing the nonlinear reflectivity.

Then, the relative change in the reflectivity reads

$$\frac{\Delta R}{R} = \frac{\gamma}{R} I_{pump}. \quad (2.2)$$

On the millisecond timescale both pump and probe light are modulated according to $I_{pump} = I_{pump}^A \Theta(\sin 2\pi\nu_1 t)$ and $I_{probe} = I_{probe}^A \Theta(\sin 2\pi\nu_2 t)$, respectively, where t is time, I_{pump}^A and I_{probe}^A the maximal intensity of the pump and the probe light, respectively, and Θ the Heaviside step function defined as

$$\Theta(x) = \begin{cases} 0, & x < 0 \\ 1, & x \geq 0 \end{cases}. \quad (2.3)$$

Since both pump and probe intensities are periodic in time, Eq. (2.1) can be expanded in a Fourier series

$$I_r = RI_{probe}^A \left[\frac{1}{2} + \sum_{m>0} \frac{2}{\pi N_m} \sin(\Omega_{m0} t + \Psi_{m0}) \right] + \gamma I_{probe}^A I_{pump}^A \left[\frac{1}{4} + \sum_{m>0} \sum_{l>0} \frac{2}{\pi^2 N_m N_n} \sin(\Omega_{mn} t + \Psi_{mn}) \right], \quad (2.4)$$

with

$$\begin{aligned} \Omega_{mn} &= 2\pi(\nu_2 N_m \pm \nu_1 N_l), \\ \Psi_{mn} &= \varphi_2 N_m \pm \varphi_1 N_l. \end{aligned} \quad (2.5)$$

Here, $N_m = 2m - 1$, $N_n = 2n - 1$, m and l are natural integers. Further, φ_1 and φ_2 are the phases of pump and probe modulations, respectively.

The double-modulation technique employs a lock-in amplifier as a narrow-band frequency filter. In our experimental condition, the measured signal I_r was passed via a lock-in that admits only $\nu_1 + \nu_2$, and has maximum transmission when the phase of the lock-in is adjusted according to $\varphi_1 + \varphi_2 = 0$. Now, in order to reject the frequency components of the linearly reflected probe and the scattered pump light and to admit exclusively the non-linear signal, the modulation frequencies must be chosen such that $\nu_1 l \neq \nu_2 m$ for any integers l and m . (However, this requirement is difficult to fulfil, since the phases of the modulations should be locked, $\varphi_1 + \varphi_2 = 0$. In practice, one aims at $(\nu_1/s_1)p = (\nu_2/s_2)q$, where s_1 and s_2 are the numbers of slits in each chopper, and $p \gg 1$, $q \gg 1$ are large integers. Moreover, qs_1 and ps_2 should not have a common denominator). Under these conditions, the transmitted signal is proportional to the nonlinear signal,

$$I_r(\nu_1 + \nu_2) = \frac{2}{\pi^2} \gamma I_{probe}^A I_{pump}^A. \quad (2.6)$$

This scheme virtually rejects all low-frequency noise of the laser source.

When applied in a real sample, the technique described above suffers, from a strong spurious signal related to the sample heating induced by the modulated pump intensity. Heating, namely, modifies the sample reflectivity and thus decreases the effectiveness of the lock-in scheme. We discovered, however, that the sign of the thermally induced changes depends on the locations chosen on the sample. It appeared that there exist specific areas in the sample, on which, quite fortuitously, the amplitude of the thermally induced modification is negligible. Although the nature of this phenomenon is not clear, we took advantage of it to suppress spurious effects of heating.

2.2.3 Linear reflection

Stationary reflectance spectra were measured with a halogen lamp, a spectrometer, and a charge-coupled device (CCD) from OCEAN OPTICS. The collimated 2-mm diameter beam from the lamp was sent along the same optical path as the probe laser beam (Fig. 2.2). The difference in the propagation direction of the Bragg-diffracted beam and the specular beam allowed us to separate the effects from the 3D opal structure from the ordinary surface reflection of the sample. In the first configuration the specular beam was blocked, and only the Bragg diffracted light was collected over a solid angle of $3.5 \times 10^{-2}\pi$. In the second configuration, a diaphragm of 2-mm diameter selected the specular beam and suppressed the Bragg light. Due to structural defects in the opal lattice [4–7], the Bragg light emerges as a cone extending over several degrees, depending on the point selected on the sample surface.

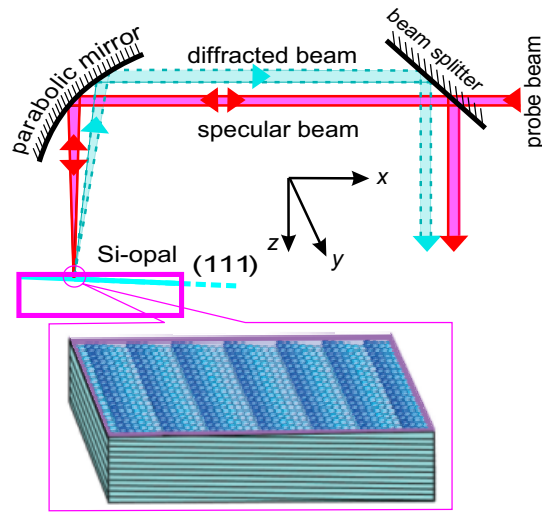


FIGURE 2.2 Diagram illustrating the beam paths of the incident probe-, the specular-, and the Bragg diffracted beam. Inset schematically shows the faceted sample surface.

2.3 Experimental setup with low repetition rate

The 1-kHz pump-probe experimental setup is shown in Fig. 2.3. Ultrafast excitation of the photonic crystal was induced by an intense optical 120-fs pump pulse from an amplified femtosecond Ti-sapphire laser operating at 1 kHz and 800 nm (Spectra Physics, HURRICANE) [8–10]. The pump pulse was focused onto a $400\text{-}\mu\text{m}$ spot at the sample surface with a surface energy density in the range of $0.5\text{--}10\text{ mJ/cm}^2$ per pulse. The pump power density was controlled by the aperture of a diaphragm placed in the pump beam. The time-resolved reflection spectrum was monitored by a weak, ultrafast, white light continuum probe pulse generated in a thin sapphire plate by part of the same Ti-sapphire laser pulse train used in the pump. In order to reject the residual 800-nm pump light, the white light was passed via an optical band-pass filter. The probe pulse propagating close to the $[1\ 1\ 1]$ direction of the photonic crystal was focused onto a $25\text{-}\mu\text{m}$ spot at the sample surface within the area illuminated by the pump. The Bragg-reflected probe light was picked up by a lens, passed via a spatial filter, and focused onto the entrance of an optical fiber. The fiber transferred the Bragg-reflected light to a spectrometer (Action Research, SPECTRAPRO 300i) with a spectral resolution of 1 nm and equipped with a cooled CCD (Roper Scientific, model CCD-1340-EB/1) read out by a computer. An optical delay line controls the time delay between pump

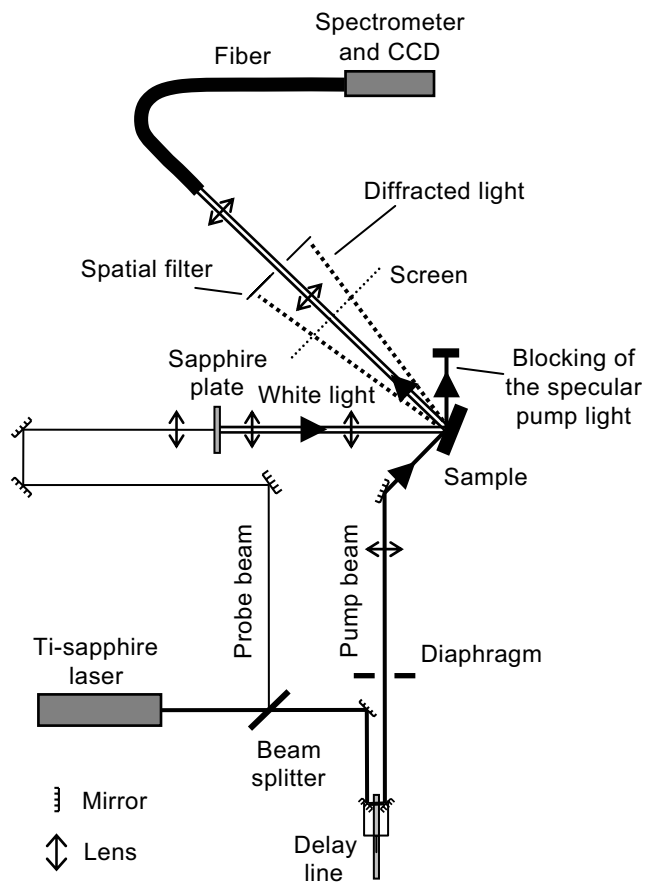


FIGURE 2.3 Pump-probe setup operated at 1-kHz repetition rate.

and probe pulses with 10- μm precision. Correction for the chirp of the probe light is possible relying on time-resolved transmission spectra taken in an amorphous silicon film at otherwise the same experimental conditions. Since the response of the silicon film is virtually instantaneous [11], we readily obtained the spectral dependence of the chirp and corrected the spectral-temporal dependencies of the Bragg-reflectivity. After correction, our temporal resolution was only limited by the pump-probe temporal overlap ($\tau_p \approx 170$ fs). In order to increase the signal-to-noise ratio, all spectra have been averaged over a spectral width of 15 nm. The stationary reflection spectra were obtained in the same experimental configuration but in absence of the pump pulse.

The pump-probe experiment with low repetition rate (1 kHz) allows us to apply higher power densities of the pump excitation without destroying the sample.

References

- [1] I. Walmsley, L. Waxer, and C. Dorrer, *Rev. Sci. Instrum.* **72**, 1 (2001).
- [2] D. A. Mazurenko, R. Kerst, J. I. Dijkhuis, A. V. Akimov, V. G. Golubev, D. A. Kurdyukov, A. B. Pevtsov, and A. V. Sel'kin, *Phys. Rev. Lett.* **91**, 213903 (2003).
- [3] D. A. Mazurenko, A. V. Akimov, A. B. Pevtsov, D. A. Kurdyukov, V. G. Golubev, and J. I. Dijkhuis, *Physica E* **17**, 410 (2003).
- [4] V. N. Astratov, A. M. Adawi, S. Fricker, M. S. Skolnick, D. M. Whittaker, and P. N. Pusey, *Phys. Rev. B* **66**, 165215 (2002).
- [5] Y. A. Vlasov, V. N. Astratov, A. V. Baryshev, A. A. Kaplyanskii, and O. Z. Karimov, *Phys. Rev. E* **61**, 5784 (2000).
- [6] J. F. G. López and W. L. Vos, *Phys. Rev. E* **66**, 036616 (2002).
- [7] J. Huang et al., *Phys. Rev. Lett.* **86**, 4815 (2001).
- [8] D. A. Mazurenko, A. V. Akimov, A. B. Pevtsov, D. A. Kurdyukov, V. G. Golubev, and J. I. Dijkhuis, *J. Lumin.* **108**, 163 (2004).
- [9] D. A. Mazurenko, A. V. Akimov, V. G. Golubev, D. A. Kurdyukov, A. B. Pevtsov, R. Kerst, and J. I. Dijkhuis, in *Photonic Crystal Materials and Nanostructures*, edited by R. M. de la Rue, P. Viktorovitch, C. M. Sotomayor-Torres, and M. Midrio (2004), vol. 5450 of *Proc. SPIE*, p. 250.
- [10] D. A. Mazurenko, A. Moroz, C. M. Graf, A. van Blaaderen, and J. I. Dijkhuis, in *Photonic Crystal Materials and Nanostructures*, edited by R. M. de la Rue, P. Viktorovitch, C. M. Sotomayor-Torres, and M. Midrio (2004), vol. 5450 of *Proc. SPIE*, p. 569.
- [11] K. E. Myers, Q. Wang, and S. L. Dexheimer, *Phys. Rev. B* **64**, 161309(R) (2001).

CHAPTER 3

OPTICAL SWITCHING IN OPAL-SI

Abstract

We present the first experimental investigation of ultrafast optical switching in a three-dimensional photonic crystal made of a Si-opal composite. Photoinduced changes turn out to be enhanced around the photonic stop bands and reach 46% at high excitation power (5 mJ/cm^2). Short-lived photoexcited carriers in silicon induce changes in the dielectric constant of Si and diminish the constructive interference inside the photonic crystal. We show that the switching-on time is faster than 30 fs and determined by the pump pulse duration. The switching-off time is in the order of several picoseconds. Obtained results for moderate pump powers ($70 \mu\text{J/cm}^2$) are analyzed within a model based on a two-band mixing formalism.

3.1 Introduction

The rapidly expanding research in photonics is driven by various opportunities to create novel devices, such as all-optical switches and optical computers [1]. The performance of such devices might surpass the speed of traditional electronics by several orders of magnitude and result in a true revolution in nanotechnology. These devices will likely be based on photonic crystals where multiple Bragg diffraction is capable to inhibit or promote propagation of light at specific frequencies. One of the most spectacular phenomena of a photonic crystal is the existence of a photonic stop band (PSB) - a range of wavelengths on which light cannot propagate in certain directions [2]. Spontaneous emission of an excited atom with a transition frequency in the PSB is suppressed. In case of a three-dimensional (3D) photonic crystal, a PSB may extend even over the full space angle, form a true bandgap for photons, and may completely quench spontaneous emission [3]. For applications based on the all-optical switching principle (e.g. all-optical processors, pulsed lasers, and optical memories), it is important to

realize dynamic control over the optical properties of a photonic crystal on the shortest timescale possible. In order to achieve this goal, precise knowledge of the ultrafast non-linear properties of photonic crystals is a prerequisite.

Switching of a photonic crystal can be realized by rapidly changing its refractive index by some external impact. As has been predicted recently [4, 5], 3D photonic crystals should be switchable on the femtosecond time scale by hot carriers generated in a semiconductor by absorption of a short optical pulse. Recently, ultrafast switching has been realized in 1D [6] and 2D [7] silicon-based photonic crystals. Switching in 3D photonic crystals was studied only down to the nanosecond time scale [8, 9].

Here, we present the first experimental results of femtosecond pump-probe experiments in a 3D photonic crystal in the region of the PSB [10]. To demonstrate ultrafast optical switching, we chose Si-embedded opals. Opals are known to be model objects for studying PSB effects [1, 11]; silicon is very suitable for a dynamic experiment, because of its weak, but noticeable absorption in the near-infrared region, its high index of refraction, and its short carrier lifetime. Quite importantly, Si-opal structures can be integrated in optical circuits [12]. Since silicon is the material in the opal-Si composite, which absorbs the visible light, its optical properties largely determine the optical switching of opal-Si by external light. Therefore, we will first describe the dynamical properties of bulk amorphous silicon.

3.2 Ultrafast dynamics in bulk silicon

Nowadays silicon is the most popular material for semiconductor devices. This is, perhaps, the main reason to explain the general interest in its ultrafast optical properties. Dynamic optical response in thin silicon films on a short timescale has been intensively studied during the last decades. However, the evolution of the dielectric constant of silicon after an optical excitation is rather complicated and presents many opportunities for novel experiments [13].

It is important to distinguish two types of optical non-linearity. The first one, usually referred to the Kerr non-linearity, is instantaneous and occurs when pump and probe pulses are temporally overlapped. In this case, a change in the complex dielectric constant of silicon $\epsilon_{Si} = \epsilon'_{Si} + i\epsilon''_{Si}$ is induced by the strong electric field of the pump pulse. The effect is governed by two-photon absorption and Stark shift of the band-edge absorption [14]. It was established that for all semiconductors the Kerr nonlinearity $\Delta\epsilon'_{Si}$ has a maximum when excited at approximately $0.6E_g$ and changes its sign at $0.8E_g$. Here, E_g is the electron bandgap energy. The

change in $\Delta\epsilon''_{Si}$ increases for the light frequency ranging from $E_g/2$ to E_g . We note, that the amplitude of the Kerr effect is directly proportional to the *intensity* of the pump pulse.

The second type of nonlinearity is related to residual changes that remain or even develop in the material *after* excitation. In silicon such changes are induced by photoexcited electrons and holes that are formed during excitation. At low and moderate pump power densities, when two-photon absorption is negligible compared to linear absorption, this nonlinearity is directly proportional to the integrated *power* of the pump pulse. The excited carriers act as an electron-hole plasma and according to Drude theory modify the complex dielectric constant of silicon [15]. The amplitude of these changes scales linearly with the plasma density up to the melting threshold [16, 17]. We note, that $\Delta\epsilon'_{Si} < 0$ and $\Delta\epsilon''_{Si} > 0$. The subsequent dynamics of the dielectric constant in the infrared spectral region has a multi-exponential shape and the following stages can be distinguished (see Fig. 3.1):

(I) Decoherence. Initially, the excited electron-hole pairs lose their coherence due to momentum scattering that occurs on typical timescales well below 100 fs [18] and can be hardly resolved in experiments [19].

(II) Electron energy relaxation. On a timescale of the order of a few hundred femtoseconds, electron-phonon relaxation takes place, and electrons lose their kinetic energy via phonon emission [20, 21]. It turns out that the electron-phonon relaxation rate slightly depends on the energy [19] and the power density of a pump excitation [22]. In addition, the electron-electron relaxation occurs on the same or even faster timescale [23]. Both processes result in a relaxation of the electrons towards the bottom of the conduction band thereby changing the electron effective masses. Consequently, the plasma frequency also changes, and as a result, the dielectric constant.

(III) Carrier trapping. On the picosecond timescale, electrons and holes are recombining and descending on the band-tail traps. The dynamics is different for amorphous and nanocrystalline silicon and further depends on the pump power density signifying a bi-molecular type of recombination processes [16]. However, the precise microscopic mechanism of recombination is not fully understood [24]. Next to bimolecular recombination, thermal effects can play a role: both nonradiative recombination and the trapping processes create acoustic phonons that also affect the dielectric constant [25]. The thermally-induced $\Delta\epsilon_{Si}'$ has an opposite sign (positive) with respect to the electron-induced one. At some specific time, $\Delta\epsilon_{Si}'$ may even change its sign from negative to positive [26], thus effectively accelerating the recovery dynamics.

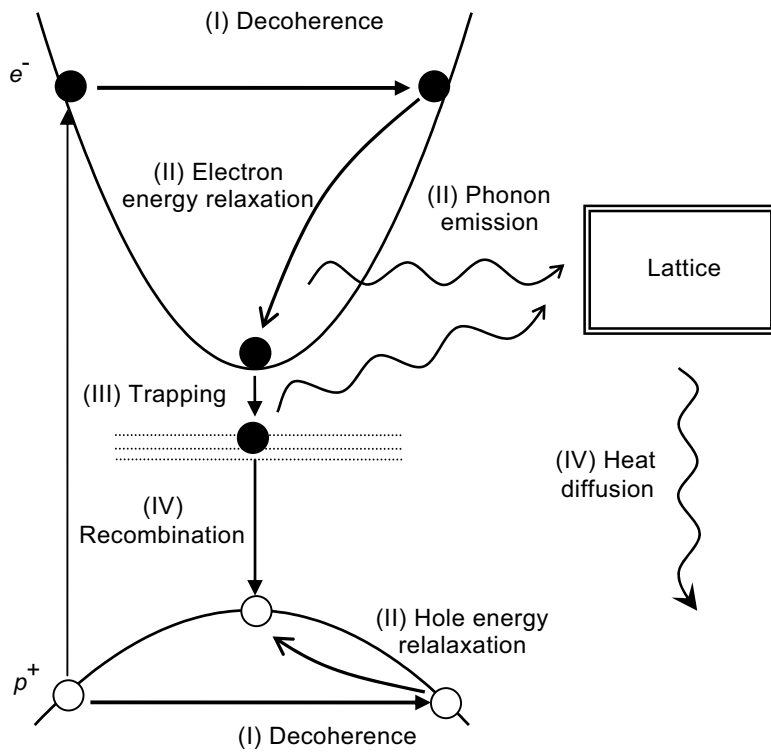


FIGURE 3.1 Schematics of ultrafast dynamics in silicon, (I) optical excitation of electron-hole pairs and decoherence, (II) energy relaxation of hot carriers and phonon emission, (III) trapping of carriers, and (IV) heat diffusion.

(IV) Recombination of trapped carriers and heat diffusion. Recombination of trapped carriers govern the dynamics of the dielectric constant of silicon on the sub-nanosecond and nanosecond timescales [27]. Obviously, nonradiative recombination of the trapped carriers supply additional heating to the silicon lattice thus further increasing the real part of the dielectric constant. The long-term kinetics is, finally, determined by thermal diffusion. Characteristic times of the thermal diffusion may vary from 100 ps, e.g. in case of excitation on silicon-sapphire interface, to micro- and even millisecond time scales, e.g. when silicon is surrounded by material with a low heat conductivity, as the case in point where silicon is grown in the voids of opal.

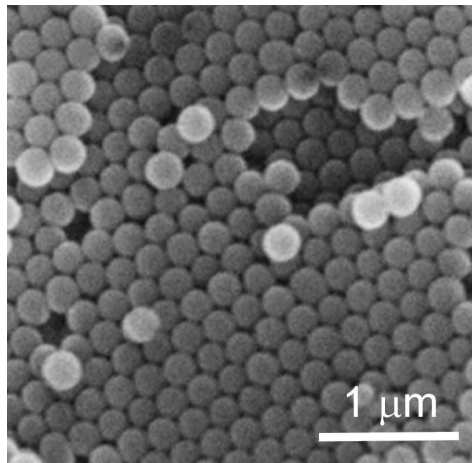


FIGURE 3.2 SEM image of the (111) plane of a bare opal used as a template for fabricating opal-Si photonic crystal. This picture is taken from the Ref. [28].

3.3 Sample and experimental details

The sample used for the demonstration of all-optical switching was fabricated in the Ioffe Physico-Technical Institute in St. Petersburg, Russia. The sample is composed of close-packed SiO_2 spheres, 230 nm in diameter, forming an ordered face-centered cubic (fcc) polydomain opalescent matrix. A scanning electron microscope (SEM) image of this matrix is shown in Fig. 3.2. The voids of this opal have been filled by silicon using thermal decomposition of 5% SiH_4 -Ar gas mixture. The filling factor was chosen close to 100% in order to arrive at a PSB located around the wavelength of the Ti-sapphire laser (800 nm). After the growth of the silicon in the voids, the sample was annealed in air at 800°C. Finally, we obtained an opal with amorphous-nanocrystalline silicon (a-nc-Si) in the voids. The SEM [28, 29] studies showed that the size of a single domain ranges from 30 μm to 100 μm . The sample was cut out to a 0.5-mm thick plate, with the surface (area of 10 mm^2) almost parallel to the (1 1 1) surface. Further details of growth and optical properties of the sample can be found in Ref. [28, 29].

Transient changes in the reflectivity and stationary reflectance spectra of both the Bragg diffracted and specular beam were measured using the high-repetition-rate (75 MHz) pump-probe setup described in Sec. 2.2. The Bragg diffracted light and the specular beam were separated and measured independently. It is worth noting that the average reflectivity of the opal-Si was gradually drifting away dur-

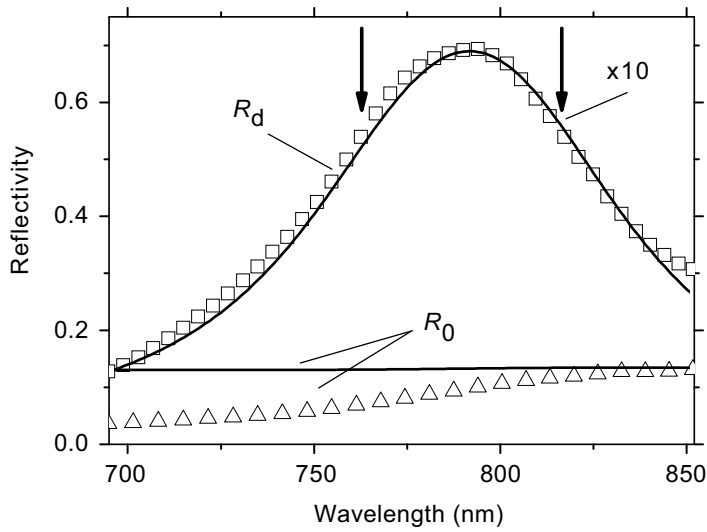


FIGURE 3.3 Measured (symbols) and calculated (solid lines) linear spectra of the specular reflection (R_0) and Bragg diffraction efficiency (R_d). Experimental data are normalized to the maximum of the R_d theoretical curve. Vertical arrows point at the calculated positions of the photonic band edges when the imaginary part of the dielectric constant is neglected.

ing the course of the pump-probe experiments due to the Staebler-Wronski effect [30] that appeared to increase the background noise level but did not affect neither the amplitude nor shape of the *differential* reflectivity.

3.4 Experimental results

3.4.1 Linear reflectance

In Fig. 3.3 the symbols show the measured linear stationary reflection spectra for the two configurations, the specular and the Bragg-diffracted one. The Bragg diffracted spectrum R_d peaks around $\lambda = 790$ nm and has a width of 66 nm, in agreement with earlier studies of similar samples. The origin of the peak is attributed to the PSB [29]. The specularly reflected light R_0 has a higher intensity, but does not exhibit the PSB structure.

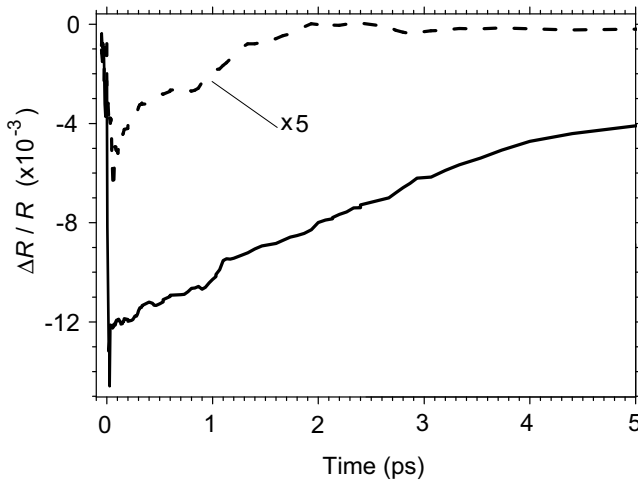


FIGURE 3.4 Temporal evolutions of transient changes in the specular reflection (dashed line) and Bragg diffraction efficiency (solid line).

3.4.2 Transient changes in reflectance

Typical pump-probe signals are presented in Fig. 3.4 for the specular ($\Delta R_0(t)/R_0$, dashed line) and Bragg-diffracted case ($\Delta R_d(t)/R_d$, solid line). In Fig. 3.5 we display an expanded time trace of $\Delta R_0(t)/R_0$. Both signals exhibit switching in less than 30 fs, limited by the time resolution of our experimental setup. The subsequent decay is multi-exponential with time constants $\tau_1 = 0.5 \pm 0.2$ ps and $\tau_2 = 5 \pm 2$ ps. We note that the measured values for the time constants vary over the sample surface, but not more than by 50%.

The most important experimental result is the large difference between the relative amplitudes of the transient signals, $\Delta R_d(t)/R_d = -(1.2 \pm 0.2) \times 10^{-2}$ and $\Delta R_0(t)/R_0 = -(9 \pm 2) \times 10^{-4}$. This effect, observed for all points studied at the sample surface, leads us to the conclusion that the pump light induces substantial ultrafast changes in the PSB properties of our 3D Si-opal photonic crystal. Quite naturally, these pump-induced changes in the optical properties of the photonic crystal should depend on the pump-probe wavelength. To check this, we carried out experiments in the PSB spectral range with a tunable 170-fs Ti-sapphire laser (MIRA), further using the same setup but without a spatial filter. The dependence of the amplitude of the obtained transient signal $\Delta(R_0 + R_d)/(R_0 + R_d)$ on the pump-probe wavelength is shown in Fig. 3.6 as symbols. Unfortunately, the high noise level of the intensity of the MIRA introduces quite sizable errors. However, in the

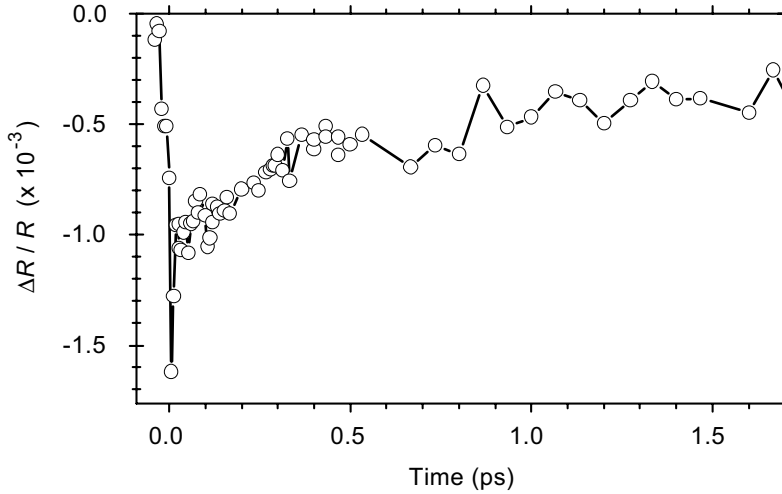


FIGURE 3.5 Transient changes in the specular reflection measured with 30 fs time resolution.

spectral region which was available in the laser tuning range, we observed that the photo-induced signal is not constant but clearly rises upon entering the PSB wavelength region.

The measured temporal evolution of $\Delta R(t)$ (Fig. 3.4) has a complicated shape. The pronounced peak around zero time delay is the instantaneous contribution from the Kerr effect [14]. The subsequent evolution of $\Delta R(t)$ is controlled by photoexcited electrons and holes in silicon. The presence of free carriers modifies the complex dielectric constant of Si, $\varepsilon_{Si} = \varepsilon'_{Si} + i\varepsilon''_{Si}$, that, in turn, changes the mean dielectric constant $\bar{\varepsilon}$, and correspondingly, modifies the photonic density of states of the photonic crystal. The temporal shape of $\Delta R(t)$ (Fig. 3.4) is similar to the signals obtained in nanocrystalline Si films [21] and amorphous Si films [16, 31] and was attributed to the energy relaxation of free carriers.

3.5 Theory

In order to explain the observed reflection and diffraction phenomena, we use a quantitative model developed by A. V. Sel'kin. This model is based on the two-band mixing formalism [32] that analyzes the relevant surface reflection effects in photonic crystal and yields theoretical estimates for both the specular and the Bragg reflectivity near the first-order PSB. We assume that the incoming probe

light propagates close to the [111] direction of the fcc photonic crystal near the L -point of the first Brillouin zone. Propagation of electromagnetic waves with a frequency ω through an uncharged dielectric medium is described by Maxwell's equations

$$\nabla \times \mathbf{E} = -i\omega\mathbf{B}, \quad (3.1)$$

$$\nabla \times \mathbf{H} = -i\omega\mathbf{D}, \quad (3.2)$$

$$\nabla \cdot (\mathbf{B}) = 0, \quad (3.3)$$

$$\nabla \cdot (\mathbf{D}) = 0, \quad (3.4)$$

together with the relation for a non-magnetic media

$$\begin{aligned} \mathbf{D}(\mathbf{r}) &= \varepsilon_0 \varepsilon(\mathbf{r}) \mathbf{E}(\mathbf{r}), \\ \mathbf{B} &= \mu_0 \mathbf{H}, \end{aligned} \quad (3.5)$$

where \mathbf{E} and \mathbf{H} are the electric and magnetic fields, respectively, ε_0 and μ_0 the permittivity and the permeability of vacuum, respectively, and \mathbf{r} the radius-vector. Further, the dielectric constant, $\varepsilon(\mathbf{r})$, is taken static and dispersionless in the frequency range under consideration, but possesses a spatial periodicity according to

$$\varepsilon(\mathbf{r}) = \varepsilon(\mathbf{r} + \mathbf{p}_{111}). \quad (3.6)$$

Here, \mathbf{p}_{111} is the lattice vector in the [1 1 1] direction with $|\mathbf{p}_{111}| = \sqrt{2/3}d$. Within the framework of this model, the modulation of $\varepsilon(\mathbf{r})$ in the (1 1 1) plane is not taken into account.

Equation (3.3) combined with Eq. (3.5) can be expressed as

$$\varepsilon(\mathbf{r}) \nabla \cdot \mathbf{E}(\mathbf{r}) = -\mathbf{E}(\mathbf{r}) \cdot \nabla \varepsilon(\mathbf{r}). \quad (3.7)$$

We note, that \mathbf{E} and $\nabla \varepsilon$ are orthogonal which reduces Eq. (3.7) to

$$\nabla \cdot \mathbf{E}(\mathbf{r}) = 0. \quad (3.8)$$

It is well known, that Eq. (3.8) combined with the Maxwell equations leads to the wave equation

$$-\nabla^2 \mathbf{E}(\mathbf{r}) - \frac{\omega^2}{c^2} \varepsilon_r(\mathbf{r}) \mathbf{E}(\mathbf{r}) = \frac{\omega^2}{c^2} \bar{\varepsilon} \mathbf{E}(\mathbf{r}). \quad (3.9)$$

Here, we have chosen to separate the dielectric constant into two parts: $\varepsilon(\mathbf{r}) = \bar{\varepsilon} + \varepsilon_r(\mathbf{r})$, where $\varepsilon_r(\mathbf{r})$ is the spatially varying part and $\bar{\varepsilon} = \varepsilon_{Si}(1-f) + \varepsilon_s f + i\bar{\varepsilon}''$ the volume averaged dielectric constant, with ε_s the dielectric constant of SiO₂ spheres occupying a relative volume $f = \sqrt{2}/6\pi \approx 0.74$ and $\bar{\varepsilon}''$ the imaginary part of $\bar{\varepsilon}$ governed by elastic light scattering at imperfections of the opal.

Equation (3.9) is a vector equation but reminiscent of the scalar time-independent Schrödinger equation for electrons in a crystal lattice. Similar to the standard theory of electrons near a bandgap, $\mathbf{E}(\mathbf{r})$ can be considered as a superposition of Bloch modes. Close to the L -point only two vectors, \mathbf{K} and $\mathbf{K}-\mathbf{G}$, are relevant,

$$\mathbf{E}(\mathbf{r}) \approx \sum_{\mathbf{K}} (\mathbf{A}_{\mathbf{K}} e^{i\mathbf{K}\mathbf{r}} + \mathbf{A}_{\mathbf{K}-\mathbf{G}} e^{i(\mathbf{K}-\mathbf{G})\mathbf{r}}). \quad (3.10)$$

Here, \mathbf{G} is the reciprocal-lattice vector for the [1 1 1] direction, with $|\mathbf{G}| = 2\pi/|p_{111}|$ and \mathbf{K} is the Bloch vector satisfying the condition $(\mathbf{K} \cdot \mathbf{G}) \approx |\mathbf{G}|^2/2$ near the L point of the first Brillouin zone. Further, $\mathbf{A}_{\mathbf{K}}$ is the coordinate-independent Bloch amplitude of the electric field. In the same fashion, the periodic part of the dielectric constant can be expanded as

$$\varepsilon_r(\mathbf{r}) \approx \varepsilon_{\mathbf{G}} e^{i\mathbf{G}\mathbf{r}} + \varepsilon_{-\mathbf{G}} e^{-i\mathbf{G}\mathbf{r}}, \quad (3.11)$$

where $\varepsilon_{\mathbf{G}}$ and $\varepsilon_{-\mathbf{G}}$ are the appropriate Fourier coefficients, which characterize the spatial modulation of $\varepsilon(\mathbf{r})$ along the [1 1 1] direction. It is clear, that the absolute dielectric constant contrast of the photonic crystal $|\varepsilon_{\mathbf{G}}| \propto |\text{Re}(\varepsilon_{Si} - \varepsilon_s)|$.

Near the L -point, Bloch states with $\mathbf{K} = \pm\mathbf{G}/2$ are degenerate and Eq. (3.9) can be solved in the framework of perturbation theory:

$$\begin{aligned} (\mathbf{n}^2 - \bar{\varepsilon}) \mathbf{A}_{\mathbf{K}} &= \varepsilon_{-\mathbf{G}} \mathbf{A}_{\mathbf{K}-\mathbf{G}}, \\ [(\mathbf{n} - \mathbf{g})^2 - \bar{\varepsilon}] \mathbf{A}_{\mathbf{K}-\mathbf{G}} &= \varepsilon_{\mathbf{G}} \mathbf{A}_{\mathbf{K}} \end{aligned} \quad (3.12)$$

where $\mathbf{n} \equiv \mathbf{K}\lambda/2\pi$ and $\mathbf{g} \equiv \mathbf{G}\lambda/2\pi$ with λ being the wavelength of light in vacuum.

Equations (3.12) co-exist when the wavevector satisfies the dispersion equation

$$\mathbf{n}^2 - \bar{\varepsilon} = \frac{|\varepsilon_{\mathbf{G}}|^2}{(\mathbf{n} - \mathbf{g})^2 - \bar{\varepsilon}}. \quad (3.13)$$

We chose the z -axis coincident with the normal to the surface of the photonic crystal (Fig. 2.2), which slightly deviates from the (1 1 1) plane of the photonic

crystal. Further, x and z define the plane of incidence and $G_y = 0$. Naturally, the tangential component of the incident wave vector is equal to that of the transmitted Bloch wave vector K_x , i.e. $n_x = \sin \theta$, where θ is the angle of incidence.

Equation (3.13) has four roots n_{jz} ($j = 1 \dots 4$) for the z -component of the \mathbf{n} -vector. Since only roots with positive imaginary parts are physical

$$n_{-,+} = \frac{1}{2} |\mathbf{g}| + \frac{1}{2} \sqrt{F_{-,+}}, \quad (3.14)$$

where

$$F_{-,+} = |\mathbf{g}|^2 + 4\bar{\varepsilon} \pm 4 \sqrt{|\mathbf{g}|^2 \bar{\varepsilon} + |\varepsilon_{\mathbf{G}}|^2}.$$

Each \mathbf{n} -vector corresponds to a Bloch-mode electric field

$$\mathbf{E}_{\mathbf{K}}(\mathbf{r}) = \mathbf{A}_{\mathbf{K}} e^{i\mathbf{K}\mathbf{r}} \left[1 + \frac{\varepsilon - \mathbf{G}}{(\mathbf{n} - \mathbf{g})^2 - \bar{\varepsilon}} e^{-i\mathbf{G}\mathbf{r}} \right]. \quad (3.15)$$

We are left with two y -polarized Bloch modes, with K_{1z} and K_{2z} at a given θ . Propagating band modes with real \mathbf{K} corresponds to $F > 0$. In the opposite case, i.e. for gap modes, $F < 0$, the wave has a complex \mathbf{K} and decays in the photonic crystal.

Allowing for a small but non-zero incident tangential wavevector component on the surface, and using the correct boundary conditions at the surface, we have obtained a propagating (or decaying in the PSB) wave in the photonic crystal and two outgoing waves propagating in slightly different directions corresponding to the specular reflections on the surface and Bragg diffraction at the (1 1 1) planes of the photonic crystal, respectively. We note, that the boundary conditions also yield surface modes decaying both in vacuum and in photonic crystal [33], which are the optical analogue of the electronic Tamm modes. In our photonic crystal, however, these modes do not couple with outgoing waves propagating in vacuum [34] and, therefore, are not contributing to the reflection signal. However, in some other type of photonic crystal these modes can play an important role (see Chapter 5). Assuming $\theta \rightarrow 0$ after some algebraic manipulations, we finally arrive at a specular reflection coefficient R_0 and nonspecular, diffracted reflection coefficient R_d ,

$$R_0 = \left| \frac{a-b}{a+b} \right|^2 \quad \text{and} \quad R_d = \left| \frac{h}{a+b} \right|^2, \quad (3.16)$$

with

$$a = (n_- + n_+)(n_- + n_+ + 1 - |\mathbf{g}|) - n_- n_+ - \bar{\varepsilon} ,$$

$$b = (n_- n_+ + \bar{\varepsilon})(1 - |\mathbf{g}|) + n_- n_+(n_- + n_+) ,$$

$$h = 2(n_-^2 - \bar{\varepsilon})(n_+^2 - \bar{\varepsilon})/\varepsilon_G .$$

3.6 Discussion

The calculated spectra of R_d and R_0 are indicated as solid lines in Fig. 3.3 for 227-nm-diameter SiO_2 spheres and $\varepsilon_s = 1.98$. In the calculations, $|\varepsilon_G| = 0.308$, $\varepsilon'_{Si} = 12.25$, and $\bar{\varepsilon}'' = 0.34$. Further, the value for $\varepsilon''_{Si} = 0.49$ was taken from the absorption coefficient at 800 nm, $\alpha = 10^4 \text{ cm}^{-1}$, for amorphous silicon grown at low annealing temperatures [35, 36]. Both the central position and the width of R_d (Fig. 3.3) are satisfactorily reproduced. Only the calculated specular reflection spectrum R_0 deviates from the measured one and R_d does not show the experimentally observed background. The very general reason for this background, which turns out to vary over the sample surface, is the spectral dependence of the extinction due to various imperfections, grain boundaries between crystal domains, and transition layers that may exist at the surface, and causes light to be diffracted non-specularly.

Transient changes ΔR_d and ΔR_0 may also be calculated from Eq. (3.16), given the photoinduced changes $\Delta\varepsilon_{Si} = \Delta\varepsilon'_{Si} + i\Delta\varepsilon''_{Si}$ in the dielectric constant of Si known from the Drude model [15, 16]:

$$\Delta\varepsilon'_{Si} = \frac{-Ne^2}{m^*\varepsilon_0(\omega^2 + \tau_d^{-2})} \quad \text{and} \quad \Delta\varepsilon''_{Si} = \frac{-\Delta\varepsilon'_{Si}}{\omega\tau_d} . \quad (3.17)$$

Here, $m^* = 0.15m_0$ (see Ref. [17] and Ref. [48] therein) the electronic reduced mass, $\tau_d = 0.5 \text{ fs}$ [26] the Drude damping time, $\omega = 2.4 \times 10^{15} \text{ rad/s}$ the center frequency of the laser, and $N = \alpha P_{pump}/\hbar\omega$ the density of photoinduced carriers. We obtain $\Delta\varepsilon_{Si} = (-6.2 + i5.3) \times 10^{-3}$ for our experimental conditions ($P_{pump} = 70 \mu\text{J}/\text{cm}^2$). Inserting this value in Eq. (3.16) yields $\Delta R_d/R_d = -5 \times 10^{-3}$ and $\Delta R_0/R_0 = -3 \times 10^{-4}$ at 800 nm. Our calculation reproduces the more-than-one-order-of-magnitude higher photoinduced changes in the Bragg reflection spectra compared to the specular ones.

The main reason for the strong transient Bragg signal is the high sensitivity

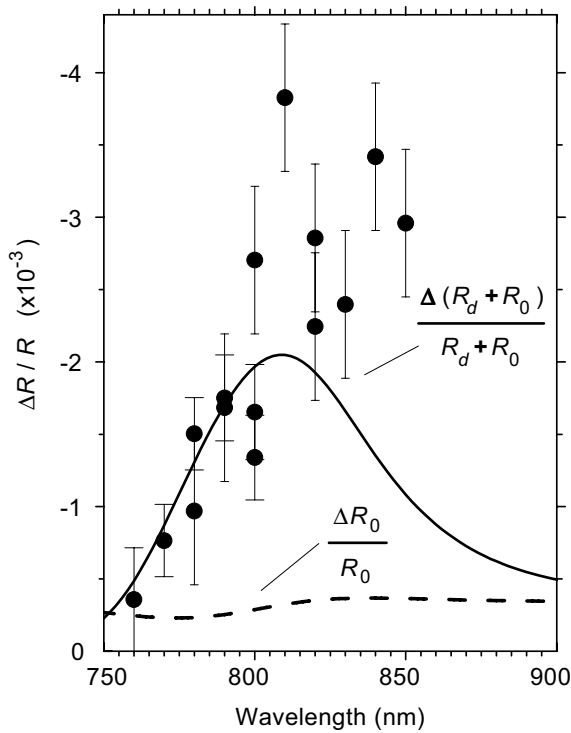


FIGURE 3.6 Calculated (solid line) and measured (symbols) spectra of the photo-induced relative changes in the total reflection. Dashed line shows the calculated relative changes in the specular reflection.

of the photonic band structure in the opal-Si to photoinduced changes in the dielectric constant of Si. The absolute calculated values for $\Delta R_d/R_d$ and $\Delta R_0/R_0$ at 800 nm deviate from the experimental values only by a factor of two and a factor of three, respectively. We attribute this to a higher optical density of pump light in Si than assumed in the model, due to local field localization effect [37]. In Fig. 3.6 we show calculated (solid line) and measured (symbols) spectra of the relative changes in the total reflection $\Delta R/R = \Delta(R_d + R_0)/(R_d + R_0)$. Dashed line shows the calculated $\Delta R_0/R_0$. As mentioned above, the experimental values of the differential reflection are somewhat higher than the calculated ones in the region of PSB. Nevertheless, the calculated and measured values for various wavelengths of the photoinduced effects (Fig. 3.6) are in reasonable agreement. We note that the amplitude of the photoinduced changes of the Bragg diffrac-

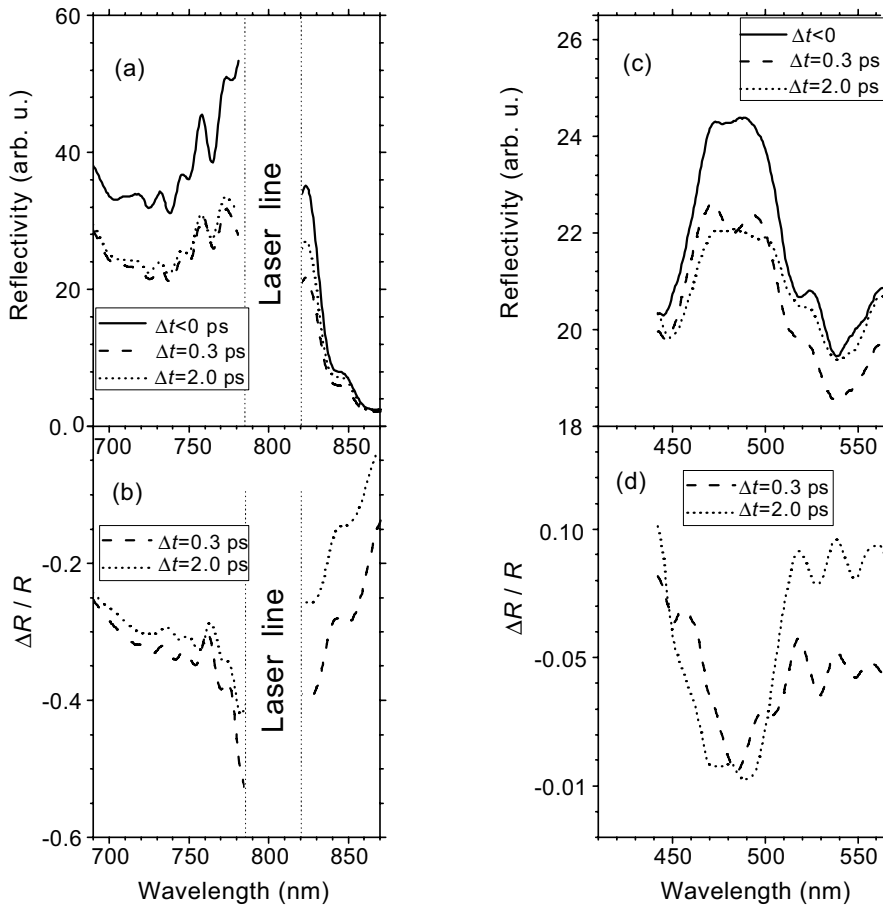


FIGURE 3.7 Chirp-corrected spectra of the Bragg reflection for negative time delay (solid line), positive delays 0.3 ps (dashed line), and 2 ps (dotted line), in case of strong 5 mJ/cm^2 optical excitation (a) and (c) in the near-infrared and in the visible range, respectively, and corresponding transient differential reflection $\Delta R_d/R_d$ (b) and (d).

tion intensity depends on the pump power density [26]. Although the amplitude of observed changes was low ($\sim 1\%$), a higher power of the optical excitation (which is not possible in a high-repetition-rate experiment due to heating) should increase $\Delta R_d/R_d$. In order to check this we performed pump-probe experiments with higher optical excitation, but lower repetition rate [38, 39].

3.7 Experiments with high excitation power density

The pump-probe setup operating at low repetition rate and described in Section 2.2 allows us to monitor photoinduced changes in the Bragg reflectivity at higher power of optical excitation and over the full visible spectral range. In this case the sample has been excited by 0.12-ps pump pulses from an 800-nm Ti-sapphire laser with a pulse repetition rate of 500 Hz. The power density of the optical excitation at the sample was 5 mJ/cm^2 per pump pulse which is close to, but below the melting threshold [17]. The reflectance spectrum was probed by a weak pulse of white-light continuum focused to a diameter of less than $30 \mu\text{m}$ in the central spot of the pump beam at the sample surface. To gain in signal-to-noise ratio, the spectral intensity has been averaged over 10-nm. In order to suppress the strong contribution of 800 nm pump light of the white light probe beam, we inserted two filters that cut light above 700 nm and below 850 nm and admit light in the spectral bandwidths of 400 – 780 nm and 820 – 1100 nm, respectively. As a consequence, the intensity of the white light was significantly suppressed in the spectral range of 700 – 850 nm, except for the region 780 – 820 nm, that is sufficient for our measurements thanks to the high dynamic range of the CCD.

3.7.1 Linear optical properties of the second-order photonic stop band

In Figs. 3.7(a) and (c), the solid line displays the measured Bragg reflectivity spectra for 690 – 870 nm and 450 – 565 nm, respectively. As noted above, the spectral region from 790 nm to 810 nm was not accessible for measurement due to the strong scattering of 800-nm pump light. At negative delay, when the probe pulse arrives before the pump pulse, the sample is not excited and the reflectivity spectrum corresponds to the linear spectrum of the photonic crystal. As was already mentioned in Sec. 3.4.1, the first and largest maximum of the reflectivity corresponds to the first order PSB that is centered at $\lambda_1 = 790 \text{ nm}$ [Fig. 3.7(a), solid line] in our photonic crystal.

A second maximum is located at $\lambda_2 = 480 \text{ nm}$ and can be attributed to the second order PSB. Here, the Bragg diffraction is significantly suppressed due to the higher absorption of silicon in that spectral range [40]. Nevertheless, the corresponding peak is clearly observed in the reflectivity spectrum [Fig. 3.7(c), solid line]. Although, one would expect to observe the second order PSB at the double frequency with respect to the first order PSB [41], $\lambda_1 = 2\lambda_2$, in our case the dispersion of the refractive index of silicon shifts the position of the second PSB to the short wavelength according to

$$\frac{2\lambda_2}{\lambda_1} = \sqrt{\frac{\bar{\epsilon}(\lambda_2)}{\bar{\epsilon}(\lambda_1)}} \quad (3.18)$$

Using $f = 0.74$ for an fcc lattice, $n_S = 1.4$, and $n_{Si}(\lambda_1) = 3.5$ we obtain $n_{Si}(\lambda_2) = 4.4$ at $\lambda_2 = 480$ nm, which is in excellent agreement with data from literature [40].

3.7.2 Optical switching at high optical excitation

At positive delays, the reflectivity spectra change dramatically. Figures 3.7(a) and (c), demonstrate photo-induced changes in the Bragg reflectivity at $\Delta t = 0.3$ ps (dashed curve) and $\Delta t = 2$ ps by dashed and dotted curves, respectively. For clarity, the corresponding relative changes of the reflectivity $\Delta R_d/R_d$ are also shown in Figs. 3.7(b) and (d). It is clear, that the amplitude of $|\Delta R_d/R_d|$ is enhanced in the spectral region of the PSBs and reaches values as high as 46% at 785 nm. At this wavelength a significant recovery can be observed at $\Delta t=2$ ps. In addition, at $\Delta t=0.3$ ps we observe a small blue-shift of the second order PSB peak, which also returns to the initial position for $\Delta t = 2$ ps.

As was already pointed out in Sec. 3.6, the changes in reflectivity are governed by increased absorption induced by hot carriers. This generates rapid switching of the *amplitude* of the reflectivity peak of the opal. The changes in the real part of the silicon refractive index, however, result in a *shift* of the second order PSB position at $\Delta t=0.3$ ps [Fig. 3.7(c), dashed line]. The amplitude of the dynamic shift of the PSB position can be estimated by the relation

$$\frac{\Delta\lambda_2}{\lambda_2} = \sqrt{\frac{\Delta\bar{\epsilon}(\lambda_2)}{\bar{\epsilon}(\lambda_2)}} \quad (3.19)$$

Using Eq. (3.17) and inserting $n_{Si}(\lambda_2) = 4.4$, we obtain a shift $\Delta\lambda = -2$ nm, which is in agreement with experiment within instrumental errors.

The fast recovery of the real part of the silicon refractive index, which results in a back shift of the PSB position [Fig. 3.7(c), dotted line], has been observed earlier in experiments with silicon films and attributed to carrier relaxation via phonon emission [16, 26, 42]. The emitted phonons, namely, lead to an increase of the lattice temperature that affect the refractive index of silicon over pico- and nanoseconds time scales [26].

3.8 Conclusions

In conclusion, we have demonstrated ultrafast switching of the PSB in an opal-silicon composite. In case of relatively weak excitation pulses ($70 \mu\text{J}/\text{cm}^2$), we measured photoinduced changes for the Bragg diffraction intensity up to $\sim 1\%$, much higher than relative changes in the specular reflectance from the surface. The switching of the Bragg reflectivity is controlled by photo-excited free carriers and can be as fast as 30 fs. Our results are in agreement with a theoretical model that properly takes into account surface effects and multiple scattering in the 3D photonic crystal. We showed that the photo-induced changes are enhanced in the spectral regions of PSBs and may reach values as high as 46% at high excitation power ($5 \text{ mJ}/\text{cm}^2$). Our results show a way to control the photonic band structure in 3D photonic crystal on the femtosecond time scale. This result is promising and perhaps relevant for a variety of applications, including switching of spontaneous emission.

References

- [1] T. F. Krauss and R. M. D. L. Rue, *Prog. Quantum Electron.* **23**, 51 (1999).
- [2] V. P. Bykov, *Sov. J. Quantum Electron.* **4**, 861 (1975).
- [3] E. Yablonovitch, *Phys. Rev. Lett.* **58**, 2059 (1987).
- [4] P. M. Johnson, A. F. Koenderink, and W. L. Vos, *Phys. Rev. B* **66**, 081102(R) (2002).
- [5] Y.-K. Ha, J.-E. Kim, H. Park, C.-S. Kee, and H. Lim, *Phys. Rev. B* **66**, 075109 (2002).
- [6] A. Haché and M. Bourgeois, *Appl. Phys. Lett.* **77**, 4089 (2000).
- [7] S. W. Leonard, H. M. van Driel, J. Schilling, and R. Wehrspohn, *Phys. Rev. B* **66**, 161102(R) (2002).
- [8] G. Pan, R. Kesavamoorthy, and S. A. Asher, *Phys. Rev. Lett.* **78**, 3860 (1997).
- [9] A. V. Akimov, A. V. Virchenko, V. G. Golubev, A. A. Kaplyanskii, D. A. Kurdyukov, A. B. Pevtsov, and A. V. Shcherbakov, *Phys. Solid State* **45**, 240 (2003).
- [10] D. A. Mazurenko, R. Kerst, J. I. Dijkhuis, A. V. Akimov, V. G. Golubev, D. A. Kurdyukov, A. B. Pevtsov, and A. V. Sel'kin, *Phys. Rev. Lett.* **91**, 213903 (2003).
- [11] C. M. Soukoulis, *Photonic Crystals and Light Localization in the 21st Century*, vol. 653 of *Nato Advanced Studies Institute, Series C: Mathematical and Physical Sciences* (Kluwer, Dordrecht, 2001).
- [12] Y. A. Vlasov, X. Z. Bo, J. C. Sturm, and D. J. Norris, *Nature (London)* **414**, 289 (2001).
- [13] M. Hase, M. Kitajima, A. M. Constantinescu, and H. Petek, *Nature (London)* **426**, 51 (2003).
- [14] M. Sheik-Bahae, D. C. Hutchings, D. J. Hagan, and E. W. V. Stryland, *IEEE J. Quantum Electron.* **27**, 1296 (1991).

- [15] S. Wang, *Solid-State Electronics* (New-York, 2001), p. 393.
- [16] A. Esser, K. Seibert, H. Kurz, G. N. Parsons, C. Wang, B. N. Davidson, G. Lucovsky, and R. J. Nemanich, *Phys. Rev. B* **41**, 2879 (1990).
- [17] K. Sokolowski-Tinten and D. von der Linde, *Phys. Rev. B* **61**, 2643 (2000).
- [18] R. Buhleier, G. Lüpke, G. Marowsky, Z. Gogolak, and J. Kuhl, *Phys. Rev. B* **50**, 2425 (1994).
- [19] A. J. Sabbah and D. M. Riffe, *Phys. Rev. B* **66**, 165217 (2002).
- [20] T. Sjödin, H. Petek, and H.-L. Dai, *Phys. Rev. Lett.* **81**, 5664 (1998).
- [21] K. E. Myers, Q. Wang, and S. L. Dexheimer, *Phys. Rev. B* **64**, 161309(R) (2001).
- [22] J. O. White, S. Cuzeau, D. Hulin, and R. Vanderhaghen, *J. Appl. Phys.* **84**, 4984 (1998).
- [23] J. R. Goldman and J. A. Prybyla, *Phys. Rev. Lett.* **72**, 1364 (1994).
- [24] I. A. Shkrob and R. A. Crowell, *Phys. Rev. B* **57**, 12207 (1998).
- [25] A. Mourchid, R. Vanderhaghen, D. Hulin, and P. M. Fauchet, *Phys. Rev. B* **42**, 7667 (1990).
- [26] A. Esser, H. Heesel, H. Kurz, C. Wang, G. N. Parsons, and G. Lucovsky, *J. Appl. Phys.* **73**, 1235 (1993).
- [27] O. B. Wright, U. Zammit, M. Marinelli, and V. E. Gusev, *Appl. Phys. Lett.* **69**, 553 (1996).
- [28] V. G. Golubev, J. L. Hutchison, V. A. Kosobukin, D. A. Kurdyukov, A. V. Medvedev, A. B. Pevtsov, J. Sloanc, and L. M. Sorokin, *J. Non-Cryst. Solid.* **299-302**, 1062 (2002).
- [29] V. G. Golubev, V. A. Kosobukin, D. A. Kurdyukov, A. V. Medvedev, and A. B. Pevtsov, *Semiconductors* **35**, 680 (2001).
- [30] D. L. Staebler and C. R. Wronski, *Appl. Phys. Lett.* **31**, 292 (1977).
- [31] V. Klimov, D. McBranch, and V. Karavanskii, *Phys. Rev. B* **52**, R16989 (1995).
- [32] K. W. K. Shung and Y. C. Tsai, *Phys. Rev. B* **48**, 11265 (1993).
- [33] R. D. Meade, K. D. Brommer, A. M. Rappe, and J. D. Joannopoulos, *Phys. Rev. B* **44**, 10961 (1991).
- [34] F. Ramos-Mendieta and P. Halevi, *Phys. Rev. B* **59**, 15112 (1999).
- [35] H. Richter and L. Ley, *J. Appl. Phys.* **52**, 7281 (1981).
- [36] Y. He, C. Yin, G. Cheng, L. Wang, X. Liu, and G. Y. Hu, *J. Appl. Phys.* **75**, 797 (1994).
- [37] N. A. R. Bhat and J. E. Sipe, *Phys. Rev. E* **64**, 056604 (2001).
- [38] D. A. Mazurenko, A. V. Akimov, A. B. Pevtsov, D. A. Kurdyukov, V. G. Golubev, and J. I. Dijkhuis, *J. Lumin.* **108**, 163 (2004).
- [39] D. A. Mazurenko, R. Kerst, A. V. Akimov, A. B. Pevtsov, D. A. Kurdyukov, V. G. Golubev, A. V. Sel'kin, and J. I. Dijkhuis, *J. Non-Cryst. Solids* **338-340**, 215 (2004).
- [40] D. E. Aspnes and A. A. Studna, *Phys. Rev. B* **27**, 985 (1983).
- [41] R. Biswas, M. M. Sigalas, G. Subramania, and K.-M. Ho, *Phys. Rev. B* **57**, 3701 (1998).
- [42] P. M. Fauchet and D. Hulin, *J. Opt. Soc. Am. B* **6**, 1024 (1989).

CHAPTER 4

SHIFTING OF A STOP-BAND INDUCED BY AN ULTRAFAST PHASE TRANSITION IN VANADIUM DIOXIDE

Abstract

We demonstrate ultrafast shifting of a photonic stop band driven by a photo-induced phase transition in a vanadium-dioxide (VO_2) forming a three-dimensional photonic crystal. An ultrashort laser pulse (120 fs) induces a phase transition in VO_2 residing in the pores of an artificial silica opal, and changes the effective dielectric constant of the opal. As a result, the spectral position of the photonic stop band blue-shifts leading to large changes in the reflectivity. The observed switching of the photonic crystal appears to be faster than 350 fs. The demonstrated properties of this opal- VO_2 composite may become relevant for potential applications in all-optical switches, optical memories, low-threshold lasers, and optical computers.

4.1 Introduction

The main goal of photonics is to design optical devices working similarly to traditional electronic devices but without the need of electrical contacts and much faster. In a photonic crystal a forbidden gap for photons may form a so-called photonic stop band (PSB), where light with a wavelength close to the period of modulation cannot propagate in certain directions [1]. In case of sufficient dielectric contrast, a complete photonic band gap may be realized, where light cannot propagate in any direction [2–4]. The spectral position and width of such a PSB in three-dimensional (3D) photonic crystals depends on the complex refractive index, which can be modified by some external impact. To date, numerous schemes have been tested experimentally that allow for external control over the PSB spectral position in 3D photonic crystals on a time scale up to nanoseconds, e.g. applying an external electric field [5–8], optical excitation [9], and temper-

ature variation [10–14]. Exceptionally large shifts of the PSB can potentially be reached taking advantage of structural phase transitions of one or more materials forming the photonic crystal. For example, Zhou *et al.* [11] recently demonstrated a small PSB shift induced by a ferroelectric phase transition. However, the largest observed shift of the PSB, was demonstrated in a photonic crystal formed of a SiO₂ opal filled with VO₂ by virtue of the semiconductor-metal phase transition in this compound [12].

Unfortunately, tuning the PSB by a temperature variation is impractically slow. In practice, optical excitation is by far the fastest way to control the PSB properties. Recently, ultrafast switching of one- [15], two- [16, 17] and three-dimensional [18, 19] photonic crystals via photo-excited free-carriers was demonstrated on the femtosecond timescale. In a 3D photonic crystal built from an opal-Si composite we demonstrated switching times shorter than 30 fs, the fastest switching ever reported (see Chapter 3). Unfortunately, a large increase of the imaginary part of the refractive index cannot be avoided in these samples and masks effects of the PSB shifting. Thus, demonstration of optical shifting of the PSB spectral position on the femtosecond time scale remains to be demonstrated in 3D photonic crystals [20, 21].

In this Chapter we explore a novel scenario of ultrafast switching in opals filled with VO₂ and demonstrate that the shift of the PSB can be made both large and fast. We report subpicosecond *shifting* of the PSB associated with a photoinduced phase transition of VO₂ [22]. Quite importantly, the imaginary part of the dielectric constant $\tilde{\epsilon}''$ of VO₂ is essentially independent of the crystal phase and, in contrast to the case of opal-Si, the PSB reflectivity intensity does not vanish under an optical excitation.

4.2 Ultrafast phase transitions in solids

Ultrafast phase transitions followed by femtosecond high-power optical excitation were intensively studied during the past two decades. Time-resolved second harmonic generation and reflectivity of silicon [23–25], gallium arsenide [24, 26–28], carbon [29], and indium antimonide [30] revealed pico- and subpicosecond dynamics associated with melting the lattice. Unfortunately, optical measurements provide only indirect information about the structural dynamics. For example, on the femtosecond timescale, the reflectivity changes associated with a structural transition can be masked by an intense electron-hole plasma that changes the dielectric constant of the studied material [24, 25]. Direct evidence for phase transitions to occur on a subpicosecond time scale, however, was obtained in time-

resolved x-ray measurements [31, 32].

It was established that large changes in the reflectivity and x-ray diffraction associated with a lattice transformation, occur only when the fluence of the excitation pulse exceeds a certain threshold. When the fluence is slightly above this threshold, the phase transition appears to take 10 – 100 ps, which is consistent with the classical thermodynamic picture of melting. For higher fluences the dynamics of melting rapidly accelerates and transition time drops below 1 ps at fluences only a few times higher than the threshold value [24]. The precise mechanism of such ultrafast phase transitions is under controversial debate. Obviously, a phase transition can be caused by the heat generated by the energy relaxation of photoexcited carriers to the lattice. However, the observed subpicosecond melting is much faster than the typical thermalization time of phonons [33] except, perhaps, longitudinal optical (LO) phonons that indeed happen to be relevant because exactly these phonon drive the phase transition [31]. In semiconductors the characteristic time of LO phonon emission from hot electrons can be as short as few tens of femtoseconds. Most likely, the phase transition is governed by non-equilibrium phonons created by hot carriers. This idea is supported by observations of large coherent oscillations of the lattice at the frequency corresponding to the LO phonon. These oscillations were observed both in optical [34–37] and x-ray experiments [32], and appear only at the fluences below the melting threshold. As soon as the fluence exceeds this threshold, the amplitude of LO oscillation surpasses the Lindemann stability limit [38] and the oscillations quench. In another report, van Vechten and co-workers [39, 40] proposed that the high-density electron-hole plasma may screen the atomic potentials and destabilize the crystal lattice leading to the phase transition. This screening is thought to appear immediately after optical excitation. In case of a highly dense electron-hole plasma ($\geq 10^{22} \text{ cm}^{-3}$), this model predicts a rapid disordering within one cycle of the LO phonon [41–43].

Optically induced structural phase transitions in vanadium dioxide may be governed by similar scenarios [44]. Here, the phase transition appears at 800-nm excitation when the fluence exceeds $\sim 7 \text{ mJ/cm}^2$, which is much less than the melting threshold. At this excitation level, the phase transition needs about 50 ps to develop. For higher fluences, say 25 mJ/cm^2 , the phase transition rapidly speeds up and occurs within 100 fs. In the following section we supply all relevant information about the phase transition in VO_2 under static conditions.

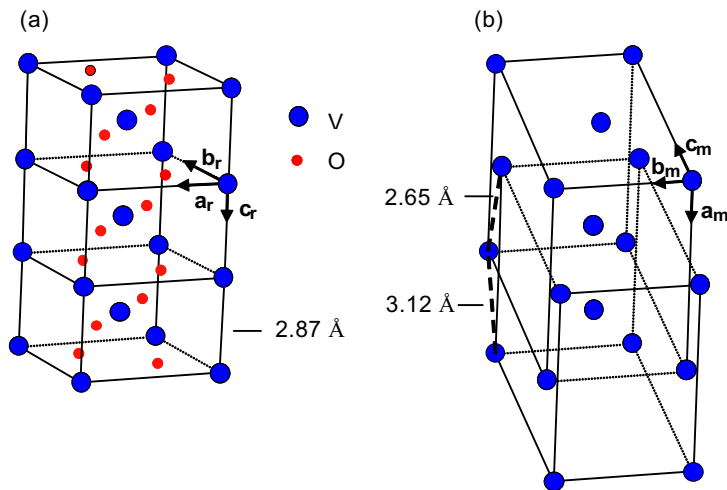


FIGURE 4.1 Crystal structure of vanadium dioxide. (a) Rutile structure in the metallic phase, i.e. at $T > T_c$. (b) Monoclinic structure in semiconducting phase at $T < T_c$. Positions of the oxygen atoms in the monoclinic phase are virtually the same as in the rutile phase and not shown.

4.3 Phase transition in VO₂

In contrast to other vanadium oxides, VO₂ exists exclusively in a narrow stoichiometric range VO_{2- δ} ($\delta < 0.006$). At $T_t = 68^\circ\text{C}$, VO₂ possesses a first-order phase transition from the semiconducting ($T < T_t$) to the metallic ($T > T_t$) phase [45]. The phase transition requires a heat absorption of $\Delta H_t \sim 4 \text{ kJ/mol}$ [46]. Figure 4.1 illustrates the spatial positions of vanadium (grey dots) and oxygen (full dots) atoms in the “hot” [Fig. 4.1(a)] and the “cold” [Fig. 4.1(b)] phases, respectively. The displacement of the oxygen atoms [not shown in Fig. 4.1(b)] at the phase transition appears to be much smaller than the displacement of the vanadium atoms. Above the transition temperature, VO₂ has the rutile structure and the distance between nearest-neighbor vanadium atoms is 2.87 Å [Fig. 4.1(a)]. Below the transition temperature, the position of the vanadium atoms deviates slightly from the high-temperature position leading to an irregular coordination of vanadium atoms: the shortest V-V distance equals 2.65 Å, while longer V-V distance is 3.12 Å [Fig. 4.1(b)]. Quite importantly, the volume expansion at the phase transition is very small, $\Delta V/V < 0.1\%$, which makes this material very convenient as a filling substance [46]. The phase transition results in the formation

of a monoclinic lattice composed of two shifted sublattices [Fig. 4.1(b)]. Lowering the crystal symmetry leads to a band gap for electrons, and VO₂ becomes a semiconductor. The relation between the high- and low-temperature phases can be visualized in terms of translation vectors of the high-symmetric rutile phase. The primitive translation vectors of VO₂ rutile structure are orthogonal and equal to $a_r = b_r = 4.53 \text{ \AA}$ and $c_r = 2.87 \text{ \AA}$. The crystallographic transformation at T_t can be represented by

$$\mathbf{a}_m \leftrightarrow 2\mathbf{c}_r, \quad \mathbf{b}_m \leftrightarrow 2\mathbf{c}_r, \quad \mathbf{c}_m \leftrightarrow \mathbf{a}_r - \mathbf{c}_r,$$

where \mathbf{a}_m , \mathbf{b}_m , and \mathbf{c}_m are the primitive translation vectors of the monoclinic lattice with $a_m = 5.74 \text{ \AA}$, $b_m = 4.52 \text{ \AA}$, and $c_m = 5.38 \text{ \AA}$. The angle between \mathbf{a}_m and \mathbf{c}_m is $\beta = 122.6^\circ$.

The idea of using VO₂ as a filling material of opals is inspired by the fact that the phase transition in VO₂ is accompanied by a substantial change in the real part of the dielectric constant from $\epsilon'_c(\text{VO}_2) = 8$ in the “cold” semiconductor phase to $\epsilon'_h(\text{VO}_2) = 6$ in the “hot” metallic phase, for the red spectral region [47, 48]. Quite importantly as stressed earlier, the corresponding change in the imaginary part is weak. The idea of our experiment is to achieve ultrafast control over the PSB position in opal-VO₂ by optically inducing a phase transition in VO₂.

4.4 Opal-VO₂ and experimental details

Our opal-VO₂ was fabricated in the Ioffe Physico-Technical Institute in St. Petersburg, Russia. The sample was synthesized from an opal template composed of close-packed (fcc) mono-dispersed ($\pm 5\%$) silica spheres of $0.23 \pm 5 \mu\text{m}$ in diameter. The template had a polydomain structure. The size of the highly-ordered domains was of the order of $30 - 100 \mu\text{m}$. The voids of the opal template were first filled with a solution of vanadium pentoxide in nitric acid and then subsequently reduced to VO₂ by high temperature annealing in vacuum. The details of the fabrication method can be found in Refs. [12, 49]. The (1 1 1) plane of the photonic crystal makes an angle of several degrees with the polished sample surface. This allowed us to separate the ordinary surface reflection from the Bragg diffraction from the (1 1 1) planes of the 3D photonic crystal by simply passing the reflected beam via a spatial filter that blocks the specular light, but captures the Bragg-diffracted light [19].

The sample was mounted on a copper holder supplied with an internal heater, allowing us to vary the sample temperature in a range of $20 - 150^\circ\text{C}$. The tem-

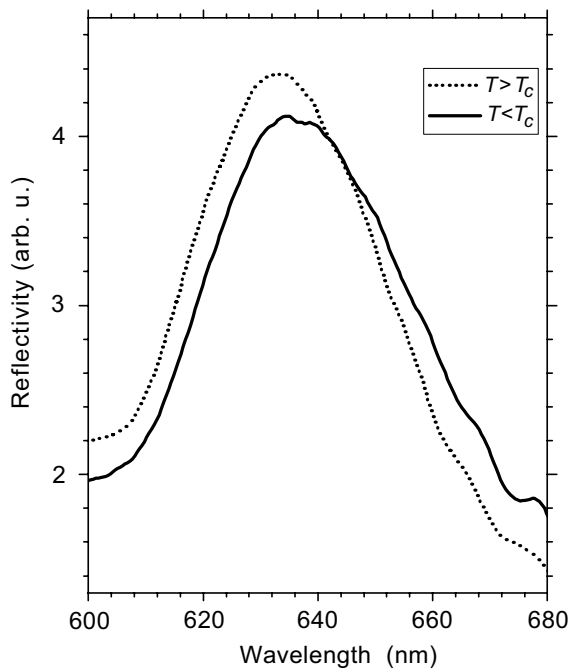


FIGURE 4.2 Stationary Bragg reflection spectra of opal-VO₂ below (solid line) and above (dotted line) the transition temperature of VO₂. Peak is the first-order PSB.

perature of the sample was monitored by a calibrated semiconductor thermistor placed close to the sample. The stationary spectra at different temperatures were obtained by reflection of a beam of white light continuum pulses, in absence of a pump on the sample.

Time-resolved reflection spectra were taken at room temperature using the 1-kHz pump-probe setup described in Chapter 2.2. In brief, the pump pulse was focused onto a 400- μm spot at the sample surface with a surface energy density of 10 mJ/cm². The optical pulse is absorbed in VO₂ in the opal voids, and is to produce a rapid phase transition of VO₂. The power density used in the experiment was chosen just above the threshold, on which the phase transition is known to occur [44]. At the phase transition, the mean refractive index of the photonic crystal rapidly changes, and the position of the PSB shifts. The time-resolved reflection spectrum was monitored by a weak ultrafast, white light continuum probe pulse generated in a thin sapphire plate, excited by the same Ti-sapphire laser. In order to reject the residual 800-nm light, the white light was passed via

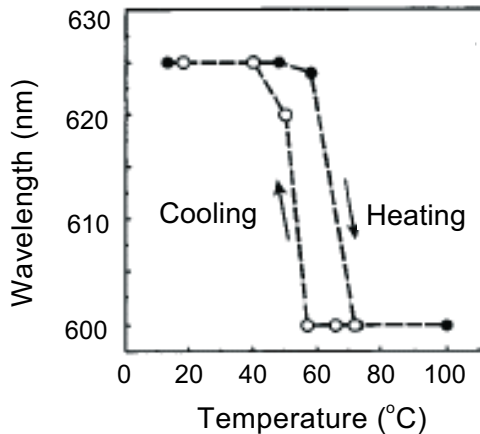


FIGURE 4.3 Spectral position of the PSB of opal-VO₂ during the sample heating and cooling. This picture is taken from Ref. [12].

an optical band-pass filter (580 – 710 nm). The probe pulse propagating close to the [1 1 1] direction of the photonic crystal was focused onto a 25- μm spot at the sample surface within the area illuminated by the pump.

4.5 Ultrafast band-shifting

4.5.1 Linear optical properties

Figure 4.2 shows typical stationary Bragg reflection spectra taken below and above the transition temperature as indicated by solid and dashed lines, respectively. The Bragg reflection spectrum in the direction perpendicular to the (1 1 1) surface, consists of one maximum that corresponds to the first-order PSB. As soon as the temperature passes the transition point, the spectral position of the Bragg reflection maximum, λ , shifts over 4 nm towards the short wavelengths. The maximum shift observed for other samples can be as much as 40 nm [12] and possesses a hysteresis (Fig. 4.3) In addition, the spectral position of λ appears to vary over the sample surface, possibly due to the variation of the filling factor and the presence of vanadium oxide of other stoichiometry. Further details of the linear optical properties of VO₂ can be found in Ref. [49] together with a calculation of the reflectivity near the first order PSB using the two-band-mixing theory described in Section 3.5.

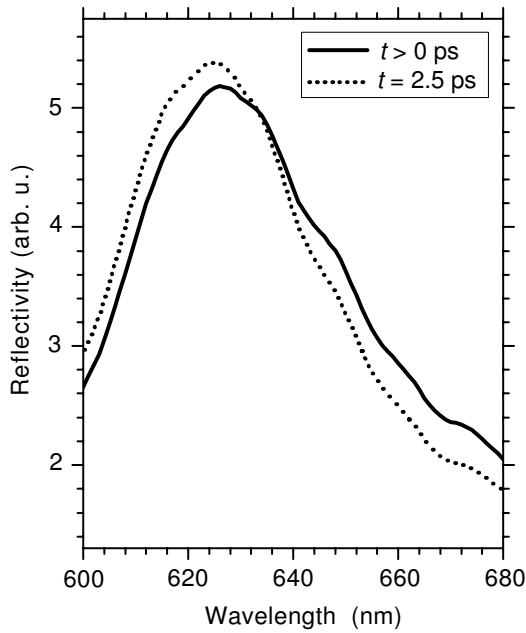


FIGURE 4.4 Bragg reflection spectra of opal-VO₂ prior (solid line) and following (dotted line) a 10-mJ/cm² pump pulse.

4.5.2 Nonlinear optical properties

In Fig. 4.4(a) the ultrafast shift of the PSB is shown induced by a strong pump pulse. Here, solid and dashed lines correspond to the Bragg reflection spectrum measured just *before* and 2.5 ps *after* the optical excitation, respectively. It appears that the optical excitation induces a rapid shift of the PSB towards the short wavelengths. Moreover, the magnitude of the transient optically induced shift of the PSB turns out to coincide with the thermally induced one, observed under stationary conditions (Fig. 4.2).

Figure 4.5 shows the spectral-temporal evolution of the Bragg reflectivity. Colors indicate relative changes of the reflectivity, $\Delta R/R$: red an increase, blue a decrease, and green no changes of the intensity. Of course, no differences in reflectivity are observed prior to the arrival of the pump pulse. At zero delay, when the pump pulse arrives, the intensity slightly decreases, most significantly at the long-wavelength side of the PSB. At 200-fs delay, however, $\Delta R/R$ changes drastically and rapidly *increases* on the short-wavelength side and *decreases* on

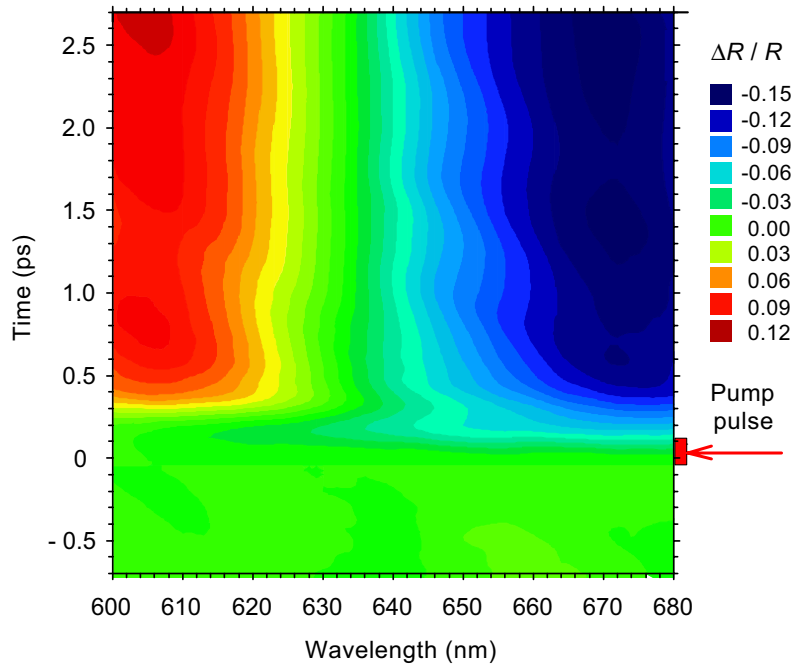


FIGURE 4.5 Spectral-temporal evolution of the relative changes of the Bragg reflectivity. Colors indicate the signal amplitude. Rectangle on the right indicates the arrival time and duration of the pump pulse.

the long-wavelength side. This signals rapid shifting of the PSB. Within half a picosecond, the transition is completed and the amplitude of the differential Bragg reflectivity reaches $\Delta R/R = 0.12$ at 605 nm and $\Delta R/R = -0.15$ at 670 nm. In this connection we note that the observed change in the differential reflection may reach values as high as $\Delta R/R = -0.35$ on other sample points. At longer delays the reflectivity remains virtually constant over at least hundreds of picoseconds. This time is determined by the cooling down of the excited volume and takes as long as $100 \mu\text{s}$ in such samples [50]. No significant ultrafast changes in the reflectivity spectra were observed in case the sample was held above the transition temperature, confirming that the rapid shifting is induced by the phase transition. Further, these remarkable shifts of the PSB were exclusively [44] observed when the pump power density exceeded the threshold of $5 - 10 \text{ mJ/cm}^2$. Above 50 mJ/cm^2 , irreversible changes in the reflectivity spectra are observed possibly due to chemical reactions and surface damage.

Figure 4.6 (a) displays as solid lines the observed switching dynamics of $\Delta R/R$ at the short-wavelength (610 nm) wing, at the long-wavelength (670 nm) wing, near the maximum (630 nm) of the PSB, and at an intermediate spectral position (640 nm). Beyond delays of ~ 500 fs, $\Delta R/R$ reaches the stationary values $A(\lambda)$, indicated in Fig. 4.6(a) as horizontal arrows. Further, the leading edge at the short-wavelength side is delayed with respect to the pump pulse by a few hundred femtoseconds. At 630 nm the time span over which the differential reflection changes is approximately equal to the duration of the pump pulse and turns out to be the fastest feature in the time-dependent reflection spectra. The dynamics of the phase transition, which is the main contribution to $\Delta R(t)/R$ at the short- and the long-wavelength side of the PSB, appears to be slower. The observed switching times, taken at the time the reflectivity reaches 50% of its full amplitude, equal to 350 fs at $\lambda = 605$ nm and 200 fs at $\lambda = 670$ nm.

4.6 Discussion

The origin of the ultrafast shift of the PSB (Fig. 4.4) in our opal-VO₂ photonic crystal is a photo-induced phase transition of VO₂. The wavelength of the reflection maximum in the reflectivity spectrum of the opal, λ_m , can be estimated from $\lambda_m = 2d\tilde{n}'$, where d is the distance between the layers of spheres and \tilde{n}' the real part of the effective refractive index of the opal. As soon as the temperature reaches T_t , the value of $n(\text{VO}_2)$ decreases. This results in a rapid change of \tilde{n}' leading to a short-wavelength shift the PSB spectral position, as observed. Consequently, $\Delta R/R$ increases on the short-wavelength and decreases on the long-wavelength wings of the PSB (Fig. 4.2). Strikingly, the amplitude of $|\Delta R/R|$ is higher at the long-wavelength side of the PSB spectrum than at the short-wavelength side. This phenomenon can be readily explained by a reduction of the refractive index contrast of the photonic crystal when VO₂ turns from the dielectric into the metallic phase. The reduction of the refractive index contrast, namely, leads to narrowing of the PSB and, consequently, results in a larger amplitude of $\Delta R/R$ at long wavelengths.

In case the dynamics of the PSB shifting is exclusively controlled by the phase transition, one would expect no wavelength-dependence in $\Delta R(t)/R$. However, the dynamics at short and long wavelength sides of the PSB appears to be different [Fig. 4.6(a)]. At $\lambda = 670$ nm, $\Delta R/R$ monotonically decreases, while at $\lambda = 605$ nm $\Delta R/R$ is negative during the first 200 fs and subsequently changes sign. Such behavior indicates the presence of two independent contributions governing the refractive index of the photonic crystal. The first is the already described phase

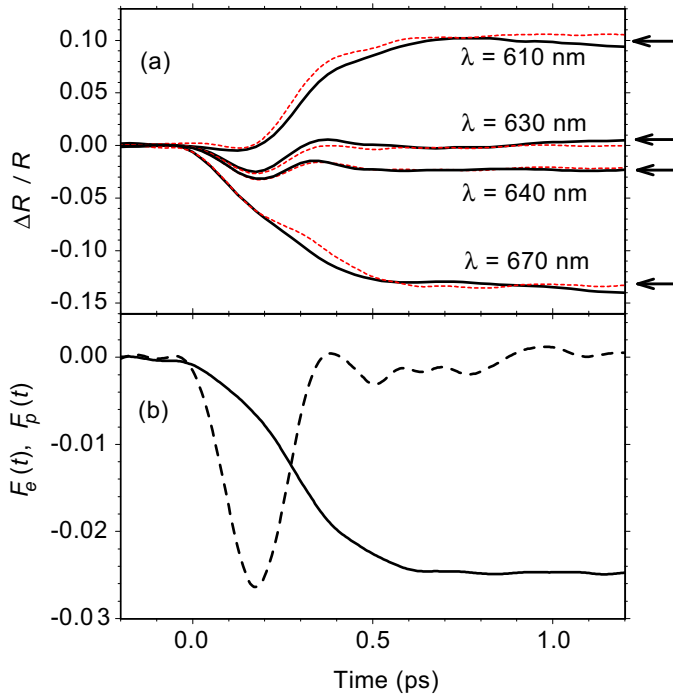


FIGURE 4.6 (a) Transient Bragg reflection signal at 610, 630, 640, and 670 nm, respectively. Black solid lines shows the experimental data, red dotted lines the calculated $F_e(t) + A(\lambda)F_p(t)$; (b) $F_e(t)$ and $F_p(t)$ depicted by dashed and solid lines, respectively. $F_p(\lambda)$ is shown in arbitrary units.

transition. The second is light absorption by photoexcited carriers in VO_2 and (or), perhaps, two-photon absorption in silica that may take place when pump and probe pulses are temporally overlapping ($t < 200$ fs) [51]. The induced absorption suppresses the Bragg interference in the photonic crystal (see Chapter 3) and explains the initial decrease of $\Delta R/R$ observed at all wavelengths. At longer time delays ($t > 200$ fs) the suppression of Bragg interference is compensated by the phase transition itself that tends to increase $\Delta R/R$ at the short-wavelength side of the spectrum. This explanation is supported by the observed weak $\Delta R(t)/R$ signals at $\lambda = 630$ nm [Fig. 4.6(a)], close to the center of the PSB where $A(\lambda) \sim 0$. Here, $\Delta R(t)/R$ is essentially independent of the PSB shift induced by the phase transition, and only affected by small photoinduced changes in the imaginary part of the refractive index.

In the analysis, that we present now, we assume that the observed differential change in the Bragg reflectivity is a sum of two contributions: (i) the phase transition, characterized by $A(\lambda) F_p(t)$, and (ii) the generation and decay of photo-excited carriers, characterized by the wavelength-independent function $F_e(t)$. These functions can be extracted from the data by subtracting and summing, respectively, the experimental curves of $\Delta R/R(\lambda, t)$ measured at two different wavelengths, for each combination of curves,

$$\begin{aligned}
 F_e(t) &= \frac{1}{2} \left[\frac{\Delta R}{R}(\lambda_1, t) + \frac{\Delta R}{R}(\lambda_2, t) \right], \\
 A(\lambda) F_p(t) &= \left[\frac{\Delta R}{R}(\lambda_1, t) - \frac{\Delta R}{R}(\lambda_2, t) \right] \frac{\Delta R}{R}(\lambda, t > t_s) \\
 &\quad \times \left[\frac{\Delta R}{R}(\lambda_1, t > t_s) - \frac{\Delta R}{R}(\lambda_2, t > t_s) \right]^{-1}
 \end{aligned} \tag{4.1}$$

where λ_1 and λ_2 are arbitrary wavelengths. We note, that $A(\lambda) F_p(t)$ and $F_e(t)$ are essentially independent of the λ_1 and λ_2 chosen. The calculated $F_e(t)$ and $F_p(t)$ are shown in Fig. 4.6(b) by red dashed and solid lines, respectively. The experimental dependencies of $\Delta R(t)/R$ depicted in Fig. 4.6(a) (black solid lines) can be compared to the sum of $F_e(t)$ and $A(\lambda) F_p(t)$ (dotted lines). We obtain excellent agreement between the measured and the calculated curves. From the empirical curve $F_p(t)$, we estimate that the optically induced phase transition takes place at a 250-fs delay after the pump pulse. Finally, we note that the presence of two contributions in the dynamics is most clearly visible in the $\Delta R(t)/R$ dependence at 640 nm.

The observed dynamics of the phase transition is in agreement with two-step model proposed by Sokolowski-Tinten and co-workers [24]. According to this model, an electron-hole plasma is excited during the optical excitation while the transition, where atoms need time to reach their new spatial positions, occurs only with some delay. The observed delay is much shorter than the thermalization time of phonons and signifies that the phase transition cannot be described by thermal processes and must be a nonequilibrium process [33]. The phase transition in VO₂ can be governed by one of two mechanisms (or by both): (i) non-equilibrium LO phonons created by hot carriers and (ii) screening the electronic states by dense electron-hole plasma. The latter may change the electron band structure and diminish the energy barrier separating the two phases of VO₂ [44]. Unfortunately, the temporal resolution of our experiment is comparable with the observed dy-

namics of the structural transformation, $F_p(t)$. Therefore, we cannot distinguish the roles of these two mechanisms in our experiment. We hope that future experiments with higher temporal resolution might resolve the decay of photoexcited carriers. For that to achieve, one, of course, needs to probe the slope of $F_p(t)$ with a time resolution shorter than the rise of $F_p(t)$. In any case, we may conclude that the electron-hole plasma produces a non-equilibrium energy distribution of phonons that promote the phase transition.

4.7 Conclusion

We demonstrated that a 3D photonic crystal based on vanadium dioxide is a promising material for ultrafast photonic applications. The shift of the PSB in opal-VO₂ was observed to take place on the subpicosecond time scale. The relative change in the Bragg reflectivity was demonstrated to be as much as 35%. The effect is attributed to the modulation of the real part of the effective dielectric constant of the photonic crystal due to an ultrafast phase transition in VO₂. Further, the high refractive index of VO₂ and the possibility of fabrication of inverted VO₂ opals [49] make this material a candidate for all-optical switching applications. Indeed, in the near infrared region, i.e. 1.5 μm (Telecom standard), the refractive index is 3.5 in the semiconductor phase [47] high enough [2] to create a photonic device capable of ultrafast switching of a complete photonic bandgap.

Already at the low concentration of VO₂ in the opal voids ($\sim 8\%$) in our sample, substantial ultrafast shifts (~ 5 nm) of the PSB were reached. In nanosecond experiments and in other opal samples with a higher concentration of VO₂ in the pores, spectral shifts up to 40 nm were recently observed, quite sizable relative to the PSB bandwidth [49, 50]. This suggests that ultrafast control of light in VO₂-based photonic crystals may prove to be relevant for applications.

References

- [1] C. M. Soukoulis, *Photonic Crystals and Light Localization in the 21st Century*, vol. 653 of *Nato Advanced Studies Institute, Series C: Mathematical and Physical Sciences* (Kluwer, Dordrecht, 2001).
- [2] R. Biswas, M. M. Sigalas, G. Subramania, and K.-M. Ho, *Phys. Rev. B* **57**, 3701 (1998).
- [3] A. Blanco, E. Chomski, S. Grachtchak, M. Ibisate, S. John, S. W. Leonard, C. Lopez, F. Meseguer, H. Miguez, J. P. Mondia, et al., *Nature (London)* **405**, 437 (2000).
- [4] Y. A. Vlasov, X. Z. Bo, J. C. Sturm, and D. J. Norris, *Nature (London)* **414**, 289 (2001).

-
- [5] D. Kang, J. E. Maclennan, N. A. Clark, A. A. Zakhidov, and R. H. Baughman, *Phys. Rev. Lett.* **86**, 4052 (2001).
- [6] Q.-B. Meng, C.-H. Fu, S. Hayami, Z.-Z. Gu, O. Sato, and A. Fujishima, *J. Appl. Phys.* **89**, 5794 (2001).
- [7] Y. Shimoda, M. Ozaki, and K. Yoshino, *Appl. Phys. Lett.* **79**, 3627 (2001).
- [8] B. Li, J. Zhou, L. Li, X. J. Wang, X. H. Liu, and J. Zi, *Appl. Phys. Lett.* **83**, 4704 (2003).
- [9] G. Pan, R. Kesavamoorthy, and S. A. Asher, *Phys. Rev. Lett.* **78**, 3860 (1997).
- [10] K. Yoshino, Y. Shimoda, Y. Kawagishi, K. Nakayama, and M. Ozaki, *Appl. Phys. Lett.* **75**, 932 (1999).
- [11] J. Zhou, C. Q. Sun, K. Pita, Y. L. Lam, Y. Zhou, S. L. Ng, C. H. Kam, L. T. Li, and Z. L. Gui, *Appl. Phys. Lett.* **78**, 661 (2001).
- [12] V. G. Golubev, V. Y. Davydov, N. F. Kartenko, D. A. Kurdyukov, A. V. Medvedev, A. B. Pevtsov, A. V. Scherbakov, and E. B. Shadrin, *Appl. Phys. Lett.* **79**, 2127 (2001).
- [13] G. Mertens, T. Röder, R. Schweins, K. Huber, and H.-S. Kitzerow, *Appl. Phys. Lett.* **80**, 1885 (2002).
- [14] G. Mertens, T. Röder, H. Matthias, H. Marsmann, H.-S. R. Kitzerow, S. L. Schweizer, C. Jamois, R. B. Wehrspohn, and M. Neubert, *Appl. Phys. Lett.* **83**, 3036 (2003).
- [15] A. Haché and M. Bourgeois, *Appl. Phys. Lett.* **77**, 4089 (2000).
- [16] S. W. Leonard, H. M. van Driel, J. Schilling, and R. Wehrspohn, *Phys. Rev. B* **66**, 161102(R) (2002).
- [17] A. D. Bristow, J.-P. R. Wells, W. H. Fan, A. M. Fox, M. S. Skolnick, D. M. Whittaker, A. Tahraoui, T. F. Krauss, and J. S. Robert, *Appl. Phys. Lett.* **83**, 851 (2003).
- [18] X. Hu, Q. Zhang, Y. Liu, B. Cheng, and D. Zhang, *Appl. Phys. Lett.* **83**, 2518 (2003).
- [19] D. A. Mazurenko, R. Kerst, J. I. Dijkhuis, A. V. Akimov, V. G. Golubev, D. A. Kurdyukov, A. B. Pevtsov, and A. V. Sel'kin, *Phys. Rev. Lett.* **91**, 213903 (2003).
- [20] Y.-K. Ha, J.-E. Kim, H. Park, C.-S. Kee, and H. Lim, *Phys. Rev. B* **66**, 075109 (2002).
- [21] P. M. Johnson, A. F. Koenderink, and W. L. Vos, *Phys. Rev. B* **66**, 081102(R) (2002).
- [22] D. A. Mazurenko, R. Kerst, J. I. Dijkhuis, A. V. Akimov, V. G. Golubev, A. A. Kaplyanskii, D. A. Kurdyukov, and A. B. Pevtsov (2004).
- [23] C. V. Shank, R. Yen, and C. Hirlimann, *Phys. Rev. Lett.* **51**, 900 (1983).
- [24] K. Sokolowski-Tinten, J. Bialkowski, and D. von der Linde, *Phys. Rev. B* **51**, 14186 (1995).
- [25] K. Sokolowski-Tinten and D. von der Linde, *Phys. Rev. B* **61**, 2643 (2000).
- [26] S. V. Govorkov, T. Schröder, I. L. Shumay, and P. Heist, *Phys. Rev. B* **46**, 6864 (1992).
- [27] L. Huang, J. P. Callan, E. N. Glezer, and E. Mazur, *Phys. Rev. Lett.* **80**, 185 (1998).
- [28] K. Sokolowski-Tinten, J. Bialkowski, M. Boing, A. Cavalleri, and D. von der Linde, *Phys. Rev. B* **58**, 11805 (1998).

-
- [29] D. H. Reitze, H. Ahn, and M. C. Downer, *Phys. Rev. B* **45**, 2677 (1992).
- [30] I. L. Shumay and U. Höfer, *Phys. Rev. B* **53**, 15878 (1996).
- [31] A. Rouse, C. Rischel, S. Fourmaux, I. Uschmann, S. Sebban, G. Grillon, P. Balcou, E. Förster, J. P. Geindre, P. Audebert, et al., *Nature (London)* **410**, 65 (2001).
- [32] K. Sokolowski-Tinten, C. Blome, J. Blums, A. Cavalleri, C. Dietrich, A. Tarasevitch, I. Uschmann, E. Frster, M. Kammler, M. H. von Hoegen, et al., *Nature (London)* **422**, 287 (2003).
- [33] Y. B. Levinson, *Nonequilibrium Phonons in Nonmetallic Crystals* (Kluwer, North-Holland, Amsterdam, 1986), vol. 653 of *Nato Advanced Studies Institute, Series C: Mathematical and Physical Sciences*, p. 91.
- [34] G. C. Cho, W. Kütt, and H. Kurz, *Phys. Rev. Lett.* **65**, 764 (1990).
- [35] M. Hase, K. Mizoguchi, H. Harima, and S. Nakashima, *Phys. Rev. B* **58**, 5448 (1998).
- [36] M. Hase, M. Kitajima, S. Nakashima, and K. Mizoguchi, *Phys. Rev. Lett.* **88**, 067401 (2002).
- [37] A. J. Sabbah and D. M. Riffe, *Phys. Rev. B* **66**, 165217 (2002).
- [38] F. A. Lindemann, *Phys. Z.* **11**, 609 (1910).
- [39] V. Heine and J. A. van Vechten, *Phys. Rev. B* **13**, 1622 (1976).
- [40] J. A. van Vechten, R. Tsu, and F. W. Saris, *Phys. Lett. A* **74**, 422 (1979).
- [41] P. Stampfli and K. H. Bennemann, *Phys. Rev. B* **49**, 7299 (1994).
- [42] P. L. Silvestrelly, A. Alavi, M. Parrinello, and D. Finkel, *Phys. Rev. Lett.* **77**, 3149 (1996).
- [43] J. S. Graves and R. E. Allen, *Phys. Rev. B* **58**, 13627 (1998).
- [44] A. Cavalleri, C. Tóth, C. W. Siders, J. A. Squier, F. Ráksi, P. Forget, and J. C. Kieffer, *Phys. Rev. Lett.* **87**, 237401 (2001).
- [45] F. J. Morin, *Phys. Rev. Lett.* **3**, 34 (1959).
- [46] O. Madelung, M. Schulz, and H. Weiss, eds., *Landolt-Börnstein*, vol. 17 (New-York, 1984).
- [47] H. W. Verleur, A. S. Barker, and C. N. Berglund, *Phys. Rev.* **172**, 788 (1968).
- [48] M. F. Becker, A. B. Buckman, R. M. Walser, T. Lépine, P. Georges, and A. Brun, *J. Appl. Phys.* **79**, 2404 (1996).
- [49] V. G. Golubev, D. A. Kurdyukov, A. B. Pevtsov, A. V. Sel'kin, E. B. Shadrin, A. V. Il'inskii, and R. Boeyink, *Semiconductors* **36**, 1043 (2002).
- [50] A. V. Akimov, A. V. Virchenko, V. G. Golubev, A. A. Kaplyanskii, D. A. Kurdyukov, A. B. Pevtsov, and A. V. Shcherbakov, *Phys. Solid State* **45**, 240 (2003).
- [51] M. Sheik-Bahae, D. C. Hutchings, D. J. Hagan, and E. W. V. Stryland, *IEEE J. Quantum Electron.* **27**, 1296 (1991).

CHAPTER 5

LINEAR OPTICAL PROPERTIES OF A CORE-SHELL SILICA-GOLD PHOTONIC CRYSTAL

Abstract

We analyze the linear optical properties of a three-dimensional photonic crystal composed of close-packed $\text{SiO}_2/\text{Au}/\text{SiO}_2$ core-shell colloidal particles. Strong coupling between incident light and the surface plasmons of the spherical gold microcavities appears as sharp features in the observed reflectivity spectra in the visible. In a single layer of gold-shell particles, a highly directional diffraction pattern was observed with hexagonal symmetry. The results are compared with theory.

5.1 Introduction

Progress in the fabrication of self-assembled nanostructures that possess a well defined and controllable spatial periodicity explains the rapid growth and interest in research on photonic crystals. From the fundamental side it is stimulated by the challenging idea to control in a photonic crystal the spontaneous emission of atoms or radiative electron-hole recombination [1, 2]. However, photonic crystals are also thought to be relevant for various future applications ranging from telecommunication data processing to the realization of ultrafast switches, optical chips, and computers. In order to achieve full control over light flow in a photonic crystal, one needs to create structures with a complete photonic band gap – i.e. a material, in which light in some spectral range cannot propagate in any direction. A photonic band gap may arise in a three-dimensional (3D) photonic crystal, which possesses 3D periodicity in the dielectric constant on the scale of the wavelength of light. However, spatial ordering is not sufficient to form a band gap. The additional requirement is to reach a sufficiently high refractive index contrast between the host and dielectric structure. For example, the required

refractive index contrast to achieve a full bandgap for close-packed face-centered-cubic (fcc) lattice of spheres should exceed 2.8 (Refs. [3, 4]). A photonic crystal with a complete band gap was demonstrated for the first time by Yablonovitch and co-workers [5, 6] in the microwave range. The wavelength position of the photonic band gap was scaled all the way down to the infrared range by Blanco and co-workers [7]. They use a sample fabricated from a monodisperse suspension of colloidal microspheres that self-assemble into a 3D matrix with long-range periodicity. In such case, the most common approach to increase the refractive index contrast above the threshold is infiltrating the voids of the photonic crystal with high-index semiconductor materials. Subsequently, the contrast can be increased further by etching out the dielectric spheres [7]. For such inverted photonic crystals, the required refractive index contrast limits the material choice to highly refractive semiconductors, which are unfortunately opaque in the visible. Metallo-dielectric photonic crystals, however, are novel and very attractive alternatives in this context because of their high refractive index contrast. It was predicted that a large photonic band gap may open up in the visible in metallo-dielectric photonic crystals [8]. Further, metallo-dielectric photonic crystals turn out to be interesting objects from the point of view of fundamental optics and nano-plasmonics.

In fact, the first, very well known, and widely utilized periodic metallic structures are, of course, metallic gratings [9]. In 1902, Wood discovered anomalously sharp minima and maxima in the reflection spectra of metallic gratings [10]. Since that discovery, it took about 60 years to complete a theory that could account for all observed phenomena [11]. Roughly speaking, the anomalies can be traced back to the presence of the two resonances: (i) one in which the diffraction orders graze the surface of the grating (proposed by Rayleigh) [12] and (ii) the plasmon resonance. These resonances may even interfere with each other and produce a Fano-like profile of the reflectivity spectrum [13, 14]. At the end of the twentieth century, the interest in the metallic gratings was renewed by the work of Ebbesen and co-workers [15] who discovered unexpectedly high transmission through an array of sub-wavelength holes in a metal film, namely one-order-of-magnitude higher than predicted by standard aperture theory. This phenomenon was explained as follows: the incoming light excites the surface plasmons on the front side of the perforated film [16]. The excited plasmons subsequently tunnel via the holes to the other side of the film and, subsequently, radiate light into free space.

A related fascinating phenomenon takes place when light is transmitted through a suitably corrugated metal film having one single aperture of a size much smaller than the wavelength of light. Standard diffraction theory prescribes that light emerging from a sub-wavelength hole should be diffracted equally intense in

all directions. However, Lezec with co-workers [17] demonstrated that the outcoming beam from a hole in a corrugated film can be unexpectedly directional. The explanation of this phenomenon was found in the coupling of the plasmon resonance with the corrugation at the rear surface of the film. The direction and width of the outcoming beam can be controlled by the geometry of the structure and the incident wavelength. Very recently, Kramper and co-workers [18] showed both theoretically and experimentally, that a highly directional beam can be coupled out from a sub-wavelength waveguide even in a dielectric photonic crystal, demonstrating that these effects are not restricted to metallo-dielectric structures.

Recent progress in the synthesis of metallo-dielectric composites now allows us to fabricate periodic 2D or 3D arrays of metallo-dielectric core-shell particles with a lattice constant of the order of the wavelength of light in the visible [19]. An important additional feature of such structures compared to a dielectric photonic crystal is the presence of surface plasmon resonances, i.e. coherent oscillations of free electrons at optical frequencies in each individual particle. Therefore, the optical response of an ordered array of a dielectric-metal core-shell particles can be viewed as a superposition of the multiple lattice diffraction and surface plasmon resonances. The latter are determined by the geometry of the individual particle and the dielectric function of the metal.

The surface plasmon resonance of an isolated metallic sphere appears at wavelengths, where the dielectric constant of the metal, ϵ_m , is approaching $\epsilon_m = -2$. For a sphere of a size much smaller than the wavelength of light, the spectral position of the surface plasmon resonance is weakly size dependent. When the diameter of the sphere is comparable to the wavelength of light, the surface plasmon resonance shifts towards lower energies, becomes broader, and finally splits into a series of separate multipole modes. This phenomenon is caused by phase retardation [20, 21].

A hollow spherical metallic nanoshell supports two types of surface plasmons, one on the internal and one on the external surfaces of the sphere, respectively. In case of a sufficiently thin shell, the inner and outer plasmons may interact resulting in “hybridization” of the plasmon excitations [22]. In resonance one expects the plasmon mode to split into symmetrically and antisymmetrically coupled plasmon modes as shown in Fig. 5.1. Recently, hybridization of the plasmon modes was reported in very complex multishell particles composed of a silica core and consecutive shells of gold and silica [22]. In this particle the hybridization of the plasmon states is the result of a strong coupling of plasmon states in the inner and outer metal shells and appeared to be very sensitive to the thickness of the separating dielectric layer.

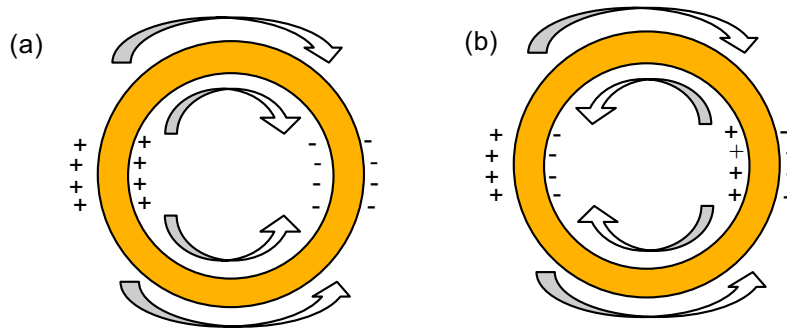


FIGURE 5.1 Sketch of the internal and external surface plasmons on a metallic shell for (a) symmetrical and (b) antisymmetrical coupling, respectively.

In this Chapter we examine simpler submicron “nano-matryoshka’s” but arranged in the 3D periodic lattice. We study the linear optical properties of a 3D photonic crystals composed of gold-shell spheres with an outer diameter of 276 nm grown on a thick silica core and covered by a thin silica outer layer. Our studies were stimulated by predictions that such a structure possesses a complete photonic band gap in the infrared. Here, however, we aim to establish the physics of the interacting resonance modes in our photonic crystal and confine ourselves to optical properties in the *visible* range where surface plasmon resonances are expected to coexist with diffraction resonances of the periodic lattice. We examine both the reflection spectra and the angular distribution of the diffracted light from the photonic crystal. In contrast to the case of a metallic film, this type of photonic crystal does not support a propagating plasmon-polariton, because the gold shells are not touching each other. Instead, light can only excite discrete surface plasmon resonances, which results in the interplay between external and internal plasmonic resonances of single particles, accounted for by Mie theory [23].

5.2 Sample and experimental details

Metallo-dielectric photonic crystal were fabricated by C. M. Graf in the Debye Institute, Department of *Soft Condensed Matter*, University of Utrecht, the Netherlands. The sample consists of close-packed metallo-dielectric particles, forming a photonic crystal. Each particle has a silica core with a radius of $r_1 = 228$ nm covered by a gold shell and capped with a silica outer shell with thicknesses of $r_2 - r_1 = 38$ nm and $r_3 - r_2 = 10$ nm, respectively, as shown in Fig. 5.2.

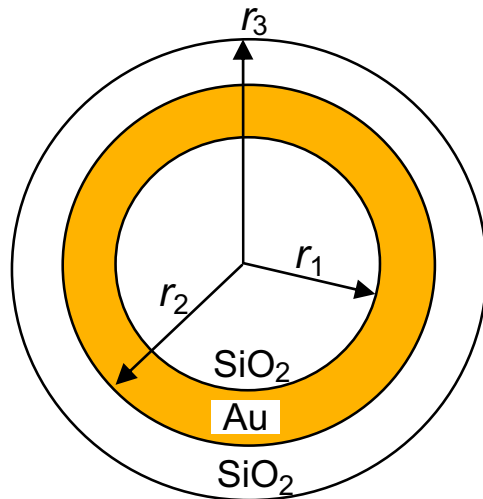


FIGURE 5.2 Silica-core gold-shell particle with silica outer shell.

The metallic-dielectric spheres were synthesized in a multistep reaction. First, spherical silica particles of 228 nm radius were grown in a stepwise seeded Stöber growth process. In the second step, gold nanoclusters of 1–2 nm in diameter were attached to the silica spheres. Subsequently, these precursor spheres were put in an $\text{HAuCl}_4/\text{K}_2\text{CO}_3$ solution. Addition of hydroxylamine to this solution results in reductive growth and coalescence of the deposited gold nanoclusters and the formation of a closed thin gold shell. Finally, capping the colloidal particles with an outer silica layer was achieved by surface functionalization with polyvinylpyrrolidone and subsequent growth by a Stöber-like process [24].

Since the silica outer shell reduces the Van-der-Waals interparticle forces, the particles can self-assemble in a periodic fashion. For this, a droplet of ethanol containing the silica coated gold-shell colloidal particles was carefully dried on a silicon wafer as to produce a close-packed array of the particles. Depending on the sample point, the thickness of the obtained photonic crystal appeared to gradually vary from one monolayer to tens of monolayers. The scanning electron microscope (SEM) picture of a highly ordered part of the sample is shown in Fig. 5.3. We assume in the following that studied points of our sample have an fcc structure. Further details of the fabrication method can be found in Ref. [19].

All experiments were carried out at room temperature. Stationary reflection spectra were obtained using a continuum white light source generated by amplified femtosecond pulses on a sapphire plate. The experimental setup was the same

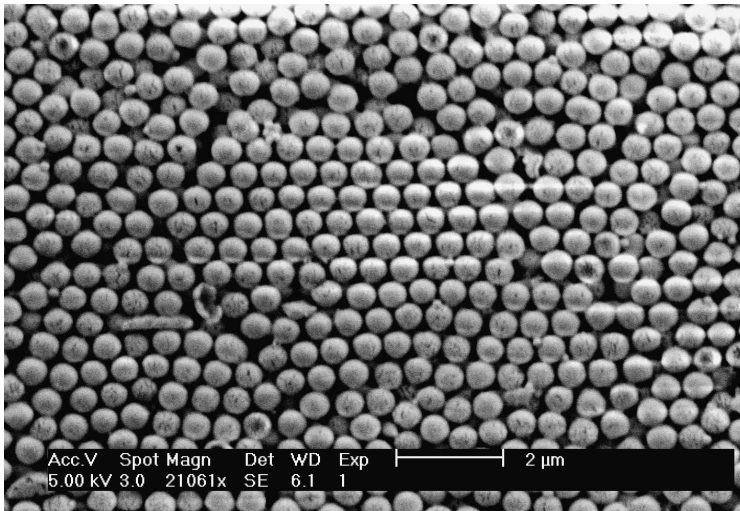


FIGURE 5.3 SEM image of the fcc gold-shell photonic crystal on a silicon substrate.

as described in Section 2.3, except that for the stationary experiments the pump pulse was not applied. The white light was directed at an angle θ to the $[1\ 1\ 1]$ direction of the photonic crystal and focused onto a $25\text{-}\mu\text{m}$ spot at the sample surface. The reflected light was picked up by a lens, passed via a spatial filter, and focused onto the entrance of an optical fiber (Fig. 2.2). This fiber transferred the reflected light to the entrance slit of a spectrometer. The spectrum was detected by a cooled charge-coupled device (CCD) controlled by a computer. In order to obtain the absolute reflectivity from the photonic crystal, we gauged our measurements against the well-known reflectivity spectra of bulk silicon by measuring the reflection of a part of the sample, that happens not to be covered by gold-shell particles. The angular distribution of the reflected and diffracted light can be displayed on a screen inserted in front of the spatial filter (see Fig. 2.2).

5.3 Experimental results

The linear optical properties of our photonic crystal turn out to depend strongly on the number of layers of the gold-shell spheres on the substrate. However, as will be shown later, there are some general features, that are found irrespective of the actual number of layers of the photonic crystal. Therefore, we describe the linear properties of a single-layer of gold-shell particles first and subsequently ex-

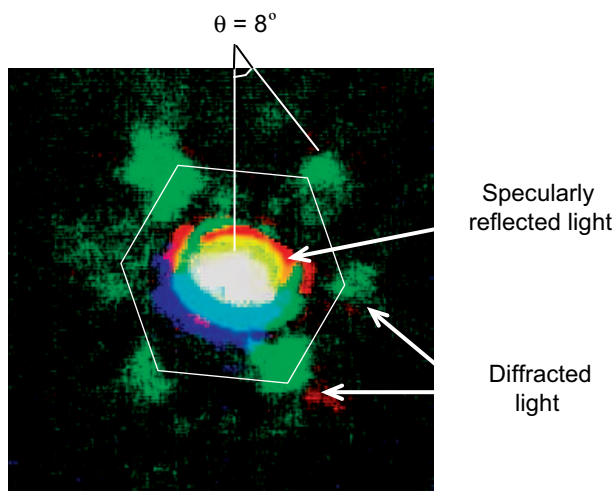


FIGURE 5.4 Diffraction pattern from one layer of ordered gold-shell particles on the silicon substrate. The angle between the propagation direction of the specularly reflected beam and the diffraction maxima is $\theta = 8^\circ$.

amine the differences that appear when more layers are present in the fcc-ordered photonic structure.

5.3.1 Reflection from a single hexagonal layer of gold-shell particles

A single layer of close-packed gold-shell particles is expected to be semitransparent for visible light. As a result, the main part of the reflected intensity should be due to specularly reflected light from the silicon substrate that manages to leak back and forth through the layer of particles. In addition to this, the reflection should have a “photonic” contribution, i.e. due to diffraction on the periodic structure of ordered gold-shells. Figure 5.4 displays the measured diffracted light intensity incident on a screen placed near the sample (the position of the screen is schematically shown on Fig. 2.2). Here, the central spot corresponds to the specularly reflected light. The specularly reflected beam propagates in a cone, which is limited by the aperture of the incident white light. The angular distribution of the diffraction pattern is strongly inhomogeneous and peaks roughly at the apexes of a hexagon. Surprisingly, the angle between the propagation direction of the specular beam and the diffracted ones amounts to only $\theta \approx 8^\circ$. This small angle cannot be explained neither in terms of single-particle scattering, nor by simple diffraction on a close-packed layer or 3Dfcc structure. The spectra of the diffracted and

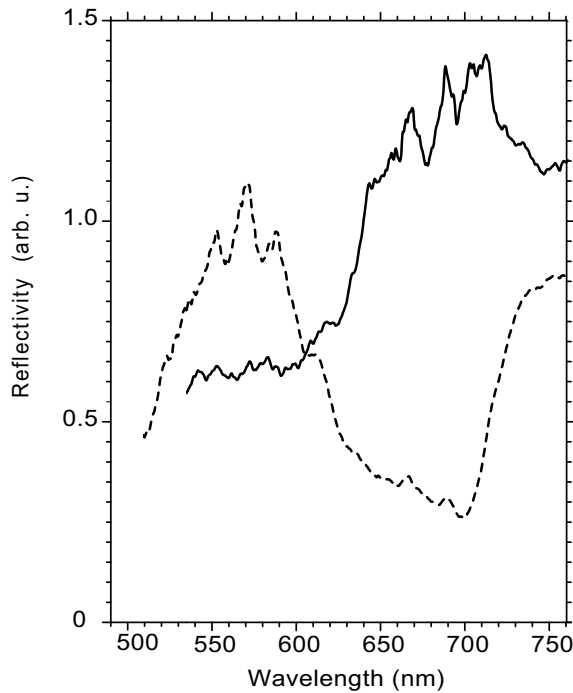


FIGURE 5.5 Linear reflection spectra of the specularly reflected (solid line) and diffracted light (dashed line), respectively, from one layer of gold-shell particles on a silicon substrate.

specular signals are shown in Fig. 5.5 by dashed and solid lines, respectively. The specular reflection peaks at 700 nm and has no spectral feature in the green range of the spectrum (550 – 600 nm). However, the spectrum of the diffracted light peaks at 570 nm and does not exhibit a maximum at 700 nm. We obtained the same spectra from the sample points where hexagonal pattern was not found and the scattered light was distributed chaotically.

5.3.2 Reflection from a multi-layer gold-shell photonic crystal

Let us now describe the optical properties of more than one layer of ordered gold-shell particles that are stacked in a hexagonal fashion, corresponding to a 3D hexagonal of fcc matrix. Unfortunately, during self-assembly, we do not have control of the stacking order in the sample introducing inherent disorder in the growth direction. In sufficiently thick regions of the crystal, the contribution from

the reflection from the substrate vanishes. Moreover, the hexagonal diffraction pattern (Fig. 5.4) disappeared completely and only one beam was observed. For the most part of the sample this beam is weak and has a broad angular distribution, which as we suppose is due to disorder. However, at some specific points at the sample reflectivity dramatically enhances and the angular distribution of the reflected beam becomes much narrower but, however, slightly wider than the incident probe beam. We believe that these specific points correspond to highly ordered parts of the sample. These specific points have the identical linear reflection spectra, such as the ones shown in Figure 5.6(a) for some selected angles of incidence. The spectra have a rather complicated structure consisting of several peaks at 500, 570, 650, and 700 nm denoted as P1, P2, P3, and P4, respectively, and several dips at 530, 615, and 680 nm, denoted as D1, D2, and D3, respectively. The exact position of the maxima and minima slightly depends on the incident angle but not on the specific location on the sample. We note that positions P2 and P4 coincide with the single-layer reflection maxima of the diffracted and specular beams, respectively [see Fig. 5.5 and 5.6(a)].

In the range of 600–750 nm, the spectral positions of the minima and maxima in the reflection spectra (Fig. 5.6) exhibit no angular dependence. However, below 550 nm and above 800 nm [not shown in Fig. 5.6(a)] the maxima and minima strongly depend on the angle of incidence.

5.4 Theory

In Chapter 3 we calculated a reflectivity spectrum around the stop band of a non-metallic photonic crystal in a framework of the two-band mixing formalism. This method takes into account only two waves interacting near the edge of the first Brillouin zone. Therefore, the validity of the two-band mixing theory is limited to the spectral range around a photonic stop band. Moreover, this method cannot be fully applicable to photonic crystals containing metals because it does not take into account plasmon modes of individual particles. Therefore, calculations of optical properties of a complicated photonic crystal as our array of dielectric-metal core-shells require more sophisticated methods.

The band structure of an *infinite* photonic crystal can be calculated by using a 3D photonic variant of the Korringa-Kohn-Rostocker (KKR) method developed by A. Moroz [8, 25, 26]. In the framework of the KKR method scattering from an isolated sphere is calculated on the basis of spherical functions taking into account a sufficient number of higher harmonics.

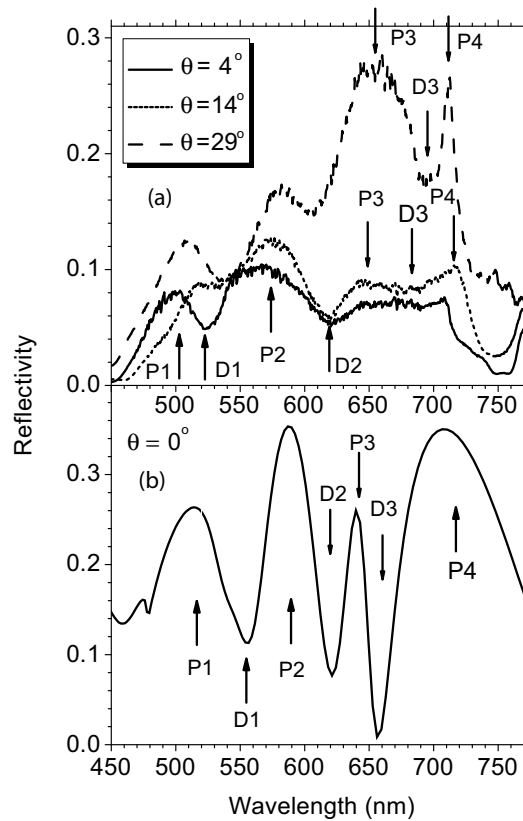


FIGURE 5.6 (a) Reflection spectra from thick (> 5 layers) gold-shell photonic crystal at various angles of incidence, θ . (b) Calculated reflection spectrum of a single close-packed hexagonal layer of gold-shell particles on an infinite silicon substrate for $r_1 = 228$ nm, $r_2 = 266$ nm, $r_3 = 276$ nm, and $\theta = 0$.

5.4.1 Layered KKR method

Transmission, reflection, and absorption of a *finite-size* photonic crystal can be calculated using the layered variant of the photonic Korringa-Kohn-Rostocker method (LKKR) [27–29]. This method has been recently used to calculate the linear reflection and transmission spectra of various photonic structures, such as ZnS-SiO₂ core-shell 3D photonic crystal and metallo-dielectric photonic glasses of colloidal silver spheres, and demonstrated to be in agreement with experimental spectra [30–32]. In the framework of the LKKR method, space is divided into

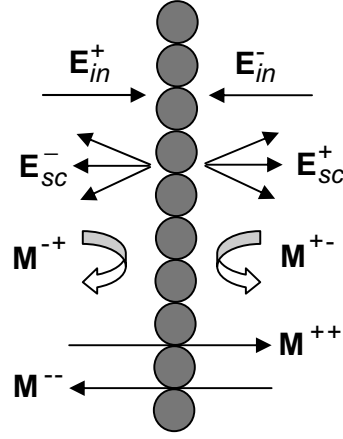


FIGURE 5.7 Scattering from a 2D plane of ordered spheres.

three parts: (i) the substrate, (ii) the photonic crystal composed of a close-packed periodic array of the multi-shells, and (iii) air. The substrate and the photonic crystal parts are considered to extend infinitely far in x and y directions. In addition to this, one assumes that the incident light propagates along the z -axis. Further, the periodic array of non-overlapping spheres is considered as a stack of the 2D layers. Each layer is infinite and periodic in the x and y directions. In order to obtain the transmission and reflectivity of the photonic crystal, one needs to find the solution of Maxwell equations in the substrate, air, and each of 2D layers of the spheres. Finally, the obtained solutions are connected by applying proper boundary conditions described in terms of transfer and transmission matrixes. We start our analysis describing the scattering by only one plane of 2D-ordered spheres.

In the following, we denote \mathbf{E}_{in}^+ and \mathbf{E}_{in}^- as the electric field of a plane wave that is incident on the layer of spheres and propagate to the right, and left, respectively, as shown in Fig. 5.7. Similarly, \mathbf{E}_{sc}^- and \mathbf{E}_{sc}^+ correspond to the scattered waves. The reflected wave can be expanded in a Fourier series,

$$\mathbf{E}_{sc}^-(\mathbf{r}) = \sum_{\mathbf{G}, j} [\mathbf{E}_{sc}]_{\mathbf{G}, j}^- \exp(i\mathbf{K}_{\mathbf{G}}^- \cdot \mathbf{r}) \hat{\mathbf{u}}_j \quad (5.1)$$

where \mathbf{G} is the reciprocal-lattice vector, $\hat{\mathbf{u}}_j$ with $j = x, y, z$ denotes the base vectors, and

$$\mathbf{K}_{\mathbf{G}}^{\pm} = \left(\mathbf{k}_{\parallel} + \mathbf{G}_{\parallel}, \pm \sqrt{\varepsilon_h \sigma^2 - (\mathbf{k}_{\parallel} + \mathbf{G}_{\parallel})^2} \right). \quad (5.2)$$

Here, $\sigma = \omega/c$ with ω frequency of the light, c speed of light in vacuum, and ε_h is the dielectric constant of the host. We note that in our particular case, spheres are in air and $\varepsilon_h = 1$. Further, the first and the second components of the right-hand part of Eq. (5.2) define the parallel and transverse components of the wavevector, respectively, and \mathbf{k}_{\parallel} is the component of the wavevector of the incident light in the 2D plane of spheres. We note, that when $\sigma^2 < (\mathbf{k}_{\parallel} + \mathbf{G}_{\parallel})$ the wavevector is imaginary and the wave is decaying.

The Fourier coefficient in Eq. (5.1) can be expressed as

$$[\mathbf{E}_{sc}]_{\mathbf{G}_j}^- = \sum_{\mathbf{G}, j'} \mathbf{M}_{\mathbf{G}_j, \mathbf{G}' j'}^+ [\mathbf{E}_{in}]_{\mathbf{G}}^+ \quad (5.3)$$

where $[\mathbf{E}_{in}]_{\mathbf{G}}^+$ is the Fourier coefficient of the incident wave and $\mathbf{M}_{\mathbf{G}_j, \mathbf{G}' j'}^+$ the reflection matrix element. The transmitted wave $\mathbf{E}_{tr}^+ = \mathbf{E}_{in}^+ + \mathbf{E}_{sc}^+$ can be expressed as

$$[\mathbf{E}_{tr}]_{\mathbf{G}_j}^+ = [\mathbf{E}_{tr}]_{\mathbf{G}_j}^+ \delta_{\mathbf{G}\mathbf{G}'} + [\mathbf{E}_{sc}]_{\mathbf{G}_j}^+ = \sum_{\mathbf{G}, j'} \mathbf{M}_{\mathbf{G}_j, \mathbf{G}' j'}^{++} [\mathbf{E}_{in}]_{\mathbf{G}_j}^+ \quad (5.4)$$

where $\mathbf{M}_{\mathbf{G}_j, \mathbf{G}' j'}^{++}$ is the transmission matrix element. Analogously, we can define the reflection matrix element $\mathbf{M}_{\mathbf{G}_j, \mathbf{G}' j'}^{+-}$ and transmission matrix element $\mathbf{M}_{\mathbf{G}_j, \mathbf{G}' j'}^{--}$ for the plane wave incident on the right side of the layer. The transmission and reflection matrices are functions of \mathbf{k}_{\parallel} , σ , the scattering properties of an individual sphere [33], and the geometrical properties of the layer of particles. The detailed description of these matrices can be found in Refs. [29, 34].

It is important to note that Eqs. (5.3) and (5.4) also correctly describe the much simpler case of reflection and transmission through a homogeneous plate of thickness d_l . In this case, the reflection and transmission matrices reduce to Fresnel's law. Generally, a photonic crystal can be treated as a stack of layers of thickness d_l , and each layer can be either a 2D periodic array of spheres or a homogeneous plate. In Fig. 5.8 we schematically sketch our sample that is composed of $N - 1$ layers of gold-shell particles and one homogeneous thick layer of silicon.

In order to obtain the reflected and transmitted waves propagating through *all* layers, we have to apply the continuity condition on the interfaces between the 2D layers. For this purpose we introduce new \mathbf{Q} -matrices that express the incoming and outgoing waves on the left and the right interfaces of the layers, respectively. For a plane of spheres the transmission and reflection matrix elements then read

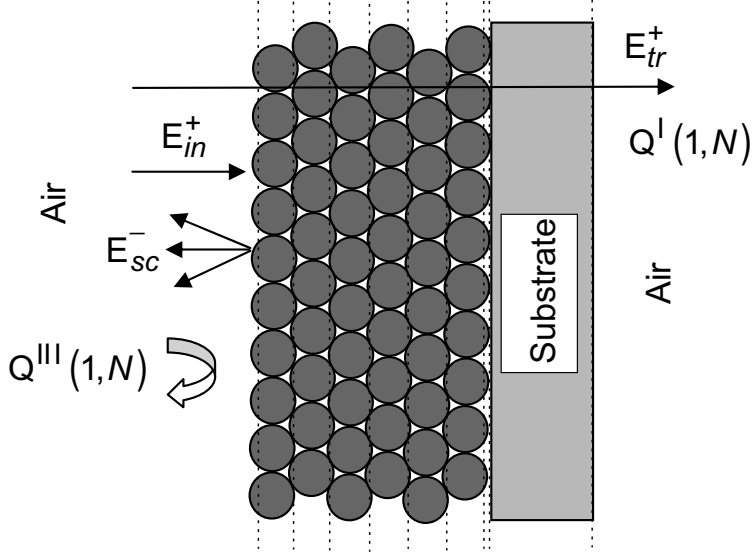


FIGURE 5.8 Reflection and transmission through the gold-shell photonic crystal on a silicon substrate. Vertical dotted lines show the interfaces between the 2D layers.

$$\begin{aligned}
 Q_{\mathbf{G}_j, \mathbf{G}'_j}^{\text{I}} &= \mathbf{M}_{\mathbf{G}_j, \mathbf{G}'_j}^{++} \exp(i\mathbf{K}_{\mathbf{G}}^+ \cdot \mathbf{d}), \\
 Q_{\mathbf{G}_j, \mathbf{G}'_j}^{\text{II}} &= \mathbf{M}_{\mathbf{G}_j, \mathbf{G}'_j}^{+-} \exp\left[\frac{1}{2}i(\mathbf{K}_{\mathbf{G}}^+ - \mathbf{K}_{\mathbf{G}}^-) \cdot \mathbf{d}\right], \\
 Q_{\mathbf{G}_j, \mathbf{G}'_j}^{\text{III}} &= \mathbf{M}_{\mathbf{G}_j, \mathbf{G}'_j}^{-+} \exp\left[\frac{1}{2}i(\mathbf{K}_{\mathbf{G}}^+ - \mathbf{K}_{\mathbf{G}}^-) \cdot \mathbf{d}\right], \\
 Q_{\mathbf{G}_j, \mathbf{G}'_j}^{\text{IV}} &= \mathbf{M}_{\mathbf{G}_j, \mathbf{G}'_j}^{--} \exp(-i\mathbf{K}_{\mathbf{G}}^- \cdot \mathbf{d}).
 \end{aligned} \tag{5.5}$$

Here, \mathbf{d} is a vector perpendicular to the plane interfaces with $\mathbf{d} = d_l$. For the case of a homogeneous plate the Q-matrices become

$$\begin{aligned}
 Q_{\mathbf{G}_j, \mathbf{G}'_j}^{\text{I}} &= \mathbf{N}_{\mathbf{G}_j, \mathbf{G}'_j}^{++} \exp\left[i\frac{1}{2}(\mathbf{K}_{3\mathbf{G}}^+ + \mathbf{K}_{1\mathbf{G}}^+) \cdot \mathbf{d}\right], \\
 Q_{\mathbf{G}_j, \mathbf{G}'_j}^{\text{II}} &= \mathbf{N}_{\mathbf{G}_j, \mathbf{G}'_j}^{+-} \exp\left[i\frac{1}{2}(\mathbf{K}_{3\mathbf{G}}^+ - \mathbf{K}_{3\mathbf{G}}^-) \cdot \mathbf{d}\right], \\
 Q_{\mathbf{G}_j, \mathbf{G}'_j}^{\text{III}} &= \mathbf{N}_{\mathbf{G}_j, \mathbf{G}'_j}^{-+} \exp\left[i\frac{1}{2}(\mathbf{K}_{1\mathbf{G}}^+ - \mathbf{K}_{1\mathbf{G}}^-) \cdot \mathbf{d}\right], \\
 Q_{\mathbf{G}_j, \mathbf{G}'_j}^{\text{IV}} &= \mathbf{N}_{\mathbf{G}_j, \mathbf{G}'_j}^{--} \exp\left[-i\frac{1}{2}(\mathbf{K}_{3\mathbf{G}}^- + \mathbf{K}_{1\mathbf{G}}^-) \cdot \mathbf{d}\right],
 \end{aligned} \tag{5.6}$$

with

$$\mathbf{K}_{m, \mathbf{g}}^{\pm} = \left(\mathbf{k}_{\parallel} + \mathbf{G}_{\parallel}, \pm \sqrt{\varepsilon_m \sigma^2 - (\mathbf{k}_{\parallel} + \mathbf{G}_{\parallel})^2} \right). \tag{5.7}$$

Here, ε_1 and ε_3 are the host dielectric constants of the preceding and successive layers, respectively, and $\mathbf{N}_{\mathbf{G}_j, \mathbf{G}'_j}^{\pm\pm}$ the reflection and transmission matrix elements for a homogeneous plate. The exact form of this matrix can be found in Ref. [29].

Finally, the $\mathbf{Q}(n, n+1)$ -matrix of a combination of two successive layers, n and $n+1$, can be obtained according to the following rule,

$$\begin{aligned}
\mathbf{Q}^{\text{I}}(n, n+1) &= \mathbf{Q}^{\text{I}}(n+1) [\mathbf{I} - \mathbf{Q}^{\text{I}}(n) \mathbf{Q}^{\text{III}}(n+1)]^{-1} \mathbf{Q}^{\text{I}}(n), \\
\mathbf{Q}^{\text{II}}(n, n+1) &= \mathbf{Q}^{\text{II}}(n+1) + \mathbf{Q}^{\text{I}}(n+1) \mathbf{Q}^{\text{II}}(n) \\
&\quad \times [\mathbf{I} - \mathbf{Q}^{\text{III}}(n+1) \mathbf{Q}^{\text{II}}(n)]^{-1} \mathbf{Q}^{\text{IV}}(n+1), \\
\mathbf{Q}^{\text{III}}(n, n+1) &= \mathbf{Q}^{\text{III}}(n) + \mathbf{Q}^{\text{IV}}(n) \mathbf{Q}^{\text{III}}(n+1) \\
&\quad \times [\mathbf{I} - \mathbf{Q}^{\text{II}}(n) \mathbf{Q}^{\text{III}}(n+1)]^{-1} \mathbf{Q}^{\text{I}}(n), \\
\mathbf{Q}^{\text{IV}}(n, n+1) &= \mathbf{Q}^{\text{IV}}(n) [\mathbf{I} - \mathbf{Q}^{\text{III}}(n+1) \mathbf{Q}^{\text{II}}(n)]^{-1} \mathbf{Q}^{\text{IV}}(n+1).
\end{aligned} \tag{5.8}$$

Applying this rule recursively for each contributing layer we obtain $\mathbf{Q}^{\text{I}}(1, N)$ and $\mathbf{Q}^{\text{III}}(1, N)$, which determine the total transmission and reflection of the studied structure (Fig. 5.8), respectively. We note, that this method of calculation can also account for stacking failure by inserting a random lateral shift between two successive layers. However, in this chapter we limit ourselves for calculating only perfectly ordered structures.

5.4.2 Computation results

In this Section we present the results of the of the *ab initio* calculation of the reflectivity spectrum of our sample relying on the LKKR method using a computer code composed by A. Moroz [26] (see also <http://www.wave-scattering.com>).

For the calculation we inserted the refractive index of silica $n(\text{SiO}_2) = 1.45$, the wavelength-dependent dielectric constant of gold [35] depicted in Fig. 5.9, and the geometrical parameters of the silica-gold multishell spheres known from the SEM measurements, $r_1 = 228$ nm, $r_2 = 266$ nm, and $r_3 = 276$ nm. We stress that our calculation allows for no fitting parameters.

Figure 5.6(b) shows the calculated reflection spectrum of a single layer of close-packed gold-shell particles on an infinite silicon substrate at $\theta = 0$ angle of incidence. The spectrum already reasonably resembles the experimentally observed one [Fig. 5.6(a), solid line]. This is remarkable because the calculation

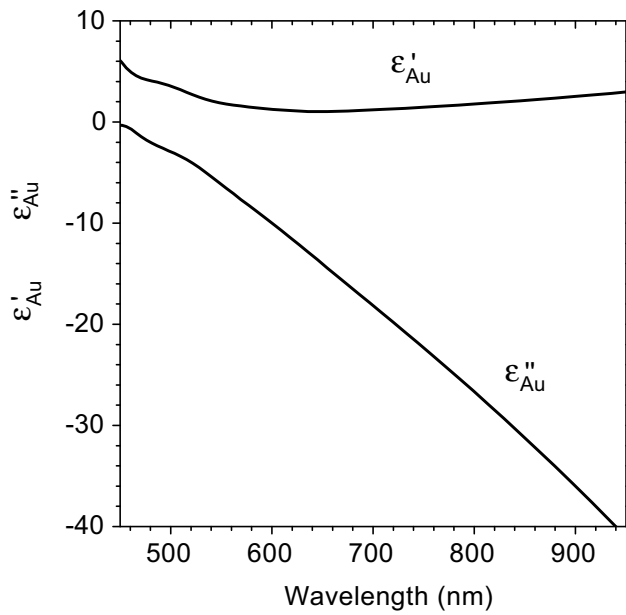


FIGURE 5.9 Dispersion of the real, ϵ'_{Au} , and the imaginary ϵ''_{Au} , parts of the dielectric constant of gold.

refers to the case of only one single layer, while the measurements are taken on a multi-layer structure. The maxima P1, P2, P3, and P4 and minima D1, D2, and D3 of the measured spectrum are nicely reproduced in the calculation. The spectral positions of the dips at 550 nm (D1) and 660 nm (D3) in the calculated spectrum coincide, respectively, with the calculated dipole and the quadrupole resonances of individual gold shell particles that are shown in Fig. 5.10. In that figure, the solid and dotted lines correspond to the scattering and absorption efficiency of an individual particle.

In Fig. 5.11, the dotted line shows the result of a calculation of the reflectivity from a thick photonic crystal. For comparison, the solid line displays the experimental data reproduced from Fig. 5.6(a). The calculation was performed for the (1 1 1) oriented structure composed of 12 close-packed fcc layers (i.e. perfect stacking order) on an infinite silicon substrate. We note that already 6 layers are sufficient in order to approximate the infinite photonic crystal. Unfortunately, the calculated reflectivity from the multilayered photonic crystal does not satisfactorily track the experimental curves at least with the parameter values used [Fig. 5.11(b)].

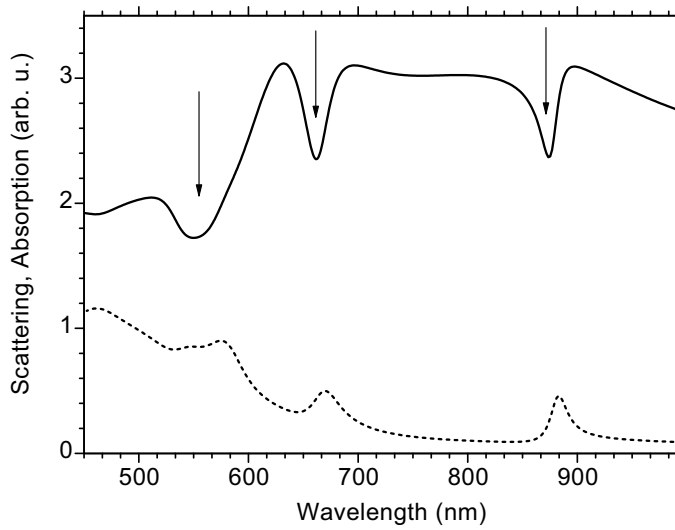


FIGURE 5.10 Calculated scattering (solid line) and absorption (dotted line) efficiencies of a single gold-shell particle for $r_1 = 228$ nm, $r_2 = 266$ nm, $r_3 = 276$ nm. The arrows at 540 nm and 870 nm show the positions of the dipole and at 660 nm quadrupole resonances.

In order to examine possible effects of non-monodispersity of our spheres, we have performed a set of computations for up to 10%-variation for the geometrical parameters of r_1 , r_2 , and r_3 over initial values. One favorable example of a calculated spectrum is presented in Fig. 5.12 and compared with experiment. These computations show that the spectral position of D2 strongly depends on r_1 but is independent of r_3 . Further, the position of peak P1 does depend on r_3 but not on r_1 , while P2, P3, and P4 depend both on r_1 and r_3 . Finally, the spectral positions of P1, P2, P3, P4, and D2 appear to be essentially independent of r_2 .

5.5 Discussion

The optical properties of gold-shell photonic crystal are governed by two types of resonances: the surface plasmons of the gold shell (Mie resonances) and the resonant scattering off the periodic array of particles (Bragg scattering). The individual contributions of these resonances can be separated by examining the angular dependence of the reflection. In case when a resonance is associated with a plasmon resonance of an isolated particle with spherical symmetry, the spec-

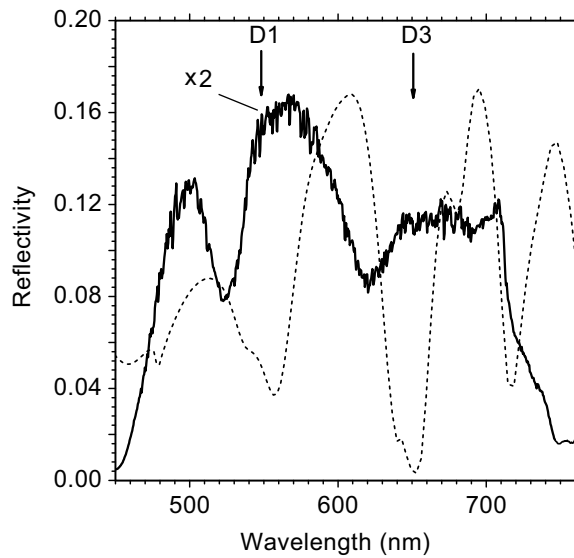


FIGURE 5.11 Calculated reflection spectrum (dotted line) along the (1 1 1) crystallographic axis of a photonic crystal composed of 12 fcc-ordered layers of the gold-shell particles on an infinite silicon substrate for $r_1 = 228$ nm, $r_2 = 266$ nm, $r_3 = 276$ nm, and $\theta = 0$. The calculation compared with the experimental reflection (solid line) at $\theta = 4^\circ$ taken from Fig. 5.6(a).

tral position of the resonance should be angle independent. In case when the resonance is associated with the ordering of the particles, however, no angular dependence is expected of the reflection spectrum. The observed maxima (P1-P4) and minima (D1-D3) in reflection [Fig. 5.6(a)] spectrum can be classified into two groups: The first group, P1, D1, and P2, has maxima and minima that depend on the angle of incidence. Therefore, their properties must be associated with a scattering on the periodic lattice that may, however, couple with the plasmon modes. The second group, D2, D3, P3, and P4, has no angular dependence and, therefore, can be attributed to the pure plasmon modes. We found that the minimum D3 in the reflection spectrum coincides with the absorption maximum of a single particle associated with the quadrupole plasmon resonance. Therefore, we believe that in the spectral range of 600 – 750 nm the spectral features of the photonic crystal are governed by the plasmon modes excited in the particles. Very recently, Miclea and co-authors reported similar effects in the reflectivity spectra in 3D photonic crystal composed of 640 nm latex spheres coated by 6-nm gold shells but detected no angular dependence of the spectral resonances in the visible spectral range. At

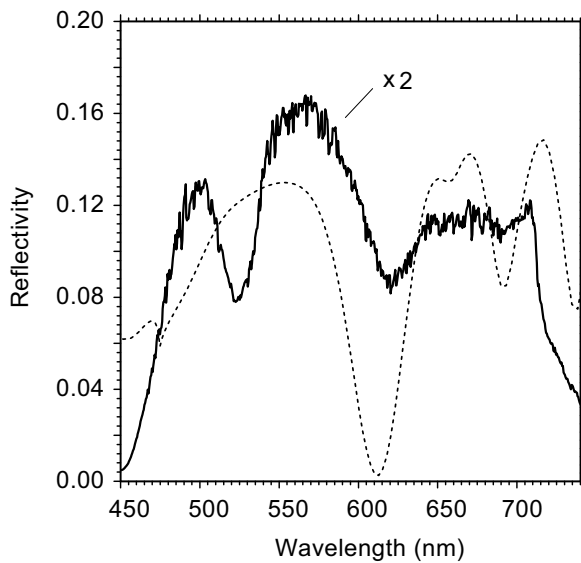


FIGURE 5.12 Calculated reflection spectrum (dotted line) along the (1 1 1) crystallographic axis of a photonic crystal composed of 12 fcc-ordered layers of the gold-shell particles on an infinite silicon substrate for $r_1 = 202$ nm, $r_2 = 264$ nm, $r_3 = 274$ nm, and $\theta = 0$. The calculation compared with the experimental reflection (solid line) at $\theta = 4^\circ$ taken from Fig. 5.6(a).

the same time, they revealed a strong angular dependence of the spectral maxima in the near-infrared and attribute this phenomenon to the Bragg diffraction on a periodic lattice [36]. Their observation was obtained independently of our first studies on metallo-dielectric structures [37]. Another related observation has been made in an inverted gold opal with 350-nm spherical cavities by Coyle *et al.* [38]. The cavities of this opal support localized surface plasmons that appear as sharp features of the reflection spectra in the visible range. Again, the spectral positions of these features are independent of the angle of incidence. All these observations support our conclusion that in the range of 600 – 750 nm the reflection of our sample is fully controlled by surface plasmon resonances.

On the other hand the dip D1 in the experimental spectra [Fig. 5.6(a)] is close to the calculated plasmon dipole resonance (Fig. 5.10) that appeared to have an angular dependence. Therefore, we can attribute D1 as a result of coupling between a plasmon resonance of an individual sphere and the scattering on a periodic crystal lattice.

This classification is also supported by the sensitivity of the calculated reflection intensity to a variation of the particle sizes r_1 , r_2 , and r_3 . Thus, the spectral position of D2 depends on r_1 , and does not depend on r_3 , which is half the lattice parameter. Since D2 is also independent of r_2 we suppose that D2 may be attributed to the internal plasmon resonance in the gold shell cavity. In contrast, P1 depends strongly on r_3 but not on r_1 . Therefore, we may safely conclude that P1 is governed by the lattice ordering.

At this point we discuss the poor agreement between the experimental and the calculated reflection spectra of the thick photonic crystal [Fig. 5.11]. The calculated spectrum (dotted line) is shifted compared to the measured one (solid line) by about 30 nm. The reason of this discrepancy is unknown and we found that it cannot be accounted for by assuming deviations of either gold or silica dielectric constants from the bulk ones. We also checked that this deviation cannot be traced back to enhanced absorption in the gold due to electron scattering on the imperfections. However, we note that the calculated spectra can be brought quite close to the experimental ones if we simply assume smaller internal radii of an individual particles. The result of a calculation for the photonic crystal composed of 12 fcc-ordered layers of the gold-shell particles on an infinite silicon substrate with inserted $r_1 = 202$ nm, $r_2 = 264$ nm, $r_3 = 274$ nm, and $\theta = 0$ is shown in Fig. 5.12.

Finally, we note that the position of the dipole resonance at 545 nm is very close to the lattice parameter $2r_3 = 552$ nm, which may result in a strong interference and possibly lead to some interesting phenomena. In Figure 5.4 we discovered that the propagation direction of light with a wavelength ~ 570 nm, diffracted on a single layer of ordered gold-shell particles, deviates from the specularly reflected light by $\theta = 8^\circ$ and produces a hexagonal diffraction pattern. Although, the origin of this phenomena is not fully understood we speculate that interference of the localized plasmon and surface modes takes place. Effects reminiscent of ours, were discussed recently by Martín-Moreno and co-authors [16] in their theory explaining highly directional beaming of light propagating through a hole in a corrugated metallic film [17]. They explain this phenomenon by formation of electromagnetic surface resonances as a result of coupling between single groove cavity modes and the periodic corrugation at the rear surface of the film. Another, perhaps related phenomenon, was discussed by Félidj and co-workers [39] in an attempt to explain the extinction spectra of gold oblate spheroidal particles deposited on 20-nm gold film on a glass substrate. They found that an ordered array of gold nanoparticles on the gold film with interparticle spacing smaller than 250 nm possesses extinction spectra with an additional band in the green

part of the spectra, which was not observed for similar particles but deposited on indium tin oxide substrate. This result was interpreted by the authors as a result of coupling between a localized surface plasmon of an individual particle and a propagating plasmon at the glass-gold interface. However, in our sample all plasmon modes are localized and excitation of the propagating surface modes on a photonic-crystal-air interface is not obvious. In this connection it may be relevant to note that these intricate effects are not restricted to metallo-dielectric structures. For example, Kramper and co-workers recently demonstrated a highly directional emission from a subwavelength waveguide in a dielectric photonic crystal [18].

However, the nature of the surface modes in our experiment remains ambiguous. Alternatively, our observation may be related to interference of the localized plasmon modes with waveguide modes of the underlying silicon substrate. A similar explanation was recently proposed by Yannopapas and Stefanou [40] in order to explain the transmission spectra of rectangular two-dimensional arrays of gold particles on an indium-tin-oxide substrate [41].

5.6 Conclusions

In this Chapter we examined reflection spectra of an fcc-ordered three-dimensional crystal composed of silica-gold core-shell colloidal particles. The observed linear spectra in the visible show several maxima that can be traced down to stop-bands. However, most linear optical properties of our gold-shell photonic crystals appeared to be governed by surface plasmon resonances of an individual gold-shell particle. We conclude that in the range of 600–750 nm the reflection properties of our sample are fully controlled by surface plasmon resonances, while in the ranges below 550 nm and above 800 nm the reflectivity is affected by resonant scattering off the photonic crystal lattice. The reflection spectra are in agreement with calculations made for a single layer of the gold-shell spheres but, unfortunately have bad agreement with calculated spectra made for an ordered multilayered photonic crystal with the correct particle dimensions. In addition, we found that a single layer of gold-shell particles may produce a surprising, highly-directional hexagonal diffraction pattern. We speculate that the observed phenomenon relates to interference of the localized surface plasmon modes and surface modes.

References

- [1] V. P. Bykov, *Sov. Phys. JETP* **35**, 269 (1972).
- [2] E. Yablonovitch, *Phys. Rev. Lett.* **58**, 2059 (1987).

-
- [3] H. S. Sözüer, J. W. Haus, and R. Inguva, *Phys. Rev. B* **45**, 13962 (1992).
- [4] R. Biswas, M. M. Sigalas, G. Subramania, and K.-M. Ho, *Phys. Rev. B* **57**, 3701 (1998).
- [5] E. Yablonovitch and T. J. Gmitter, *Phys. Rev. Lett.* **63**, 1950 (1989).
- [6] E. Yablonovitch, T. J. Gmitter, and K. M. Leung, *Phys. Rev. Lett.* **67**, 2295 (1991).
- [7] A. Blanco, E. Chomski, S. Grabtchak, M. Ibisate, S. John, S. W. Leonard, C. Lopez, F. Meseguer, H. Miguez, J. P. Mondia, et al., *Nature (London)* **405**, 437 (2000).
- [8] A. Moroz, *Phys. Rev. Lett.* **83**, 5274 (1999).
- [9] H. Raether, *Surface Plasmons on Smooth and Rough Surfaces and on Gratings* (Springer-Verlag, Berlin, 1988).
- [10] R. W. Wood, *Philos. Mag.* **4**, 396 (1902).
- [11] A. Hessel and A. A. Oliner, *Appl. Opt.* **4**, 1275 (1965).
- [12] L. Rayleigh, *Proc. Roy. Soc. (London)* **A79**, 399 (1907).
- [13] U. Fano, *Phys. Rev.* **50**, 573 (1936).
- [14] U. Fano, *J. Opt. Soc. Am.* **31**, 213 (1941).
- [15] T. W. Ebbesen, H. J. Lezec, H. F. Ghaemi, T. Thio, and P. A. Wolff, *Nature (London)* **391**, 667 (1998).
- [16] L. Martín-Moreno, F. J. Garcia-Vidal, H. J. Lezec, A. Degiron, and T. Ebbesen, *Phys. Rev. Lett.* **90**, 167401 (2003).
- [17] H. J. Lezec, A. Degiron, E. Devaux, R. A. Linke, L. Martín-Moreno, F. J. Garcia-Vidal, and T. W. Ebbesen, *Science* **297**, 820 (2002).
- [18] P. Kramper, M. Agio, C. M. Soukoulis, A. Birner, F. Muller, R. B. Wehrspohn, U. Gösele, and V. Sandoghdar, *Phys. Rev. Lett.* **92**, 113903 (2004).
- [19] C. Graf and A. van Blaaderen, *Langmuir* **18**, 524 (2002).
- [20] A. Liebsch, *Phys. Rev. B* **36**, 7378 (1987).
- [21] U. Kreibig and M. Vollmer, *Optical properties of metall clusters* (Springer-Verlag, Berlin, 1995).
- [22] E. Prodan, C. Radloff, N. J. Halas, and P. Nordlander, *Science* **302**, 419 (2003).
- [23] G. Mie, *Ann. Phys.* **25**, 377 (1908).
- [24] C. Graf, D. L. J. Vossen, A. Imhof, and A. van Blaaderen, *Langmuir* **19**, 6693 (2003).
- [25] A. Moroz, *Phys. Rev. B* **51**, 2068 (1995).
- [26] A. Moroz, *Phys. Rev. B* **66**, 115109 (2002).
- [27] E. G. McRae, *Surf. Sci.* **11**, 479 (1968).
- [28] A. Modinos, *Physica A* **141**, 575 (1987).
- [29] N. Stefanou, V. Yannopoulos, and A. Modinos, *Comp. Phys. Commun.* **113**, 49 (1998).
- [30] K. P. Velikov, A. Moroz, and A. van Blaaderen, *Appl. Phys. Lett.* **80**, 49 (2002).
- [31] K. P. Velikov, W. L. Vos, A. Moroz, and A. van Blaaderen, *Phys. Rev. B* **69**, 075108 (2004).
- [32] K. P. Velikov, Ph.D. thesis, Universiteit Utrecht (2002).
- [33] J. Sinzig and M. Quinten, *Appl. Phys. A* **58**, 157 (1994).
- [34] N. Stefanou, V. Karathanos, and A. Modinos, *J. Phys.: Condens. Matter* **4**, 7389

- (1992).
- [35] *Optical properties of metals*, vol. 2 (Fachinformationszentrum Energie, 1981).
 - [36] P. T. Miclea, A. S. Sussha, Z. Liang, F. Caruso, C. M. Sotomayor-Torres, and S. G. Romanov, *Appl. Phys. Lett.* **84**, 3960 (2004).
 - [37] D. A. Mazurenko, A. Moroz, C. M. Graf, A. van Blaaderen, and J. I. Dijkhuis, in *Photonic Crystal Materials and Nanostructures*, edited by R. M. de la Rue, P. Viktorovitch, C. M. Sotomayor-Torres, and M. Midrio (2004), vol. 5450 of *Proc. SPIE*, p. 569.
 - [38] S. Coyle, M. C. Netti, J. J. Baumberg, M. A. Ghanem, P. R. Birkin, P. N. Bartlett, and D. M. Whittaker, *Phys. Rev. Lett.* **87**, 176801 (2001).
 - [39] N. Féridj, J. Aubard, G. Lévi, J. R. Krenn, G. Schider, A. Leitner, and F. R. Aussenegg, *Phys. Rev. B* **66**, 245407 (2002).
 - [40] V. Yannopapas and N. Stefanou, *Phys. Rev. B* **69**, 012408 (2004).
 - [41] S. Linden, Kuhl, and H. Giessen, *Phys. Rev. Lett.* **86**, 4688 (2001).

CHAPTER 6

ULTRAFAST DYNAMICS IN A SILICA-GOLD CORE-SHELL PHOTONIC CRYSTAL

Abstract

We analyze the non-linear optical properties of a three-dimensional photonic crystal composed of close-packed $\text{SiO}_2/\text{Au}/\text{SiO}_2$ core-shell colloidal particles. The transient reflection spectra of the photonic crystal following excitation by intense femtosecond optical pulses demonstrate subpicosecond dynamics associated with rapid heating of the electron gas. Photoinduced absorption results in a broadening of the plasmon resonances and modifies the reflection spectrum. Depending on the wavelength, we observed both transient bleaching and transient absorption. The observed dynamics is interpreted in terms of the temperature dependence of the dielectric constant of gold and analyzed in the framework of the “two-temperature model”.

6.1 Introduction

Dielectric spheres coated with metallic shells hold a great promise for non-linear optics [1–3] and ultrafast photodetection [4, 5]. There is an obvious reason to expect enhanced non-linear properties in such kind of particles: metallic sphere possesses surface plasmon resonances that may enhance the local electric field. It was proposed that intense optical excitation may shift the spectral position of the plasmon resonance and, under some circumstances even lead to optical bistability [3, 6]. Subpicosecond non-linear responses from metallic nanoshells were demonstrated for the first time by Averitt and co-workers [7] for particles composed of a ~ 40 -nm Au_2S core surrounded by an ultrathin Au layer. The dynamical response of these particles following femtosecond optical excitation, however, turned out to be similar to the response of solid metal particles, which were already extensively studied during the previous decade [8–14]. Quite importantly, the spectral posi-

tion of the plasmon resonance in metallic nanoshells depends on the core-shell ratio that makes their optical properties tunable by choosing appropriate geometrical parameters [1, 15, 16]. It was established that the ultrafast signal induced by femtosecond optical excitation is caused by rapid heating of the electron gas in the metal. Electron heating, in turn, changes both the real and the imaginary part of the dielectric constant of a metal and appears to account for the observed wavelength-dependent transient changes in the absorption spectra. It is important to note that non-linear properties can be dramatically enhanced in an ensemble of metallic particles. For example, strong enhancement of second harmonic generation was recently reported in randomly distributed arrays of gold nanoparticles [17].

Nowadays, progress in nanotechnology allows us to fabricate periodic arrays of metallic nanoshells [18, 19] forming a photonic crystal. These structures are very promising for ultrafast switching of light. On one hand, it was predicted that these structures may possess a sizable photonic bandgap in the visible or infrared spectral range [20, 21]. On the other hand, in such structures light can be localized in extremely small volumes boosting their non-linear optical properties.

In Chapter 5, we analyzed the linear properties of a 3D photonic crystal composed of a silica core surrounded by a gold shell and capped by an outer silica nanoshell. In the visible spectral range we observed that the optical properties of this photonic crystal are governed by plasmon resonances. In this Chapter we examine the ultrafast nonlinear response of the photonic crystal, and analyze both the spectral response and subpicosecond dynamics of the transient reflectivity followed by femtosecond optical excitation.

6.2 Experimental details

6.2.1 Time-resolved detection of the reflectivity spectra

Our sample is a three-dimensional photonic crystal with submicron core-multi-shell spheres on the lattice points. Each particle consists of a 228-nm radius silica core, gold shell with a thickness of 38-nm, and an outer silica shell with a thickness of 10-nm. A more detailed description of our sample and its linear optical properties can be found in Chapter 5.

The ultrafast response of our photonic crystal was examined by the low-repetition-rate pump-probe setup described in Section 2.3. The angle of incidence of the probe beam was chosen to be $\theta = 14^\circ$. The transient changes of the reflectivity were measured from the thick, highly ordered part of the photonic crystal

containing more than five layers of gold-shell particles. The studied sample areas were carefully selected by checking that the linear reflection spectrum coincides with the spectrum depicted in Fig. 5.6. In thick samples, the reflected light is concentrated in the specular direction and the scattering at other angles vanishes. In order to reject the residual scattering of the pump light in these transient reflectivity experiments, the reflected probe beam was passed through a spatial filter that admits exclusively the specular beam. The intensity of the pump beam was chosen to be $\sim 0.5 \text{ mJ/cm}^2$, which is slightly below the damage threshold. Despite these high illumination, both the linear reflection spectra and the dynamics of the transient reflectivity spectra appeared to remain stable and reproducible for at least several hours.

6.2.2 High-selectivity pump-probe detection at a specific wavelength

Some high-sensitivity pump-probe measurements at a specific wavelength were performed employing another detection technique developed by E. Hesseling and O. L. Muskens [22]. In this configuration the pump pulse was modulated by a mechanical chopper operating at a frequency $\nu_m = \nu/4$, where $\nu = 1 \text{ kHz}$ is the repetition frequency of our Ti-sapphire laser. The phase of the chopper was synchronized with the Ti-sapphire laser. The reflected probe beam from the sample was collected, guided by a lens into the fiber, and transported to the entrance slit of the spectrometer. The intensity of the light at a wavelength selected by the end slit was detected by a slow InGaAs photodetector with amplifier, yielding a sufficient optical sensitivity in a large spectral range, 400 – 2000 nm. In order to enhance the signal-to-noise ratio of the photodetector, we decided to increase the intensity of the incoming light on the entrance of the photodetector by opening the output slit of the spectrometer at the expense of decreasing the spectral resolution to 35 nm. Since the detected probe light was chirped, the temporal resolution of the detection is reduced to about 1 ps. The electronic signal from the photodetector was analyzed by a digital multimeter (HEWLETT PACKARD 3458A) with a 300-k Ω load resistor at the input. The digital multimeter was synchronized with the pump pulses by an external trigger and a digital delay generator. Both the multimeter and the digital delay generator were controlled by a computer. In order to increase the signal-to-noise ratio further, the multimeter was set to measure the average voltage of the photodetector with a precision of 5 digits in a 100- μs time window during the electrical signal of the probe pulse. For each measurement the multimeter registered one pulse of the reflected probe beam *with* the pump excitation and one *without*. The difference between these two measurements is subsequently stored in the memory of the multimeter. The collected values were

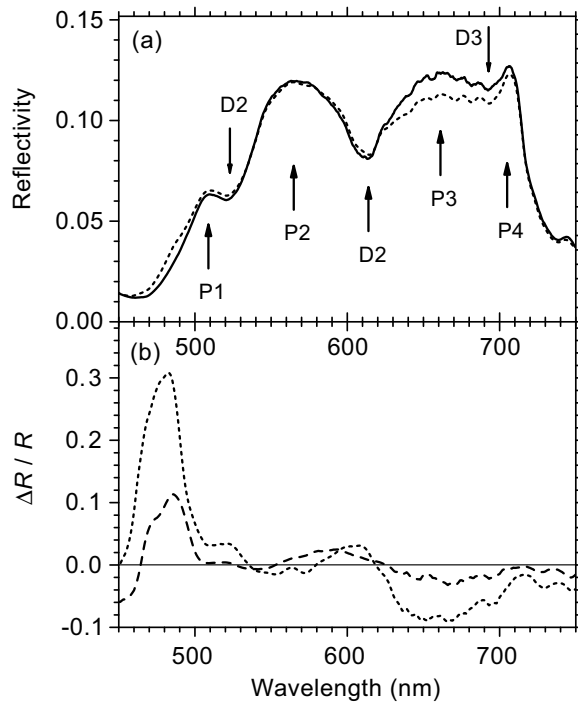


FIGURE 6.1 (a) Reflection spectra before (solid line) and 500 fs after (dotted line) 800-nm optical excitation pulse for $\sim 0.5\text{-mJ/cm}^2$ pump power density; (b) differential changes in the reflectivity at a delay of 500 fs (dotted line) and 17 ps (dashed line).

averaged over 4000 measurements for each position of the delay line and the result was transferred to the computer. The final signal-to-noise ratio of the detected $\Delta R/R$ was about 10^3 . Further details of this technique can be found in Ref. [22].

All experiments have been carried out at room temperature.

6.3 Ultrafast response of the gold-shell photonic crystal

Figure 6.1(a) shows time-resolved reflection spectra of the gold-shell photonic crystal taken before (solid line) and 0.5 ps after (dotted line) the 120-fs optical excitation for a surface density of 800-nm pump pulse of about 0.5-mJ/cm^2 per pulse. The reflection spectrum measured at a negative delay (solid line) was found to coincide with the stationary reflection spectrum measured in the absence of the pump pulse. This fact ensures that cooling of the excited sample volume

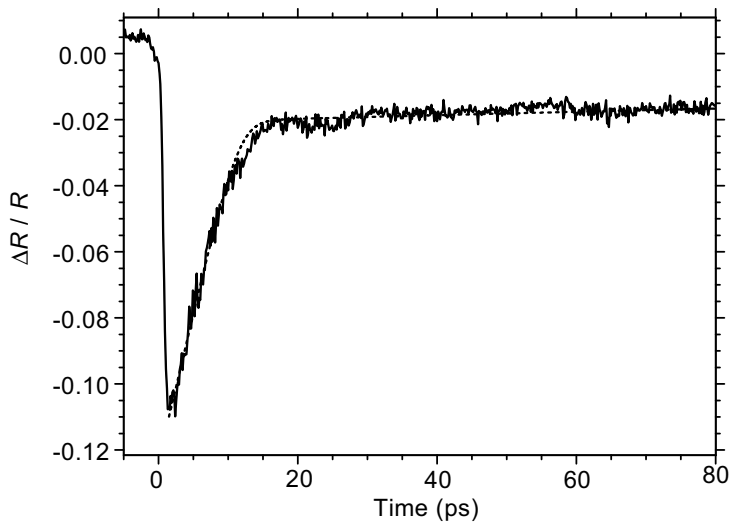


FIGURE 6.2 Temporal evolution of the transient reflectivity at 670 nm. The red dotted line is a fit by the two-temperature model.

occurs well within the time interval between two consecutive pump pulses. The reflection spectrum measured at 0.5-ps delay of the pump excitation (dotted line) demonstrates pronounced changes in the reflectivity intensity in the range 630 – 700 nm. In order to show this to a better advantage, we also plotted in Fig. 6.1(b) the differential changes of the reflectivity, $\Delta R/R$, and dashed lines for 500 fs and 17 ps delays, respectively. We note, that the error in the measured values is smaller than 1%.

For the first 100 ps following the optical excitation, the temporal evolution of the transient reflectivity was found to exhibit the same shape over the full visible spectral range but different amplitudes. A typical time dependence of $\Delta R/R$ measured at 670-nm is shown on Fig. 6.2 by the solid line. In this graph the duration of the initial rise ~ 1 ps is limited by the temporal resolution of the setup. Accurate measurements using the chirp-correction technique (Section 2.3) allowed us to determine this rise time to be ~ 300 fs.

6.4 Nature of the ultrafast changes in reflectivity

Reflection spectra of the photonic crystal [Fig. 6.1(a)] change substantially upon optical excitation. Around 550 nm and 680 nm, the differential reflectivity is nega-

tive while at 610 nm it increases abruptly and even becomes positive [Fig. 6.1(b)]. Since silica is transparent for 800-nm light, the core will not absorb and the pump pulse can only affect the optical parameters of the gold shell. We can also exclude influences from the thermal expansion because the subpicosecond time scale is too short to develop perceptible mechanical movements. Therefore, we explain the ultrafast change in the reflectivity by a transient modification of the dielectric constant of the gold shell, $\varepsilon = \varepsilon' + i\varepsilon''$, due to a rapid heating of the electron gas. In the following we discuss on the cooling mechanisms of the gold nanoshells [7, 23].

Several studies of the dynamic optical response of solid and hollow gold nanospheres revealed that optical excitation tends to suppress the surface plasmon resonances on the subpicosecond timescale [7, 14, 23–26]. This results in a bleaching in the center and enhanced absorption at the wings of the surface plasmon resonance. Comparing the differential reflection spectra [Fig. 6.1(b)], $\Delta R/R$, with the stationary reflection spectrum [Fig. 6.1(a), solid line] we observe that the areas of enhanced absorption (i.e. reduction of the $\Delta R/R$) around 550 nm and 680 nm coincide with the reflection maxima denoted by P2, P3, and P4 in the linear spectra. In contrast, the positive peak of the $\Delta R/R$ at 610 nm [Fig. 6.1(b)] coincides with a dip in the reflectivity denoted by D2 [Fig. 6.1(a)]. In Chapter 5 this dip was attributed to the surface plasmon resonance and our present observation confirms this conclusion. Indeed, the optical excitation of the electrons broadens the D2 surface plasmon resonance, decreases the absorption, and increases the reflectivity at the plasmon resonance.

6.5 Calculation of the transient reflectivity

Our photonic crystal is composed of two components: silica and gold, of which only gold can absorb light at 800 nm. As mentioned above the observed dynamics of $\Delta R/R$ on the picosecond time scale is far too fast to be caused by geometrical changes in the spheres and, for that matter, in the lattice parameter of the photonic crystal, and must be due to transient modulation of the dielectric constant of gold.

6.5.1 Ultrafast dynamics in gold

The dynamical changes of the optical properties of gold induced by ultrashort optical pulses are commonly assigned to the excitation of the free electron gas [8–14]. The widely accepted model for the electron dynamics feature four steps (see Fig. 6.3).

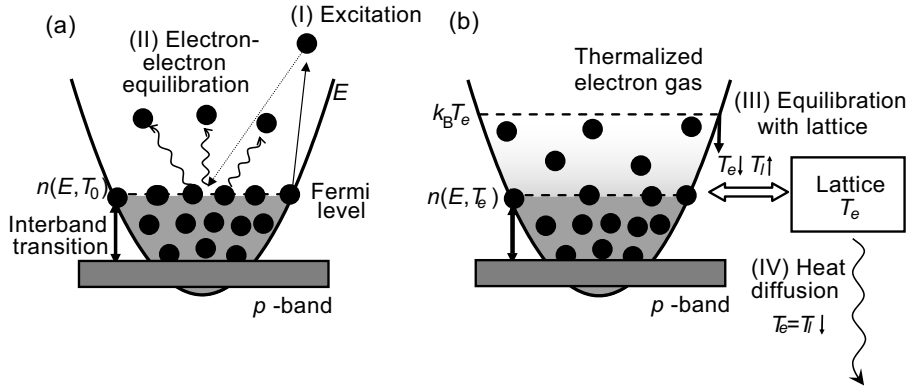


FIGURE 6.3 Schematics of ultrafast dynamic in gold. (a) Optical excitation of electron gas followed by thermalization; (b) Equilibration of electrons and lattice followed by heat diffusion from the excited volume to the surroundings.

(I) Excitation. In the first step, part of the pump pulse is absorbed by electrons. In our particular case, the photon energy of the pump light ($\hbar\omega = 1.55$ eV) is below the energy transition from the d band to the Fermi level near the L -point, $\hbar\Omega_L = 2.3$ eV, and below d - p transition near the X -point, $\hbar\Omega_X = 1.7$ eV. Therefore, electrons are predominantly excited via surface plasmons, which dephase on a timescale well below 100 fs. At the first moment following plasmon excitation and dephasing into individual electron excitations, the electrons have a non-Fermi-Dirac energy distribution with some hot electrons but leaving the main part cold [11]. Therefore, the initial change of the dielectric constant of gold $\Delta\epsilon_{Au}$, and hence $\Delta R/R$, is very weak. This is in contrast to the dynamics generally observed in semiconductors (see Section 3.2), where at a sufficient level of optical excitation virtually all electrons are initially hot and reflectivity changes appear instantaneously with the pump excitation pulse.

(II) Thermalization of the electron gas. In the second step, the excited electrons equilibrate with the remaining free electrons [11]. This changes the occupation numbers of the electronic state near the Fermi level that alter the absorption. Within the first picosecond, the electron energies reach a new Fermi-Dirac distribution and the amplitude of $\Delta\epsilon_{Au}$ its maximum value. However, up to this moment the lattice remains cold and the hot electron gas is far from equilibrium with the lattice.

(III) Equilibration of the electron gas with the lattice. In the third step, free electrons lose their energy via electron-phonon interaction to the lattice.

Consequently, the electron temperature decreases leading to a recovery of $\Delta\varepsilon_{Au}$. Generally, the electron-phonon exchange time τ_{e-ph} depends on the size of the gold particles. However, for particles sufficiently larger than 10 nm this effect is negligible and $\tau_{e-ph} \approx 1$ ps [27].

(IV) Heat diffusion. In the forth and last step, the lattice cools down via heat transfer to the surrounding temperature bath. The rate of this process depends on the size of the excited volume and the heat conductivity, but is much slower than our experimental window allows to monitor.

6.5.2 Two-temperature model

The dynamics of the electron temperature in the third step can readily be described by the so-called “two-temperature model” [28, 29]. This model assumes that both electrons and phonons are in internal thermal equilibrium but not in mutual equilibrium. In that case, these subsystems can be characterized by an electron temperature T_e and a lattice temperature T_l , respectively. The relaxation dynamics of these temperatures follows from the heat exchange equation,

$$\begin{aligned} C_e \frac{\partial T_e}{\partial t} &= \nabla \cdot (\kappa \nabla T_e) - G_{e-p} (T_e - T_l) + h(r, t) \\ C_l \frac{\partial T_l}{\partial t} &= -G_{e-p} (T_l - T_e), \end{aligned} \quad (6.1)$$

where $C_e = 1/3\pi^2 D_f k_B^2 T_e = \gamma T_e$ [30] and C_l are the electronic and lattice heat capacities, respectively, and G_{e-p} represents the electron-phonon coupling constant. Further, κ is the thermal conductivity of the electrons, k_B the Boltzmann constant, D_f the electronic density of states at the Fermi level, and $h(r, t)$ the electron heating source term. Since the duration of the pump pulse is much shorter than the electron-phonon interaction, $h(r, t)$ can readily be considered as a δ -function. For gold $\gamma = 67 \text{ J m}^{-3} \text{ K}^{-2}$, $C_l = 2.5 \times 10^6 \text{ J m}^{-3} \text{ K}^{-1}$, and $G_{e-p} \approx 3 \times 10^{16} \text{ W m}^{-3} \text{ K}^{-1}$ [10, 12, 13]. The “two-temperature model” assumes that electron-electron thermalization appears much faster than equilibration with the lattice. In case of weak excitation, when $\Delta T_e < T_e$, this assumption may not be valid [11, 13, 31], and the measured dynamics in the low-excitation limit appears to be slower than predicted by the model. However, at high degrees of excitations, relevant for the present experiments, the electron-electron interaction speeds up and the electron gas can be treated as being in internal equilibrium [32]. In our experiment the excitation is close to the damage threshold and we believe that the two-temperature model is quite suitable for our case.

Further, we assume that hot electrons, by virtue of their high Fermi velocities tend to quickly spatially homogenize the hot electron distribution over the shell and omitting the diffusion term in Eq. (6.1), we arrive at two coupled non-linear differential equations

$$\begin{aligned}\gamma T_e \frac{\partial T_e}{\partial t} &= -G_{e-p}(T_e - T_l) \\ C_l \frac{\partial T_l}{\partial t} &= -G_{e-p}(T_l - T_e),\end{aligned}\tag{6.2}$$

which can be solved analytically. We observe that the decay of the electron temperature is characterized by a time constant $\tau = \gamma T_e / G_{e-p}$, which depends on the electron temperature. This implies that the decay is slower for higher temperatures. This elongation of the equilibration dynamics with increasing excitation power was indeed observed experimentally [8, 33]. Further, in case of very high electron temperature $T_e \gg T_l$ the electron temperature will linearly decrease in time. In the opposite case $(T_e - T_l) \ll T_l$, the electron temperature will exponentially decay to a final equilibrium temperature, T_∞ , which can be calculated from the energy balance between the electron gas and the lattice, noting that $C_e \ll C_l$,

$$T_\infty - T_0 = \frac{\gamma}{2C_l} (T_e^i)^2,\tag{6.3}$$

where T_e^i is the initial temperature of the electron gas after the excitation, T_0 the temperature of the electron gas and lattice before the excitation ($t < 0$).

In order to solve the differential equations (6.2) we neglect the small variation of T_l comparing with the large variation of T_e , ($\partial T_l / \partial t \ll \partial T_e / \partial t$). This approach is accurate because $\gamma T_e \ll C_l$ and allows us to omit the second equation in (6.2). Assuming in first approximation $T_l \approx T_\infty$ we are left with solving

$$\gamma T_e \frac{\partial T_e}{\partial t} = -G_{e-p}(T_e - T_\infty).\tag{6.4}$$

The solution of this equation is

$$T_e(t) = T_\infty W \left[\chi \exp \left(\chi - \frac{G_{e-p}}{\gamma T_\infty} t \right) \right] + T_\infty,\tag{6.5}$$

where $W(t)$ is the Lambert function and $\chi = (T_e^i - T_\infty) / T_\infty$. Corresponding changes in T_l are approximately

$$T_l(t) - T_0 \approx \frac{G_{e-p}}{C_l} \int_0^t (T_e(\tau) - T_\infty) d\tau. \quad (6.6)$$

The electron temperatures T_e^i and T_∞ can be estimated within this model from the experimental curve $\Delta R(t)/R$ vs t shown in Fig. 6.2. Assuming a linear relation between ΔT_e and ΔR , the transient reflectivity can be estimated by

$$\frac{\Delta R(t)}{R} = \{A [T_e(t) - T_0] + B [T_l(t) - T_0]\} \exp(-t/\tau_c). \quad (6.7)$$

Here, the first and second terms on the right hand correspond to the electron and lattice contributions, respectively. Exponential decay, characterized by τ_c , accounts for residual coupling with the core and parameters A , B , τ_c , and T_e^i can be found from the experimental data.

In Fig. 6.2 dotted line shows a fit of the experimental $\Delta R(t)/R$ using Eq. (6.7). From the fit we obtain $A = -8 \times 10^{-3} \text{ K}^{-1}$, $B = -9 \times 10^{-3}$, $\tau_c = 350 \text{ ps}$, and $T_e^i = 4100 \text{ K}$. Further, inserting T_e^i in Eq. (6.3) we find $T_\infty - T_0 = 225 \text{ K}$.

We note, that the estimated $T_\infty = 518 \text{ K}$ for $T_0 = 293 \text{ K}$ is close but slightly below the melting threshold $T_m = 600 \text{ K}$ reported for similar gold shells capped by a 6 – 8 nm silica shell [34]. Indeed, we observed irreversible changes in the reflection spectra already for pump fluences of about 2 times higher than used for the measurements in Fig. 6.2.

6.5.3 Calculation of the transient reflectivity

Assuming a small change in the dielectric function, $\Delta \varepsilon' \ll \varepsilon'$ and $\Delta \varepsilon'' \ll \varepsilon''$, the transient reflectivity can be written in the following form

$$\frac{\Delta R}{R} = \frac{\partial R}{R \partial \varepsilon'} \Delta \varepsilon' + \frac{\partial R}{R \partial \varepsilon''} \Delta \varepsilon''. \quad (6.8)$$

The partial derivatives can subsequently be calculated in the framework of the layered variant of the photonic Korringa-Kohn-Rostocker method (LKRR) described in Chapter 5. As a starting point we again take the reflection spectrum of a single layer of gold nanoshells deposited on a silicon substrate calculated in Chapter 5. For the sake of clarity we reproduce this spectrum in Fig. 6.4(a). The partial derivatives in Eq. (6.8) were obtained by calculating the spectrum with a slightly different dielectric constant $\varepsilon + \varepsilon_\Delta$ where $\text{Re}(\varepsilon_\Delta) \ll \varepsilon'$ and $\text{Im}(\varepsilon_\Delta) \ll \varepsilon''$, subtracting the result from the spectrum of Fig. 6.4(a) and normalizing to it. For this calculation we again used the computer code written by A. Moroz.

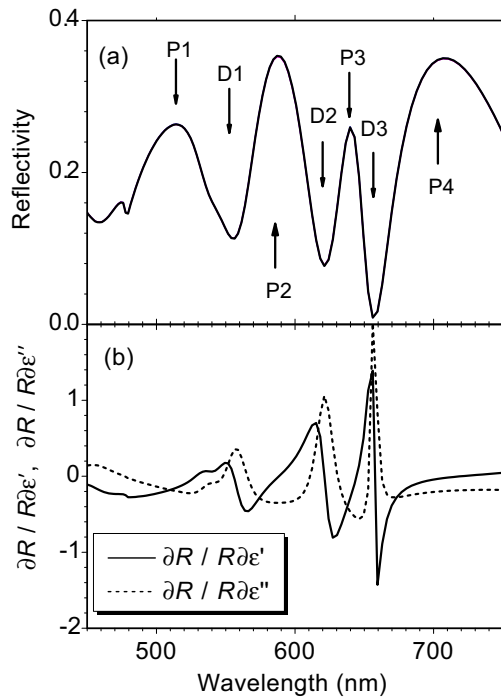


FIGURE 6.4 (a) Calculated reflection spectrum of a single close-pack hexagonal layer of the gold-shell particles on an infinite silicon substrate [the same as in Fig. 5.6(b)] and (b) corresponding $\partial R/R\partial\epsilon'$ (solid line) and $\partial R/R\partial\epsilon''$ (dotted line) calculated for the dielectric constant of bulk gold taken at room temperature.

In the calculation we inserted the refractive index of silica $n(\text{SiO}_2) = 1.45$, the wavelength-dependent dielectric constant of gold [35] depicted in Fig. 5.9, and the geometrical parameters of the particles, $r_1 = 228$ nm, $r_2 = 266$ nm, and $r_3 = 276$ nm. The results of the computations are shown in Fig. 6.4(b). The computed partial derivatives confirm that the dips D1, D2, and D3 of the $\Delta R/R$ in Fig. 6.4(a) rather than the maxima correspond to the plasmon resonances. As a natural feature of an optical resonance, the reflectivity is sensitive to the $\Delta\epsilon''$ at the center and to the $\Delta\epsilon'$ at the side of the resonances, respectively. It is also clear that for non-zero $\Delta\epsilon''$ the response in $\Delta R/R$ will be spectrally asymmetric.

In order to estimate the magnitude of $\Delta R/R$, the dielectric constant of gold need to be calculated at a given electron temperature.

6.5.4 Temperature dependence of the dielectric constant of gold

The dielectric constant of gold $\varepsilon = \varepsilon' + i\varepsilon''$ can be separated into interband and intraband Drude contribution of the free electrons

$$\varepsilon = \varepsilon_{IB} + \varepsilon_D. \quad (6.9)$$

In the following we will neglect the intraband contribution and focus on the interband part, which was found to be the most important for the changes in surface-plasmons resonances with electron temperature [24]. The imaginary part of the dielectric constant due to the interband absorption was found to be [13, 36]

$$\varepsilon''_{IB}(\omega, T_e) = \frac{8\pi^2 e^2 \hbar^2}{3m_0^2 \omega^2} |M_{p-d}|^2 \int D(E, \omega) [1 - n(E, T_e)] dE, \quad (6.10)$$

where m_0 is the free electron mass, e the charge of electron, ω frequency of light, M_{p-d} the transition matrix element, E the energy, and $n(E, T_e)$ the Fermi distribution function. Further, $D(E, \omega)$ is the energy distributed joint density of states given by

$$D(E, \omega) \propto \frac{\Theta[v_d \hbar (\omega - \omega_{d-p}) - E]}{\sqrt{v_d \hbar (\omega - \omega_{d-p}) - E}}, \quad (6.11)$$

with the Heaviside step function Θ and $v_d = m_p / (m_p + m_d)$, where m_p and m_d are the effective masses for the p and d bands [13]. For gold $\hbar\omega_{d-p} = 2.38$ eV and $v_d = 0.86$.

The real part of the dielectric constant can be obtained from the Kramers-Krönig relations [37],

$$\varepsilon'_{IB}(\omega, T_e) = \frac{2}{\pi} \mathcal{P} \int_0^\infty \frac{\omega' \varepsilon''_{IB}(\omega', T_e)}{\omega'^2 - \omega^2} d\omega', \quad (6.12)$$

where \mathcal{P} denotes the Cauchy principal value of the integral.

The change in the dielectric constant of gold induced by a temperature rise from $T_0 = 293$ K to T_e^i , $\Delta\varepsilon = \varepsilon(T_e^i) - \varepsilon(T_0)$ was calculated by a computer program made by O. L. Muskens [38]. As an example, in Fig. 6.5 we plot the real (solid line) and imaginary (dashed line) parts of the difference in the dielectric constants of gold calculated for $T_e = 2000$ K and room temperature.

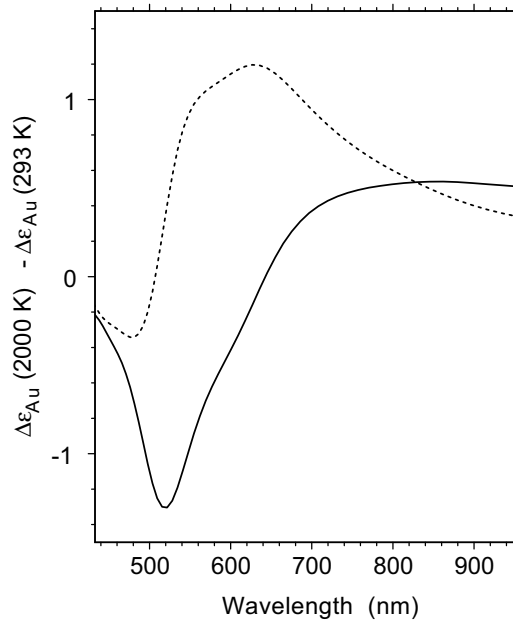


FIGURE 6.5 Modulation of the real (solid line) and imaginary (dotted line) parts of the dielectric constant of gold caused by electron heating from 293 K to 2000 K.

6.5.5 Comparison of the experiment and calculations results

Now we are in the position to calculate the difference in the reflection spectra of the gold-shell photonic crystal induced by a large nonequilibrium electron temperature T_e^i . $\Delta R/R$ can be obtained from the curves of Fig. 6.4(b) with those from Fig. 6.5 as long as the curves in Fig. 6.4(b) have a sufficiently weak temperature dependence. To check this, we performed the direct calculation of $\Delta R/R$ using the correct function $\varepsilon(\lambda, T_e)$ and compare result with the simple approach. The result of the calculations is shown in Fig. 6.6(b) and demonstrate the validity of the simple approach in the visible spectral range except around the narrow resonances in Fig. 6.4(b).

In Fig. 6.6 we compare the measured and the calculated $\Delta R/R$. In Fig. 6.6(a) we reproduce the experimentally detected $\Delta R/R$ of Fig. 6.1(b) taken at 0.5 ps delay after optical excitation. According to our estimation made in the framework of two-temperature mode and discussed in Section 6.5.2, the effective temperature of the electron gas at a given delay is $T_e \sim 4100$ K. In Fig. 6.6(b) we show the calculated spectrum of the $\Delta R/R$ for $T_e = 2000$ K using Moroz's computer pro-

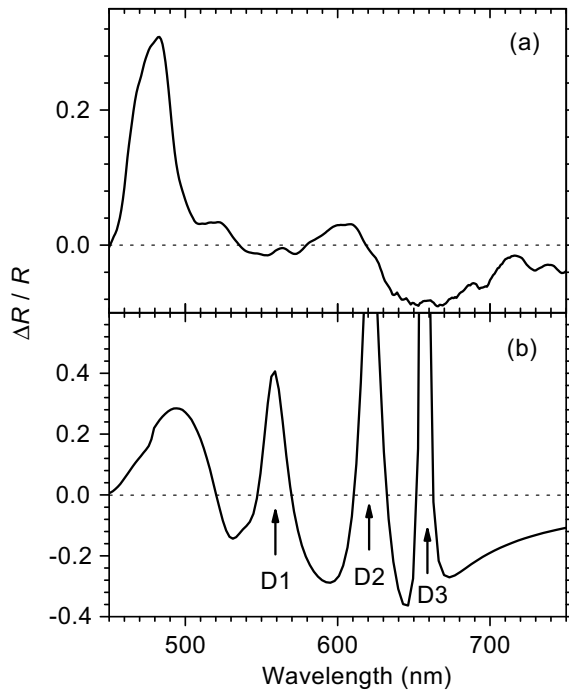


FIGURE 6.6 (a) Experimental and (b) calculated spectra of the differential reflectivity. Calculation performed for $T_e = 2000$ K .

gram for a one-layer photonic crystal of our core-shell particles. The calculated spectrum has four peaks. Two of them, at 490 nm and 620 nm, roughly coincide with the experimental ones, but the remaining ones at 560 nm and 660 nm were not reproduced in the experiment. This discrepancy is not unexpected, because of the unfortunate deviations between the already measured and calculated *linear* spectra for our sample, the solid lines in Fig. 6.1(a) and Fig. 6.4(a), respectively. In the calculated spectrum the dips D1 and D3 are quite suppressed but visible.

Another deviation of the calculation forms the absolute values found for $\Delta R/R$. Although the measured and calculated spectra of $\Delta R/R$ coincide at 490 nm, for the remaining part of the spectrum the calculated $\Delta R/R$ are overestimated already at 2000 K, and for 4100 K even more. These discrepancies, perhaps, can be accounted for by the polydispersity of the gold-shell spheres, which is apparent from SEM measurements and amounts to $\sim 5\%$. Unfortunately, this spurious effect cannot easily be taken into account in the calculation scheme. Indeed, polydispersity of the particles results in inhomogeneous broadening of the plasmon resonances.

As a result, the sharp peaks in the transient reflectivity spectra will be “washed out” and the resulting amplitude of $\Delta R/R$ will decrease. We speculate that the overestimation of $\Delta R/R$ by the theory can also be partly explained by a higher initial absorption of gold shell than was accounted by the theory. Indeed, our theory assumes the bulk dielectric constant of gold. However, the dielectric constant of the gold shell can deviate from the bulk value because of the enhanced electron scattering at the metal-silica interfaces and imperfections in the gold shell. The enhanced scattering may account for increase in absorption in gold nanoshells that, in turn, makes plasmon resonance broader. As a result, the nonlinear changes will come less pronounced.

In spite of the fact that our calculations fail to fully explain our experimental curves for $\Delta R/R$, they correctly predict the order of magnitude and produce reasonably good qualitative agreement with the experiment. Indeed, the calculations yield the correct sign of the $\Delta R/R$ for *all* wavelengths excluding the resonances D1 and D3, at 550 nm and 650 nm, respectively. Moreover, the theory predicts correctly the sharp positive peak of the $\Delta R/R$ that corresponds to the resonance D2 at 620 nm.

Finally, we discuss irreversible changes of the sample following very strong optical excitation, above the damage threshold.

6.6 Irreversible changes following excitation above the threshold limit

At pump fluences exceeding 1 mJ/cm^2 , we observed irreversible changes in the reflectivity. The intensities of the P1 and P2 in the linear reflection spectrum [Fig. 6.1(a)] decrease and do not recover even in the case the pump pulses are switched off. However, the intensity of P4 remained constant. We attribute this phenomenon to “melting” of the photonic crystal, - i.e. breaking long-distance periodicity due to spatial disordering of the gold-nanoshell particles. Disorder leads to nonreversible changes in the blue and the green parts of the stationary and transient reflectivity spectra, which were found to be quite sensitive to the particle ordering (see Chapter 5).

At even higher intensities i.e. above 1.5 mJ/cm^2 , the reflectivity drops irreversibly over the entire spectrum by several orders of magnitude. Figure 6.7(a) demonstrates an SEM image of a non-damaged area in the sample and Fig. 6.7(b) a part damaged by the optical irradiation. We see that the ordering of particles is completely lost. Moreover, the concentration of the particles is significantly lower than in non-damaged area due to “evaporation” from the excited volume, which

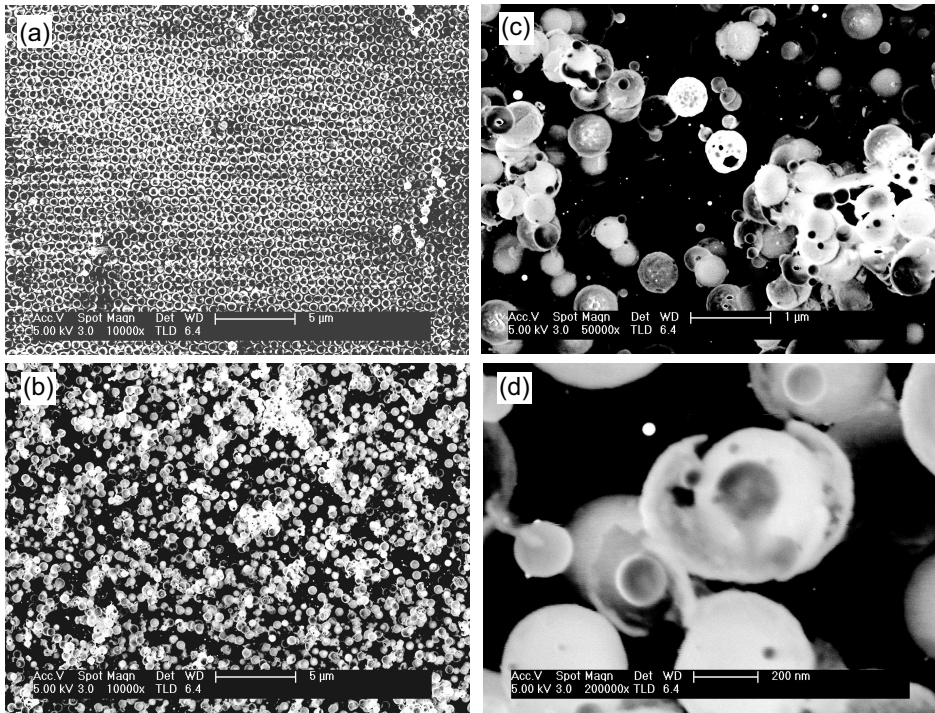


FIGURE 6.7 SEM image of (a) non-irradiated area of the photonic crystal, (b), (c), and (d) damages induced by a strong irradiation of the sample surface. (c) and (d) are taken with higher magnifications.

naturally explains the observed decrease in reflectivity. In the “area of disaster” shown in Fig. 6.7(c) and (d) with higher magnification, we observe that particles have desintegrated, possibly due to explosive melting of gold.

6.7 Conclusions

In this Chapter, we analyzed the dynamic changes in the reflectivity spectra of gold-nanoshell 3D photonic crystals induced by strong optical pump pulses. Sub-picosecond ultrafast changes in the reflectivity were induced by 800-nm optical excitation with 120-fs pulse. The observed changes in the reflectivity reach values as high as 35% for pump power fluences of about 0.5 mJ/cm^2 , one-order-of-magnitude lower than needed to induce comparable changes in silicon (Chapter 3) and vanadium dioxide (Chapter 4) photonic crystals. The dynamics of the tran-

sient changes in the reflectivity is controlled by hot electrons and was analyzed in the framework of the “two-temperature model”. The observed temporal evolution of the transient reflectivity exhibits a form described by non-linear differential equations of the two-temperature model, yielding in our specific case electron temperatures as high as 4100 K and inducing lattice temperatures of 518 K. On longer time scales, the transient reflectivity is governed by heat diffusion that accounts for the decay on the nanosecond time scale.

The transient changes in the reflectivity appeared to strongly depend on wavelength. We observed pronounced peaks in the spectrum of the transient reflectivity, which we attributed to photoinduced quenching of the surface plasmon resonance. The obtained experimental results appeared to be in qualitative agreement with theory.

References

- [1] A. E. Neeves and M. H. Birnboim, *Opt. Lett.* **13**, 1087 (1988).
- [2] N. Kalyaniwalla, J. W. Haus, R. Inguva, and M. H. Birnboim, *Phys. Rev. A* **42**, 5613 (1990).
- [3] J. W. Haus, H. S. Zhou, S. Takami, M. Hirasawa, I. Honma, and H. Komiyama, *J. Appl. Phys.* **73**, 1043 (1993).
- [4] S. Collin, F. Pardo, and J.-L. Pelouarda, *Appl. Phys. Lett.* **83**, 1521 (2003).
- [5] S. Collin, F. Pardo, R. Teissier, and J. L. Pelouard, *Appl. Phys. Lett.* **85**, 194 (2004).
- [6] J. W. Haus, N. Kalyaniwalla, R. Inguva, M. Bloemer, and C. M. Bowden, *J. Opt. Soc. Am. B* **6**, 797 (1989).
- [7] R. D. Averitt, S. L. Westcott, and N. J. Halas, *Phys. Rev. B* **58**, 10203 (1998).
- [8] H. E. ElsayedAli, T. Juhasz, G. O. Smith, and W. E. Bron, *Phys. Rev. B* **43**, 4488 (1991).
- [9] C.-K. Sun, F. Vallée, L. Acioli, E. P. Ippen, and J. G. Fujimoto, *Phys. Rev. B* **48**, 12365 (1993).
- [10] W. S. Fann, R. Storz, H. W. K. Tom, and J. Bokor, *Phys. Rev. Lett.* **68**, 2834 (1992).
- [11] W. S. Fann, R. Storz, H. W. K. Tom, and J. Bokor, *Phys. Rev. B* **46**, 13592 (1992).
- [12] T. Juhasz, H. E. ElsayedAli, G. O. Smith, C. Suárez, and W. E. Bron, *Phys. Rev. B* **48**, 15488 (1993).
- [13] R. H. M. Groeneveld, R. Sprik, and A. Lagendijk, *Phys. Rev. B* **51**, 11433 (1995).
- [14] M. Perner, P. Bost, U. Lemmer, G. von Plessen, J. Feldmann, U. Becker, M. Mennig, M. Schmitt, and H. Schmidt, *Phys. Rev. Lett.* **78**, 2192 (1997).
- [15] A. E. Neeves and M. H. Birnboim, *J. Opt. Soc. Am. B* **6**, 787 (1989).
- [16] R. D. Averitt, D. Sarkar, and N. J. Halas, *Phys. Rev. Lett.* **78**, 4217 (1997).
- [17] S. I. Bozhevolnyi, J. Beermann, and V. Coello, *Phys. Rev. Lett.* **90**, 197403 (2003).
- [18] C. Graf and A. van Blaaderen, *Langmuir* **18**, 524 (2002).
- [19] L. M. Liz-Marzán and P. Mulvaney, *J. Phys. Chem. B* **107**, 7312 (2003).

-
- [20] A. Moroz, Phys. Rev. Lett. **83**, 5274 (1999).
- [21] A. Moroz, Phys. Rev. B **66**, 115109 (2002).
- [22] O. L. Muskens, Ph.D. thesis, Universiteit Utrecht (2004).
- [23] J. H. Hodak, I. Martini, and G. V. Hartland, J. Phys. Chem. B **102**, 6958 (1998).
- [24] H. Inouye, K. Tanaka, I. Tanahashi, and K. Hirao, Phys. Rev. B **57**, 11334 (1998).
- [25] S. L. L. ans T. S. Ahmadi, M. A. ElSayed, J. T. Khoury, and R. L. Whetten, J. Phys. Chem. **101**, 3713 (1997).
- [26] C. Voisin, D. Christofilos, P. A. Loukakos, N. D. Fatti, F. Vallée, J. Lermé, M. Gaudry, M. P. E. Cottancin, and M. Broyer, Phys. Rev. B **69**, 195416 (2004).
- [27] A. Arbouet, C. Voisin, D. Christofilos, P. Langot, N. D. Fatti, F. Valée, J. Lermé, G. Celep, E. Cottancin, M. Gaudry, et al., Phys. Rev. Lett. **90**, 177401 (2003).
- [28] M. I. Kaganov, I. M. Lifshitz, and L. V. Tanatarov, Sov. Phys. JETP **4**, 173 (1957).
- [29] S. I. Anisimov, B. L. Kapeliovich, and T. L. Perel'man, Sov. Phys. JETP **39**, 375 (1974).
- [30] C. Kittel, *Introduction to Solid State Physics* (John Wiley, New York, 1986).
- [31] D. Bejan and G. Raseev, Phys. Rev. B **55**, 4250 (1997).
- [32] B. Rethfeld, A. Kaiser, M. Vicanek, and G. Simon, Phys. Rev. B **65**, 214303 (2002).
- [33] J. H. Hodak, A. Henglein, and G. V. Hartland, J. Phys. Chem. B **104**, 9954 (2000).
- [34] C. Radloff and N. J. Halas, Appl. Phys. Lett. **79**, 674 (2001).
- [35] *Optical properties of metals*, vol. 2 (Fachinformationszentrum Energie, 1981).
- [36] R. Rosei, F. Antonangeli, and U. M. Grassano, Surf. Sci. **37**, 689 (1973).
- [37] L. D. Landau and E. M. Lifshitz, *Electrodynamics of continuous media*, vol. 8 of *Course of Theoretical Physics* (Pergamon, Oxford, 1975).
- [38] O. L. Muskens, Master's thesis, Universiteit Utrecht (1999).

CHAPTER 7

COHERENT VIBRATIONS OF SUBMICRON GOLD SHELLS

Abstract

We demonstrate coherent acoustic radial oscillations of a submicron gold shell loosely bound to a silica core. The vibrational mode is excited by an ultrafast optical pulse and appears as a pronounced modulation of the transient reflectivity on the subnanosecond time scale. The frequency of these oscillations is demonstrated to be in excellent agreement with Lamb theory.

7.1 Introduction

In the previous chapter, we demonstrated the dynamic response of silica-core gold-shell photonic crystal to a femtosecond optical pulse. On the picosecond time scale, the transient reflectivity appeared to be governed by electrons. In this chapter, we examine the dynamical optical response of the same sample on the subnanosecond time scale, on which the optical properties are mainly governed by lattice motion. In composite structures such as photonic crystals, these motions are expected to be localized in a small volume because the mechanical interparticle coupling is small [1]. If the typical size of the vibrational volume is sufficiently small this motion produces a discrete spectrum of energies. Such modes have been observed in Raman scattering experiments [2–4] and in time-domain pump-probe spectroscopy [5–12]. In the latter case the acoustic vibrations were excited by an ultrashort pulse that excites the electron gas, which in turn, induces a lattice stress via electron-phonon interaction setting up a coherent vibration. To date coherent excitation of the breathing modes has been demonstrated in silver [5], gold [6, 7], tin [8], and gallium [8] solid spheres, silver ellipsoids [9], gold nanorods [10], and bimetallic core-shell particles [11, 12]. In most of these experiments, the frequency of coherently excited breathing vibrations was demonstrated to be in a good agreement with the calculations. However, even in bimetallic spheres only

one acoustic mode has been detected - the ground mode of the radial vibration of the solid sphere. Recently, a quadrupolar-hollow-shell mode was observed in Raman scattering in nickel-silver core-shell nanoparticles [4]. In this chapter we demonstrate for the first time a time-resolved coherent oscillation of a nanometer-thick gold shell loosely bound to an inner silica core of submicrometer diameter.

7.2 Coherent excitation of acoustic modes

For our experiments we used the 3D photonic crystal composed of core-multishell spheres. Each particle consists of a 228-nm silica core, a 38-nm gold shell, and a 10-nm silica outer shell [13]. The geometrical parameters of this sample, its linear response, and ultrafast nonlinear optical properties were described in Chapter 5 and 6. Acoustic modes have been excited by a 120-fs pulse extracted from a femtosecond amplified Ti-sapphire laser operating at 1 kHz. The transient reflectivity induced by the optical excitation was registered in exactly the same way as described in Section 6.2.2. For our studies we select a highly ordered area of the sample containing more than five layers of particles. Linear reflection spectra taken in those areas have a shape as depicted in Fig. 5.6.

In Figure 7.1, the solid lines show evolutions of the transient reflectivity, $\Delta R/R$, registered at (a) 950 nm and (b) 700 nm. Inset in Fig. 7.1(b) shows the signal at 700 nm including the fast decay of the electronic contribution. Both curves demonstrate an intense and sharp peak with a duration of several picoseconds immediately after the optical excitation. This peak has been analyzed in detail in Chapter 6 and was attributed to the rapid cooling of the photoexcited electron gas. In Fig. 7.1(a) and (b), we observe pronounced oscillations of the reflectivity with a period of about 400 ps. The amplitude of these oscillations appeared to depend on the probe wavelength, λ . The maximum amplitude of the oscillations was registered at $\lambda = 950$ nm and amounts to as much as 4% from the total reflection intensity [Fig. 7.1(a)]. At $\lambda = 700$ nm, the amplitude of the oscillations is smaller but still quite sizable. Further, we did observe weak oscillations at 605 nm (not shown in Fig. 7.1) but found no oscillations in the spectral ranges of 500–590 nm and 640–780 nm. Unfortunately, the spectral range of 740–850 nm was not accessible for measurements because of the presence of elastic scattering of the intense 800-nm pump beam. It is interesting to note that the dependencies at 950 nm and 700 nm have the same signs for the initial fast electron peaks while the slow oscillations have opposite polarities. The temporal evolution of the slow oscillations can be approximated quite faithfully by the function

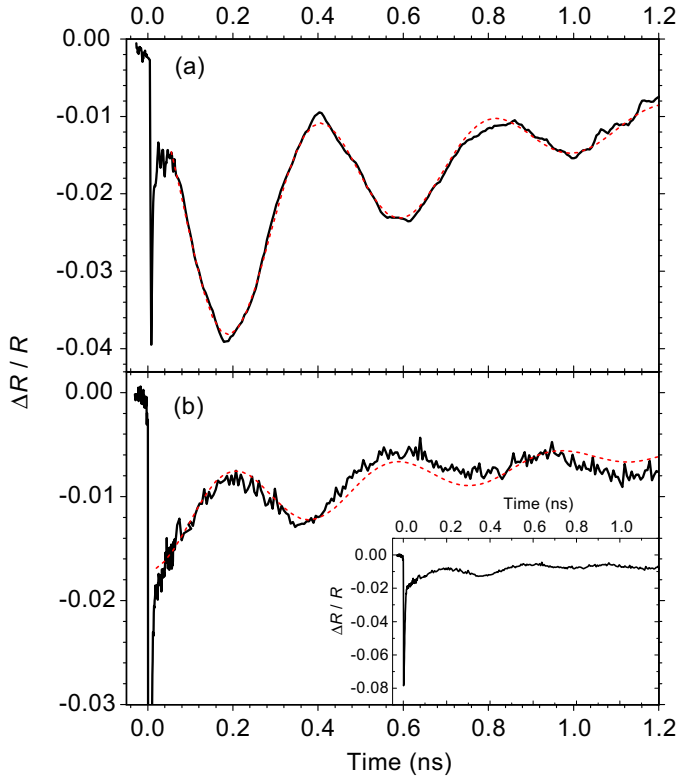


FIGURE 7.1 Transient reflectivity dynamics of the gold-shell photonic crystal measured at (a) 950 nm and (b) 700 nm. Solid lines depict experimental data, dotted show the fits. Inset shows the signal measured at 700 nm plotted including the entire electronic contribution.

$$\frac{\Delta R}{R} = A_1 \exp(-t/\tau_1) \cos\left(\frac{2\pi}{T}t + \varphi\right) + A_2 \exp(-t/\tau_2). \quad (7.1)$$

Here, t is time and the fitting parameters T and φ are the period and phase of the oscillations, respectively, τ_1 and τ_2 decay times, and A_1 and A_2 amplitudes referring to the oscillatory and non-oscillatory decay, respectively. The best fits of $\Delta R/R$ for 950 nm and 650 nm are shown by dotted lines in Fig. 7.1(a) and (b), respectively, and track the experiments excellently. The set of values of the fitting parameters for the different wavelengths are collected in Table 7.1. It is remarkable that the period and the phase of the oscillations are almost the same over the full spectral range. Moreover, τ_1 and τ_2 also appeared to be virtually

Wavelength, nm λ	Fitting parameters					
	A_1	A_2	τ_1 , ps	τ_2 , ps	T , ps	φ , rad
950	-0.021	-0.028	482	1176	406	0
700	0.0047	-0.015	633	1510	378	0.08π
600	0.0043	-0.025	770	>1000	381	-0.06π
Average	depends on λ	depends on λ	600 ± 200	1300 ± 300	390 ± 20	$0 \pm 0.1\pi$

TABLE 7.1 Fitting parameters of the transient reflectivity using Eq. (7.1). Last row summarizes average values from different measurements.

independent of the selected wavelengths. The last line in the Table 7.1 shows the average values for the fitting parameters collected at different wavelengths and points on the sample. We note that the detected phase of the oscillations is zero radians and the period of oscillation is 390 ps with a standard deviation of 5%.

7.3 Interpretation of the experimental results

The dynamics of the reflectivity during the first 10 ps has already been analyzed in Chapter 6. The initial peak in the transient reflectivity was attributed to the changes in the dielectric constant of gold induced by hot electrons. The subsequent dynamics lasts no longer than 20 ps and was attributed to equilibration of the electron gas with the lattice. At the same time, the sign of the subnanosecond oscillations observed in the transient reflectivity (Fig. 7.1) can deviate from the sign of the electronic effect. Therefore, the nature of this oscillation can not be found in electron-temperature variations. We attribute the 400-ps oscillation in the transient reflectivity to acoustic vibrations of the submicron gold-shells coherently excited by an impulsive stress. As noted in the Introduction, similar oscillations have been recently reported for solid spherical metal particles [5–7].

7.4 Lamb modes

The problem of a vibrating sphere was first addressed by Poisson [14]. The fundamental acoustic modes of an elastic sphere were classified later by Jaerish [15]. The complete analysis of the acoustic vibrations of a free elastic sphere was obtained by Lamb [16, 17]. He found explicit analytical solutions for the eigenfunctions and eigenfrequencies of a solid sphere. He also extended this analysis for the case of a free-standing thin hollow sphere [17].

The wave equation for elastic, and isotropic media has the form [18]

$$\frac{\partial^2 \mathbf{u}}{\partial t^2} = (c_l^2 - c_t^2) \nabla (\nabla \cdot \mathbf{u}) + c_t^2 \nabla^2 \mathbf{u}, \quad (7.2)$$

where t is time and \mathbf{u} the lattice displacement. Further c_l and c_t are the longitudinal and transverse sound velocities, respectively. For periodic oscillations $u \sim \exp(-i\Omega t)$, where Ω is the frequency, Eq. (7.2) reduces to

$$(c_l^2 - c_t^2) \nabla (\nabla \cdot \mathbf{u}) + c_t^2 \nabla^2 \mathbf{u} + \Omega^2 \mathbf{u} = 0. \quad (7.3)$$

Accounting for the spherical symmetry of our particles, we express the solution of Eq. (7.3) in spherical coordinates (r, φ, θ)

$$\begin{aligned} u_r &= \frac{\partial \Upsilon_{ml}(h_l r)}{\partial r} + l \left\{ \frac{\partial^2 [r \Upsilon_{ml}(h_l r)]}{\partial r^2} - r \nabla^2 \Upsilon_{ml}(h_l r) \right\}, \\ u_\theta &= \frac{1}{r} \frac{\partial \Upsilon_{ml}(h_l r)}{\partial \theta} + \frac{1}{\sin \theta} \frac{\partial \Upsilon_{ml}(h_l r)}{\partial \varphi} + \frac{l}{r} \frac{\partial^2 [r \Upsilon_{ml}(h_l r)]}{\partial r \partial \theta}, \text{ and} \\ u_\varphi &= \frac{1}{r \sin \theta} \frac{\partial \Upsilon_{ml}(h_l r)}{\partial \varphi} + \frac{\partial \Upsilon_{ml}(h_l r)}{\partial \theta} + \frac{l}{r \sin \theta} \frac{\partial^2 [r \Upsilon_{ml}(h_l r)]}{\partial r \partial \varphi}, \end{aligned} \quad (7.4)$$

with u_r , u_θ , and u_φ the radial and the angular displacements, respectively, $h_l = \Omega/c_l$, $h_t = \Omega/c_t$, and Υ_{ml} the spherical distribution function,

$$\begin{aligned} \Upsilon_{lm}(kr) &= \left(A_l \sqrt{\frac{\pi}{2kr}} J_{l+1/2}(kr) + B_l \sqrt{\frac{\pi}{2kr}} Y_{l+1/2}(kr) \right) \\ &\quad \times P_{lm}(\cos \theta) e^{im\varphi - i\omega t}. \end{aligned} \quad (7.5)$$

Here, A_l and B_l are constants to be determined from the boundary conditions, $J_n(kr)$ and $Y_n(kr)$ the n -th order Bessel functions of the first and the second kind, respectively. We note that for the case of a solid sphere $B_l = 0$, because $Y_n(kr)$ is infinite when $r \rightarrow 0$. Further, $P_{lm}(\cos \theta)$ is the Legendre function with the angular numbers l and n . We note, that n and m are integers with $l \geq 0$ and $-l \leq m \leq l$.

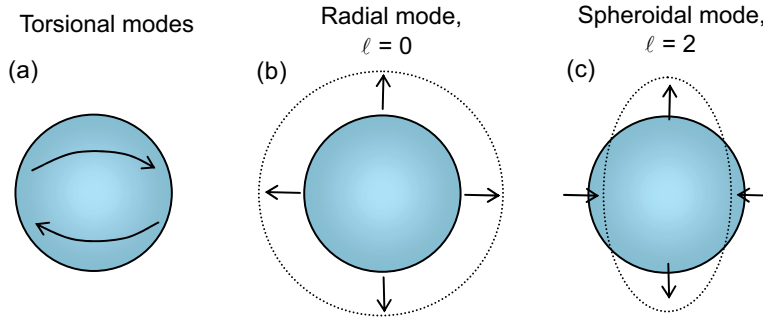


FIGURE 7.2 Sketch of (a) torsional, (b) radial, and (c) spheroidal vibration modes of a solid sphere.

Applying the free-boundary conditions at the interfaces, we arrive at the equations for the normal frequencies that can be found in the book of Eringen and Şuhubi [19].

7.4.1 Eigenfrequencies of a solid sphere

Vibrational modes of a solid sphere can be classified into two categories.

Torsional modes. These modes are purely transversal and have no radial displacement. All movements are purely tangential as shown in Fig. 7.2(a). The displacements of the torsional modes keep a constant volume and satisfy the condition $\nabla \cdot \mathbf{u} = 0$. We also note, that these modes are independent of c_l as apparent from Eq. (7.3). The eigenfrequencies of the torsional modes can be found from the equation

$$(l-1)j_l(h_t r_s) - h_t r_s j_{l+1}(h_t r_s) = 0 \quad (7.6)$$

with r_s the radius of the sphere and

$$j_l(kr) = \sqrt{\frac{\pi}{2kr}} J_{l+1/2}(kr). \quad (7.7)$$

Torsional modes exist only for $l \geq 1$ since for $l = 0$ Eq. (7.6) gives a trivial solution.

Radial and spheroidal modes. For the ground mode, $l = 0$, displacements are purely radial as shown in Fig. 7.2(b), and Eqs. (7.4) reduce to one simple equation

$$u_r = A_0 \frac{\partial j_0(h_l r)}{\partial r}. \quad (7.8)$$

Applying the conditions of zero stress on the surface of the sphere, we arrive at the transcendental equation

$$\frac{\tan(h_l r_s)}{h_l r_s} = \frac{1}{1 - (h_l r_s/2)^2}, \quad (7.9)$$

which yields the eigenfrequencies.

For $l \geq 1$ displacements have a mixed character of radial and tangential movements. One example of such vibrational modes is shown in Fig. 7.2(c) for $l = 2$. Here we see that the sphere contracts and elongates along a certain axis periodically transforming from sphere to ellipsoid. In this case the equation for the eigenfrequencies has the more complicated form

$$\begin{aligned} -\frac{1}{2} (h_l r_s)^2 \left[2l^2 - l - 1 - \frac{1}{2} (h_l r_s)^2 \right] j_l(h_l r_s) j_l(h_l r_s) \\ + \left[l^3 + 2l^2 - l - 2 - (h_l r_s)^2 \right] (h_l r_s) j_{l+1}(h_l r_s) j_l(h_l r_s) \\ + \left[l^2 + l^2 - 2l - \frac{1}{2} (h_l r_s)^2 \right] (h_l r_s) j_l(h_l r_s) j_{l+1}(h_l r_s) \\ + (2 - l^2 - l) (h_l r_s) (h_l r_s) j_{l+1}(h_l r_s) j_{l+1}(h_l r_s) = 0. \end{aligned} \quad (7.10)$$

7.4.2 Eigenfrequencies of a spherical shell

Displacements in a spherical shell with external and internal radii, r_1 and r_2 , respectively, can be expressed by the same functions as in the case of a solid sphere, but with different boundary conditions. In order to obtain the eigenfrequencies one needs to apply free boundary conditions at both sides of the shell. This problem was first solved by Lamb [17]. He also found that in case of a very thin shell, $(r_2 - r_1) \ll r_{1,2}$, the eigenfrequencies, generally, are non-zero and in first approximation independent of the thickness of the shell. In the following we assume that the shell is thin and $r_1 \approx r_2 = r_s$. Similar to the case of a solid sphere the fundamental modes of a spherical shell fall into two classes, namely torsional and spheroidal modes.

Torsional modes. The motion in torsion modes are fully tangential [see Fig. 7.3(a)] and growing in frequency with increasing the angular number l . The frequency spectrum is given by the expression

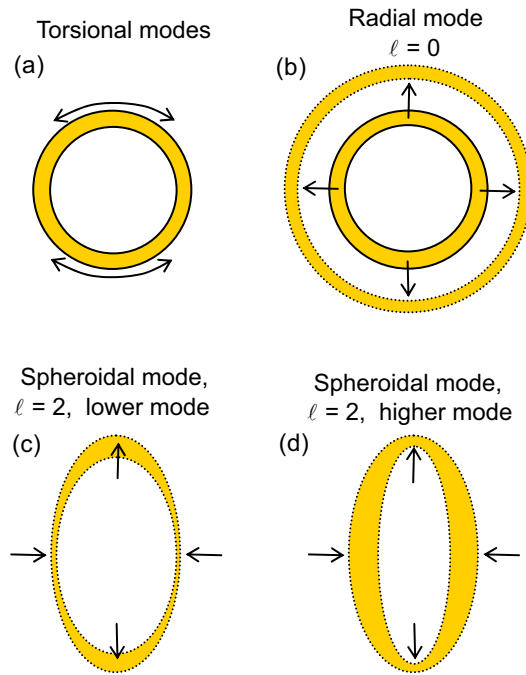


FIGURE 7.3 Sketch of (a) torsional, (b) radial, and (c) and (d) two types of spheroidal vibrational modes of a hollow spherical shell.

$$\Omega_l = h_t r_s \sqrt{(l-1)(l+2)}, \quad (7.11)$$

where r_s is the radius of the sphere. In contrast to the case of a solid sphere, the lowest mode appears for $l = 2$.

Radial and spheroidal modes. Similar to the case of a solid sphere, solutions for a hollow shell are different for the cases $l = 0$ and $l \neq 0$, respectively. The case $l = 0$ corresponds to a purely radial mode as shown in Fig. 7.3(b). The frequency of this mode is

$$\Omega_0 = 2h_t r_s \sqrt{\xi}, \quad (7.12)$$

where ξ reads

$$\xi = 3 - 2 \left(\frac{c_t}{c_l} \right)^2. \quad (7.13)$$

For $l \geq 1$ the displacements have both radial and transverse components. For each l , these modes have two branches with a spectrum given by

$$\Omega_{l\pm} = h_t r_s \sqrt{\frac{\zeta}{2} \pm \frac{1}{2} \sqrt{\zeta^2 - 16\xi(l^2 + l - 2)}}, \quad (7.14)$$

with $\zeta = (l^2 + l + 4)\xi + l^2 + l - 2$. These two branches have a quite different character. For $l = 1$ the high frequency root of Eq. (7.14) is $h_t r_s \sqrt{6\xi}$ while the lower one is zero, corresponding to a pure translation of the shell. For $l \geq 2$ both branches have a non-trivial solution. The lower and the higher modes for $l = 2$ are shown in Fig. 7.3. These modes correspond to a periodic elongation and contraction of the polar and equatorial diameters with opposite phases. For the mode corresponding to the lower root the tangential motion is directed towards the poles when the polar diameter is elongated, while for the high frequency mode the tangential motion is directed in the opposite direction. It is important to note that the frequency of the higher mode grows monotonically and infinitely with increasing l . In contrast, the lower which is finite obeys

$$\lim_{l \rightarrow +\infty} \Omega_{l-} = 2h_t r_s \sqrt{\frac{\xi}{1 + \xi}}. \quad (7.15)$$

We note, that around this frequency the density of the vibrational state is very high and produces a quasi-continuum spectrum. The lowest vibrational mode of a hollow shell is the lower $l = 2$ mode.

7.5 Ringing in a hollow sphere: selection rules.

Let us now consider what kind of Lamb mode can be responsible for the experimentally observed vibrations in the pump-probe experiment of Fig. 7.1. First of all, we note that heating induced by an optical excitation results in expansion and, hence, drives modes of the free shell that do not maintain a constant volume. Therefore, we have to exclude the pure torsional modes. Further, we can show that the heat induced by the optical excitation of a homogeneous sphere can excite exclusively the modes with even l (including $l = 0$). The photon energy of the excitation, in our case, is below the energies of the interband transitions in gold. Therefore, we can safely assume that the heat is induced via surface plasmon excitation, i.e. via dipole, quadrupole and, perhaps, higher multipoles. For the sake of simplicity we assume that the excitation is dipolar. The dipolar excitation

will induce a rapidly oscillating electron current on the surface of the shell with an electron current density having inversion symmetry. We note that the same applies for higher multipole excitation. According to Ohm's law, the dissipation and, for that matter, the induced stress in the metallic shell is proportional to the square of the current, and the inversion symmetry of the current distribution excludes excitation of an even- l Lamb modes. This selection rule was first formulated by Duval for far-infrared and Raman transitions of a solid sphere [20]. Of all even- l modes, the most important ones are expected to be the $l = 0$ and the $l = 2$ modes because they possess the highest symmetry.

Although, the selection rules for Raman scattering and pump-probe excitation are identical there is a striking difference in the experiments. In Raman experiments the most active mode has $l = 2$, while the $l = 0$ -mode is difficult to observe [2, 3] and has only recently been revealed [1, 21]. In contrast, in pump-probe experiments with spherically symmetric particles only $l = 0$ was observed [5–8, 10, 11]. The reason of these paradoxical discrepancy lays in different conditions of excitations [22]. Indeed, in Raman scattering measurements the excitation is thermal and all modes are occupied according to the Planckian distribution. Since Raman scattering is primarily sensitive to dipolar plasmon coupling with the modulation of the surface charges induced by a quadrupole vibration ($l = 2$) of the sphere, the $l = 2$ peak prevails. In contrast, in pump-probe experiments, the excitation is impulsive and after a short time (much shorter than the period of acoustic oscillation) electrons are expected to reach an equilibrium distribution in the entire volume of the metal shell. As a result, the $l = 0$ mode is predominantly excited.

In Table 7.2 we present the calculated values of the Lamb mode for an isolated solid silica core with a radius $r_1 = 228$ nm and an isolated hollow gold shell with an average radius $(r_1 + r_2)/2 = 247$ nm. For our calculations of the Lamb modes on a gold shell, we used the approximation of a thin shell, which is valid because $r_2 \gg (r_2 - r_1)$. Further, in the calculations for the silica core and the gold shell with the free-boundary condition, we used the longitudinal and transverse sound velocities for gold of $c_l = 3240$ m/s and $c_t = 1200$ m/s, respectively, and for silica $c_l = 5970$ m/s and $c_t = 3760$ m/s, respectively. The results of the calculations show that the Lamb oscillations of the solid silica core are all too fast to explain the experiments. For the hollow gold shell, however, the calculated period for the $l = 0$ mode ($T = 392$ ps) is remarkably close to experiment $T = 390$ ps, while the lower $l = 2$ mode is even too slow. Taking into account a 5-% spread in the measured period at different locations on the sample, we arrive at the conclusion that agreement between the calculated $l = 0$ mode and the experiment is remarkable. Although, it may look surprising that the model, which does not take into account

Mode	Period of oscillations, ps	
	Silica core (solid sphere) $R = 228$ nm	Gold sphere (hollow sphere) $R = 247$ nm
$\ell = 0$	100	392
$\ell = 2$	145	1060 and 237
Experiment	390 ± 20	

TABLE 7.2 Calculated periods of Lamb modes for 228-nm silica core and 247-nm gold hollow shell for $l = 0$ and $l = 2$. The last row shows the experimental value for comparison.

the internal core, produces such good agreement with experiment, we note that this model is equally valid in the case of poor mechanical contact between silica and gold, which is very likely because gold and silica possess very different temperature expansion coefficients and apparently easily lose mechanical contact by drying and during repeated heating and cooling cycles. We note, that similar observations were recently reported by Portales and co-workers in [4]. They studied resonant Raman scattering from nickel-silver core-shell particles and found that their spectra can be explained quantitatively just by a free vibration of the silver shell, i.e. assuming stress-free internal boundary condition with the core. In contrast to our measurement, their oscillation frequency corresponds to the $l = 2$ mode that is, as we explained above, however, not excited in our pump-probe experiment.

The picture of the subnanosecond dynamics is now complete: our ultrashort optical pulse excites electrons that reach a high-temperature equilibrium distribution within a picosecond (see Chapter 6). By virtue of their high velocity free electrons quickly homogenize around the gold shell. Within several picoseconds the electron gas further equilibrates with the lattice, generating phonons that induce a homogeneous stress in the gold shell and impulsively excite the ground Lamb mode of the isolated hollow shell.

Our explanation is also in agreement with the observed zero phase of the optical oscillations (see Table 7.1). Indeed, under our experimental conditions the

equilibration of electrons and lattice occurs within several picoseconds (see Chapter 6), i.e. much faster than the oscillation period. In our experimental conditions, we did not observe any evidence of hot-electron pressure driving the vibration as reported by Perner and co-workers [9].

If in our case the nonhomogeneously distributed hot electrons had driven the vibration directly they would have excited predominantly non-spherically-symmetric modes (e.g. $l = 2$), which were not observed. In contrast, vibrations of ellipsoidal particles have no spherically-symmetric modes and hot electrons may even couple with the ground mode. This results in a phase shift of the vibrational oscillations as was observed by Perner.

7.6 Nature of the optical response

Now, having established the selection rules, how can we explain quantitatively the changes in the reflectivity induced by excited Lamb modes? The first obvious effect, that we have to consider, is the sensitivity of the dielectric constant of gold to compression and dilatation. Indeed, significant oscillations of the transient reflectivity have been registered only at those wavelengths that have a sizeable slope in the reflectivity spectrum. This suggests that the changes in the real part of the dielectric constant of gold shifts the position of the plasmon resonances and converts vibrations into modulations of the optical reflectivity.

In the infrared part of the spectrum where our vibrational signals are the strongest, we can neglect the influence of intraband transitions in gold and may consider only the free-electron Drude contributions. The real part of the intraband dielectric constant $\varepsilon'_{ib} = \text{Re}(\varepsilon_{ib})$ reads

$$\varepsilon'_{ib}(\omega) = 1 - \frac{\omega_p^2}{\omega^2 - \Gamma^2}. \quad (7.16)$$

Here, ω is the optical frequency, Γ the damping constant for free electrons [23], and ω_p the plasma frequency given by

$$\omega_p = \sqrt{\frac{ne^2}{\varepsilon_0 m_e}}, \quad (7.17)$$

with n the electron density, m_e the electron effective mass, ε_0 the permittivity of vacuum, and e the electron charge.

The amplitude of the gold-shell expansion can be estimated by the expression

$$\frac{\Delta r_s}{r_s} \approx 2\alpha_T \Delta T_l, \quad (7.18)$$

where α_T is the linear thermal expansion coefficient, r_s is the radius of the gold shell, and ΔT_l is the ultrafast rise in lattice temperature induced by optical excitation. Since the changes are small, the relative volume expansion $\Delta V/V$ of the volume V of the gold shell reads

$$\frac{\Delta V}{V} \approx 6\alpha_T \Delta T_l. \quad (7.19)$$

Noting that n is inversely proportional to the volume, the relative decrease in electron concentration equals $\Delta n/n = -\Delta V/V$. Combining Eqs. (7.16), (7.17), and (7.19), we obtain

$$\frac{\Delta \varepsilon'_{ib}(\omega, \Delta T_l)}{\varepsilon'_{ib}(\omega)} \approx 6\alpha_T \Delta T_l. \quad (7.20)$$

Inserting $\alpha_T = 1.42 \times 10^{-5} \text{ K}^{-1}$ [24] and $\Delta T_l = 225 \text{ K}$ (see Chapter 6) we arrive at $\Delta \varepsilon'_{ib}/\varepsilon'_{ib} = 1.9 \times 10^{-2}$. The resulting shift of the spectral position of the quadrupole plasmon resonance, λ_p , can be estimated as [7]

$$\frac{\Delta \lambda_p}{\lambda_p} = \sqrt{\frac{\Delta \varepsilon'}{\varepsilon'}} \approx \frac{1}{2} \frac{\Delta \varepsilon'}{\varepsilon'}. \quad (7.21)$$

Hence, the change in reflectivity at the wavelength λ can be expressed in terms of the differential reflectivity $\partial R/\partial \lambda$ as

$$\frac{\Delta R}{R} = -\frac{1}{2} \frac{\Delta \varepsilon}{\varepsilon} \frac{\partial R}{\partial \lambda} \lambda. \quad (7.22)$$

For $\lambda = 700 \text{ nm}$, we insert $\partial R/\partial \lambda = -0.023 \text{ nm}^{-1}$ taken from the linear spectrum in Fig. 5.6(a) and find $\Delta R/R \approx 0.15$, which is one order of magnitude higher than experimental value of 0.01 (see Table 7.1). In spite of the overestimation of the absolute values our estimate correctly explains the sign of the oscillations. Indeed, for $\lambda = 950 \text{ nm}$ the slope of the reflectivity observed in the linear spectra is positive, $\partial R/\partial \lambda > 0$, that implies that $\Delta R/R$ should be negative, as observed ($\Delta R/R = -0.04$, see Table 7.1).

7.7 Origin of the damping of acoustic vibrations

We now examine the possible origins of the observed damping of the acoustic vibrations. First of all, we calculate the free-induction decay of an inhomogeneous distribution of oscillation frequencies due to the variation in the size of the gold shell. We assume that the particles are normally distributed with a standard deviation σ_r . Then the transient reflectivity can be expressed as

$$\frac{\Delta R}{R} = \frac{1}{\sqrt{2\pi}\sigma_r} \int_0^{\infty} \exp\left[-\left(\frac{r_s - \bar{r}_s}{\sqrt{2}\sigma_r}\right)^2\right] \cos[\Omega(r_s)t] dr_s, \quad (7.23)$$

where \bar{r}_s is an average radius of the gold shell and $\Omega(r_s)$ the frequency of the oscillations, also dependent on the size of the sphere. In our case $\sigma_r/\bar{r}_s \ll 1$ and Eq. (7.23) yields

$$\frac{\Delta R}{R} = \cos(\bar{\Omega}t) \exp\left(-\frac{t^2}{\tau_{df}^2}\right). \quad (7.24)$$

Here, $\bar{\Omega} = 2\pi/\bar{T}$ is the mean oscillation frequency corresponding to the mean radius of the gold shells and

$$\tau_{df} = \frac{\bar{r}_s \bar{T}}{\sqrt{2}\pi\sigma_r}. \quad (7.25)$$

Inserting $\bar{T} = 390$ ps and $\sigma_r/\bar{r}_s = 0.05$ taken from the experimentally observed distribution of \bar{T} (see Table 7.1) and also known from the SEM data we compute $\tau_{df} = 1.75$ ns, which is three times longer than the experimentally observed decay 0.6 ns.

Additional damping may occur thanks to energy transfer to the silica core [6, 25], which, however, is hard to estimate because the degree of mechanical contact between shell and core is unknown. Additionally, the decay of oscillation can be caused by electron-phonon interaction. It is known that electron-phonon interaction results in significant attenuation of gigahertz acoustic wave in metals. The reason is oscillations of the Fermi-level that induce an electric current [26]. In our case electron current appears between the domains of the polycrystalline gold shell because acoustic wave shifts their Fermi-levels. The current acts as friction and converts the energy of the oscillation into heat. We also mention that the ground mode oscillation, of course, can funnel energy to other modes via anharmonic decay.

Finally, we note that similar to the observations of Courty and co-workers made in self-organized silver nanocrystals [1], we found no influence of the regular ordering on the vibration spectrum of the gold shell.

7.8 Conclusions and perspectives

In this Chapter we analyzed the subnanosecond dynamics of the transient reflectivity of a photonic crystal composed of a silica-core thin gold-shell particles. The transient reflectivity exhibits pronounced oscillations with a period of 390 ps with an amplitude as high as 4% of the total reflectivity. These oscillations are caused by a coherent vibration of the gold-shell diameter. The frequency of the acoustic vibration has been shown to be in excellent agreement with a model assuming free boundary conditions on both sides of the shell. This situation corresponds to a poor contact between the silica core and the gold shell.

In our experiment we observed exclusively the ground vibrational mode ($l = 0$) corresponding to a pure radial expansion and contraction of the gold shell. However, we suppose that the lowest frequency quadrupole mode ($l = 2$) can be observed in a Raman spectroscopy. We note, that this mode was recently observed in a Raman scattering experiment in the case of nickel-silver core-shell nanoparticles [4]. In our sample this mode should appear with a 2.5-GHz shift from the laser line, which can be an interesting point for future investigations. Observation of this mode will be a good test for our model of free gold shell loosely bound to a silica core.

References

- [1] A. Courty, I. Lisiecki, and M. P. Pileni, *J. Chem. Phys.* **116**, 8074 (2002).
- [2] E. Duval, A. Boukenter, and B. Champagnon, *Phys. Rev. Lett.* **56**, 2052 (1986).
- [3] M. Fujii, Y. Kanzawa, S. Hayashi, and K. Yamamoto, *Phys. Rev. B* **54**, R8373 (1996).
- [4] H. Portales, L. Saviot, E. Duval, M. Gaudry, E. Cottancin, M. Pellarin, J. Lermé, and M. Broyer, *Phys. Rev. B* **65**, 165422 (2002).
- [5] J. H. Hodak, A. Henglein, and G. V. Hartland, *J. Chem. Phys.* **111**, 8613 (1999).
- [6] Y. Hamanaka, J. Kuwabata, I. Tanahashi, S. Omi, and A. Nakamura, *Phys. Rev. B* **63**, 104302 (2001).
- [7] G. V. Hartland, *J. Chem. Phys.* **106**, 8048 (2002).
- [8] M. Nisoli, S. D. Silvestri, A. Cavalleri, A. M. Malvezzi, A. Stella, G. Lanzani, P. Cheyssac, and R. Kofman, *Phys. Rev. B* **55**, R13424 (1997).

-
- [9] M. Perner, S. Gresillon, J. Marz, G. von Plessen, J. Feldmann, J. Porstendorfer, K.-J. Berg, and G. Berg, *Phys. Rev. Lett.* **85**, 792 (2000).
- [10] G. V. Hartland, M. Hu, O. Wilson, P. Mulvaney, and J. E. Sader, *J. Phys. Chem. B* **106**, 743 (2002).
- [11] J. H. Hodak, A. Henglein, and G. V. Hartland, *J. Phys. Chem. B* **104**, 9954 (2000).
- [12] J. H. Hodak, A. Henglein, and G. V. Hartland, *J. Phys. Chem. B* **104**, 5053 (2000).
- [13] C. Graf, D. L. J. Vossen, A. Imhof, and A. van Blaaderen, *Langmuir* **19**, 6693 (2003).
- [14] S. D. Poisson, *Mém. de le Acad. (Paris)* **8**, 357 (1829).
- [15] P. Jaerish, *Creele J. Math.* **88**, 131 (1880).
- [16] H. Lamb, *Proc. Lond. Math. Soc.* **13**, 51 (1881).
- [17] H. Lamb, *Proc. Lond. Math. Soc.* **14**, 50 (1882).
- [18] A. E. H. Love, *A treatise on the mathematical theory of elasticity* (Dover, New York, 1944).
- [19] A. C. Eringen and E. S. Şuhubi, *Elastodynamic*, vol. 2 (Academic press, New York, 1975).
- [20] E. Duval, *Phys. Rev. B* **46**, 5795 (1992).
- [21] H. Portales, L. Saviot, E. Duval, M. Fujii, S. Hayashi, N. D. Fatti, and F. Vallée, *J. Chem. Phys.* **115**, 3444 (2001).
- [22] G. Bachelier and A. Mlayah, *Phys. Rev. B* **69**, 205408 (2004).
- [23] U. Kreibig and M. Vollmer, *Optical properties of metall clusters* (Springer-Verlag, Berlin, 1995).
- [24] J. S. Touloukian, *Thermal expansion: metallic elements and alloys*, vol. 12 of *Thermophysical properties of matter* (Plenum, New-York, 1975).
- [25] N. D. Fatti, C. Voisin, D. Christofilos, F. Vallée, and C. Flytzanis, *J. Phys. Chem. A* **105**, 4321 (2000).
- [26] J. W. Tucker and V. W. Rampton, *Microwave Ultrasonics in Solid State Physics* (North-Holland, Amsterdam, 1972), p. 302.

SAMENVATTING

Dit proefschrift beschrijft een experimentele studie van de lineaire en niet-lineaire optische eigenschappen van zogenaamde fotonische kristallen: materialen met een periodieke variatie van de brekingsindex in de ruimte. Fotonische kristallen zijn ontworpen om de voortplanting van licht te beïnvloeden door middel van meervoudige verstrooiing. Hoewel het lichtveld in een dergelijke structuur strikt genomen niet is gekwantiseerd en eenvoudig met de vergelijking van Maxwell kan worden beschreven, wordt niettemin gesproken over fotonische kristallen. In de afgelopen tien jaar is de interesse in de studie van fotonische kristallen exponentieel gegroeid, vanwege hun opmerkelijke optische eigenschappen. In het bijzonder treedt in deze structuren een stop-band op voor licht wat zich in bepaalde richtingen voortplant, als de golflengte bijna gelijk is aan de periode van de modulatie in brekingsindex. In sommige gevallen hebben driedimensionale fotonische kristallen zelfs een complete stop-band, een bandkloof, waarin licht zich in geen enkele richting kan voortplanten. Dit betekent dat licht in het spectrale bereik van de fotonische band-gap totaal zal worden gereflecteerd. Een ander interessant optisch fenomeen treedt op als er een trilholtje in het fotonische kristal is uitgespaard. Doordat de voortplanting van licht in het omringende fotonische kristal niet mogelijk is, kan het licht niet uit de holte ontsnappen en zit gevangen. Dit kan zorgen voor spectaculaire veranderingen in de stralingseigenschappen van het medium. Spontane emissie zou bijvoorbeeld helemaal onmogelijk zijn in het spectrale bereik van de fotonische band kloof. Deze eigenschappen zijn uniek en kunnen niet in andere materialen gevonden worden.

Een van de doelen van het onderzoek in fotonica is het ontwerpen van optische componenten gebaseerd op fotonische kristallen, waarin fotonen een vergelijkbare functie hebben als elektronen in traditionele elektronica, maar dan veel sneller. Fotonen kunnen worden gestuurd en gecontroleerd op een vergelijkbare manier als elektronen in halfgeleidercomponenten. In het bijzonder maken

dergelijke optische componenten het mogelijk om geïntegreerde optische circuits te bouwen. In zulke optische circuits zullen halfgeleiderlasers de rol spelen van de elektrische stroombron en kunnen golfgeleiders het licht transporteren zoals een draad de elektronen transporteert. Het licht kan zelfs worden verzameld in trilholttes in het fotonische kristal om fotonische LC-kringen te realiseren en terwijl absorberende materialen kunnen worden gebruikt als weerstanden. De belangrijkste elementen van geïntegreerde circuits zijn natuurlijk transistoren, elektrische schakelaars. *Optisch* schakelen kan worden bereikt met behulp van niet-lineaire optica. Om dit optisch schakelen te bereiken in fotonische kristallen is een begrip en nauwkeurige controle van de ultrasnelle niet-lineaire eigenschappen een vereiste. In dit proefschrift wordt een analyse gegeven van de optische respons in verschillende regimes, in verschillende typen driedimensionale fotonische kristallen, en op tijdschalen van femto- tot picoseconden (10^{-15} – 10^{-12}). Het blijkt dat de dynamische veranderingen in de reflectie aan een driedimensionaal fotonisch kristal groot en snel kan worden gemaakt.

Het idee van optisch schakelen kan als volgt worden uitgelegd: een ultrasnelle optische puls slaat een fotonische kristal aan, waardoor de complexe diëlectrische constante verandert en de reflectie aan het kristal wordt aangepast. Een verandering in het imaginaire deel van de diëlectrische constante onderdrukt interferentie in het fotonische kristal en verandert de amplitude van de reflectie. Een verandering in het reële deel van de dielectrische constante echter verschuift de spectrale positie van de fotonische stop band. Beide effecten worden in dit proefschrift beschreven. Het eerste type schakelaar is gemaakt van een opaal, gevuld met amorf silicium. Het sample bestaat uit een dicht-gepakt vlakgecentreerd rooster van silica balletjes met een diameter van 230 nm. De holttes in deze opalen werden gevuld met silicium. In dit kristal wordt schakelen bereikt door gebruik te maken van de niet-lineaire eigenschappen van het silicium. Wij beschrijven hoe een optische puls de elektronen en gaten in het silicium aanslaat. Deze aangeslagen ladingsdragers vormen een plasma en verhogen daardoor de absorptie. Dientengevolge wordt de constructieve interferentie van meervoudig verstrooid licht in het opaal onderdrukt en vermindert de Bragg reflectie. Dit proces gebeurt zeer snel en wordt slechts beperkt door de duur van de optische excitatie puls. In het experiment in dit proefschrift zijn schakeltijden van 30 femtoseconde waargenomen, en dat gepaard gaande met een verandering van de relatieve amplitude van meer dan 50%, veel hoger dan in optische schakelaar van “gewoon” amorf silicium.

Het is belangrijk om onderscheid te maken tussen twee bijdragen aan de reflectie aan de opalen: de coherente verstrooiing aan het periodieke rooster (Bragg

diffRACTIE) en rest-verstrooiing aan de lucht-opaal overgang. De niet-lineaire eigenschappen van deze twee bijdragen zijn apart onderzocht in twee experimenten. In het eerste experiment werd de “speculaire” bundel geblokkeerd zodat alleen het Bragg-gereflecteerde licht werd opgevangen en geanalyseerd. In het tweede experiment werd een klein diafragma in de detectiebundel geplaatst om het Bragglicht tegen te houden. Het is opmerkelijk dat de verandering van de BraggdiffRACTIE 10 keer groter was dan de verandering in de speculare reflectie. Dit resultaat bleek in goede overeenstemming met de theorie. Dit demonstreert de intrinsieke versterking van niet-lineaire effecten in fotonische kristallen.

Een tweede manier om te schakelen werd aangetoond in een opaal gevuld met vanadium-dioxide. Het is bekend dat vanadium-dioxide een structurele faseovergang ondergaat bij een temperatuur van 68°C. Bij temperaturen onder het transitiepunt is het materiaal een halfgeleider, erboven een metaal. Het is belangrijk dat het reële deel van de dielectrische constante van vanadium-dioxide in deze twee toestanden veel verschillen. Het is dit feit wat we hebben gebruikt om de tweede manier van optische schakelen te demonstreren. In ons experiment wordt de faseovergang tot stand gebracht met behulp van een intense optische puls. Het blijkt dat de faseovergang in slechts enkele honderden femtoseconden plaatsvindt. Als gevolg hiervan verschuift de fotonische stopband binnen 350 femtoseconden naar het blauw, waardoor de reflectie sterk verandert. Het herstel vindt plaats op een tijdschaal van microseconden en wordt bepaald door het afkoelen van het geëxciteerde materiaal.

Een compleet nieuw type fotonische kristallen, de zogenaamde *metallo-diëlectrische* fotonische kristallen, bieden nog meer mogelijkheden om de fotonische band te er stemmen. Deze structuren hebben oppervlakte plasmonresonanties die in feite collectieve oscillaties van het elektronen gas zijn. De lineaire en niet-lineaire optische eigenschappen van deze structuren zijn in dit proefschrift beschreven. We hebben de lineaire eigenschappen geanalyseerd van een fotonische kristal wat bestaat uit periodiek geordende deeltjes met een meervoudige schil, bestaande uit een silica kern met een straal van 228 nm, bedekt met een dunne gouden schil en dunne silica schil, met diktes van respectievelijk 38 en 10 nm. Dit fotonische kristal van “nano-uien” levert spectaculaire optische fenomenen op. Licht wat aan deze structuur wordt gereflecteerd, produceert bijvoorbeeld onverwachte licht bundeltjes in richtingen met een hexagonale symmetrie en een verstrooiingshoek tophoek van slechts 8°. Deze hoek is te klein om toegeschreven te worden aan simple diffRACTIE aan een periodiek rooster van deze nano-uien, maar kan worden uitgelegd door interferentie tussen oppervlakte plasmonen en oppervlakte golven te beschouwen.

In het visuele gebied blijkt het reflectie spectrum van het goud-schil fotonische kristal te worden bepaald door de oppervlakte plasmonresonanties. Het is interessant dat deze resonanties kunnen worden beïnvloed op een femtoseconde tijdschaal. Een optische puls kan het elektronengas in goud tot duizenden Kelvins verhitten, wat de dielectrische constante op een femtoseconde schaal kan doen veranderen. Afhankelijk van de golflengte kunnen zowel, bleking en absorptie worden geobserveerd in onze structuren. De dynamica van het herstel duurt meerdere picoseconden (10^{-12} s) en wordt bepaald door het energietransport van het elektron gas naar het rooster. Ook hier is het schakelen zeer efficiënt. We kunnen veranderingen in reflectie bereiken van 35% bij een excitatie-vermogen van 0.5-mW/cm^2 , dat 20 keer lager is dan nodig om vergelijkbare veranderingen te bereiken in opaal-silicium en opaal-vanadium-dioxide composieten.

Als laatste beschrijven we een heel ander schakelmechanisme, wat geïnduceerd wordt door coherente akoestische radiële vibraties van de nanogoudschillen, in andere woorden, periodieke compressie en uitrekking. Deze oscillaties worden Lamb-vibraties genoemd, maar zijn tot nu toe nooit in nanometer-schillen gezien. Door mechanische oscillaties ontstaan vergelijkbare veranderingen in reflectie als door hete elektronen. De geobserveerde oscillatie eigenschappen van onze nanogoudschillen komen goed overeen met berekeningen. Dit experiment kan een brug slaan tussen fotonische en zogenaamde fononische kristallen, periodieke media voor akoestische golven, waarin bandkloven bestaan voor akoestische golven.

Dit proefschrift beschrijft een paar eerste stappen in de richting van complete ultrasnelle controle over de voortplanting van licht in fotonische kristallen en de toepassing hiervan in bijvoorbeeld optische schakelaars, optisch geheugens, lage-drempel lasers, holografische geheugens, configureerbare optische netwerken en optische computers.

ACKNOWLEDGEMENTS

At the end of 1998 we, members of the Solid State Department in the Ioffe Institute, gathered for a New Year party. As part of the amusing program there was a quiz with an important prize for the winner – a barrel of beer. One of the questions was: “Which magic crystal brings Russian scientists abroad?” Curiously enough, the one of us who, in fact, already went to the West driven by research on such crystals, did not find the right answer! At that time I did not take the magic power seriously. However, I was intrigued by the question and decided to remember it. Shortly thereafter, I was the one to go to the West, driven by the goal to study magic crystals.

My first thanks I would like to address to my supervisor, Prof. Dr. Jaap Dijkhuis. My research would have been stuck without his enthusiastic support and confidence in success of the project even in desperate situations. His challenging ideas and ability to find non-standard solution of problems amazed me already from my first minutes in the Netherlands (he transported me to the University by bicycle!). Quite important was Jaap’s ability to feel what is “possible” and what is “impossible” that made me just in time stop my walk on the wrong road. I really appreciate our discussions supplying me with new ideas, which resulted, in the end, in nice publications. I also thank my former supervisor Prof. Dr. Andrey Akimov for his great help in my studies in St.Petersburg. In fact, his proposal to use opal-silicon composite was crucial and pushed my research forward.

My studies would not have been successful without the technical support from Cees de Kok, Paul Jurrius, and Frans Wollenberg. It was fantastic to work with them not only because of their adequate help with handling the equipment but also by their sense of humor. Especially, the months of fighting with our Femtosource laser under the general command of Cees are truly unforgettable.

I have had quite interesting discussions with Otto Muskens, who also sometimes helped me with small experimental problems. He also made some calcu-

lations of the dielectric constant of gold for different temperatures that I used in Chapter 6. Otto, thank you also for sharing our journey around New Zealand.

It is my pleasure to thank Cristina Graf and Dmitry Kurdyukov who fabricated samples for my research. Cristina, I know how difficult it was to fabricate your unique sample! I would like to acknowledge the fruitful collaboration with Dr. Alexander Moroz and Dr. A.V. Sel'kin who made some calculations, which became important supplements to the experimental data and allows us to make an important publication. Further, I thank Prof. Dr. Alfons van Blaaderen for fruitful discussions, long-term collaboration, careful reading of manuscripts, and several important advices. I also acknowledge Dr. A. B. Pevtsov who shared with me his data on linear properties of opal-Si and opal-VO₂ composites and gave me several useful advices. I appreciate Prof. Dr. A. A. Kaplyanskii for his attention, together with Prof. Dr. V. G. Golubev and my other co-authors from the Ioffe Institute for careful reading of manuscripts.

The list of my colleagues contributing to this thesis can not be complete without mentioning another six persons. First of all I would like to thank my students: Robert Kerst who developed a pump-probe setup and achieved important results in experiments with opal-VO₂ during his “groot onderzoek” and Johan Stiefelhaagen who performed a wonderful research during his “klein onderzoek”, X. Shan is acknowledged for her help with the acoustic experiments of Chapter 7. Quite important help I received from Carlos van Kats and Job Thijssen who performed the SEM measurements. Carlos and Job, thank you! Also special thanks I would like to address to Dries who translate the “Samenvatting” in Dutch.

It is my pleasure to thank Dr. Prof. Andries Meijerink for loaning the CCD. Without this device it would have been impossible performing the experiments of Chapters 5, 6, and 7. I also appreciate help from Pieter and Bert.

Further, Prof. Dr. Jaap Dijkhuis and Dmitry Turchinovich made a hard job by checking spelling and grammar in this thesis, suffering from my “*the*’s” and “*a*’s”. I also thank Prof. Dr. Albert Polman for his interest to my work (I am sorry that I did not manage to study his sample). Svetlana Chakhina is acknowledged for designing the cover of this thesis.

I thank Clarin Derks for assisting in secretary affairs. Working in the lab would be boring without the nice people surrounding me and I enjoyed the time shared with Jeroen, Otto, Lennart, Shan, Peter, Robert, Johan, Erik, Inge, Dries, Driss, Carolijn, Erik, Michel, Richard, and, of course, Sivaji both in the coffee-room and some-times in a bar.

In addition to this, there are quite a few very friendly and helpful colleagues from the others groups of the Department of Physics and Astronomy, which make

the University life highly enjoyable. I like to give my best regards to Krasi, Didi, Cristina Christova, Elena, and Masha. I special regards to Panos who has disclosed Utrecht for me during my first weeks in the Netherlands. In spite the fact that he left Utrecht University about four years ago, we are still friends. Another thanks I address to Marcel, who showed me another side of Amsterdam. I enjoy acknowledge two friends and colleagues of mine, Kostya and Slava, who were always ready to give me advises in mathematics, computers, and in life being.

I am also very much appreciate the time I shared with XuQuan. I would also like to thank Tony Hearn for organizing ING meetings where foreign students are able to meet each other. During these 4 years I have met many interesting people from different countries: Kostas, Alberto, Maki, Claudette, Ruža, Zuzana, Edita, Wojtek, Alice, Manuela, Ruben, Pilar, Vivian, Reza, Davido, Mika, Peka, Agneska, Stephen, as well as my Russian friends Yura, Olga, Sergej, Roma, Zhenya, Alexej and many, many others.

At the end I would like again to acknowledge all my colleagues and friends for their support and I hope we will meet each other very soon.

This Ph. D. study has been supported by Breedtestrategieproject of the Debye Institute and University of Utrecht “The Physics of Colloidal Matter”.

LIST OF PUBLICATIONS AND CONFERENCE VISITS

This thesis is partly based on the following publications:

1. D. A. Mazurenko, A. V. Akimov, A. B. Pevtsov, D. A. Kurdyukov, V. G. Golubev, and J. I. Dijkhuis, *Ultrafast switching in Si-embedded opals*, Physica E **17**, 410-413 (2003) – Chapter 3.
2. D. A. Mazurenko, R. Kerst, J. I. Dijkhuis, A. V. Akimov, V. G. Golubev, D. A. Kurdyukov, A. B. Pevtsov, and A. V. Sel'kin, *Ultrafast optical switching in three-dimensional photonic crystals*, Phys. Rev. Lett. **91**, 213903 (2003) – Chapter 3.
3. D. A. Mazurenko, A. V. Akimov, A. B. Pevtsov, D. A. Kurdyukov, V. G. Golubev, and J. I. Dijkhuis, *Ultrafast all-optical switching in a three-dimensional photonic crystal*, J. Lumin. **108**, 163-166 (2004) – Chapter 3.
4. D. A. Mazurenko, R. Kerst, A. V. Akimov, A. B. Pevtsov, D. A. Kurdyukov, V. G. Golubev, A. V. Sel'kin, and J. I. Dijkhuis, *Femtosecond Bragg switching in opal-a-nc-Si photonic crystals*, J. Non-Cryst. Solids **338-340**, 215-217 (2004) – Chapter 3.
5. D. A. Mazurenko, A. Moroz, C. M. Graf, A. van Blaaderen, and J. I. Dijkhuis, *Three-dimensional silica-gold core-shell photonic crystal: linear reflection and ultrafast non-linear optical properties* in *Photonic Crystal Materials and Nanostructures*, edited by R. M. de la Rue, P. Viktorovitch, C. M. Sotomayor-Torres, and M. Midrio (2004), vol. **5450** of Proc. SPIE, pp. 669-577 – Chapters 5 and 6.
6. D. A. Mazurenko, A. V. Akimov, V. G. Golubev, D. A. Kurdyukov, A. B. Pevtsov, R. Kerst, and J. I. Dijkhuis, *Ultrafast Bragg switching induced by a phase transition in a 3D photonic crystal* in *Photonic Crystal*

Materials and Nanostructures, edited by R. M. de la Rue, P. Viktorovitch, C. M. Sotomayor-Torres, and M. Midrio (2004), vol. **5450** of Proc. SPIE, pp. 250-259 – Chapter 4.

7. D. A. Mazurenko, R. Kerst, J. I. Dijkhuis, A. V. Akimov, V. G. Golubev, A. A. Kaplyanskii, D. A. Kurdyukov, A. B. Pevtsov, *Subpicosecond shifting of the photonic band gap in a three-dimensional photonic crystal*, Submitted to Appl. Phys. Lett. – Chapter 4.

Parts of the research described in this thesis have been presented on the following international conferences:

1. *ICSNN 2002*, International Conference on Superlattices Nano-Structures and Nano-Devices, 21-26 July 2002, Toulouse, France.
2. *Nanostructures Physics and Technology*, 23-28 June 2003, St. Petersburg, Russia.
3. *DPC'03*. International Conference on Dynamical Processes in Excited States of Solids, 3-8 August 2003, Christchurch, New Zealand.
4. *ICAMS'20*, 20th International Conference on Amorphous and Microcrystalline Semiconductors: Science and Technology, 25-29 August 2003, Campos do Jordão, Brazil.
5. VI Russian Conference on Semiconductors, 27-31 October 2003, St. Petersburg, Russia. (*Invited*).
6. *Photonics in Europe 2004*, Photonic Crystal Materials and Nanostructures, 27-29 April 2004, Strasbourg, France.
7. *Phonons 2004*, 11th International Conference on Phonon Scattering in Condensed Matter, 25-30 July 2004, St. Petersburg, Russia.

Further, parts of this work have been presented on local events: annual meetings of the FOM “Wetenschappelijke vergadering voor de Gecondenseerde Materie”, Veldhoven (2002) and (2003), during the *Do!-days*, 24 March (2003), Noordwijkerhout, and at the University of Groningen (2004).

CURRICULUM VITAE

The author of this thesis was born on 26 January 1974 in Leningrad, Soviet Union. After graduating from the Lyceum of Mathematics and Physics #239, Leningrad in 1991 he entered the Electrotechnical Institute of Leningrad, which was renamed as St. Petersburg Electrotechnical University in the same year. During his University studies the author has participated in scientific research at the Ioffe Physico-Technical Institute in St. Petersburg, first in the group headed by Dr. A. M. Mintairov and latter in the group of Prof. A. A. Kaplyanskii and Dr. A. A. Akimov. After graduating from the Electrotechnical University in 1997, the author continued his research as a post-graduated student in the same team, where the research was focused on phonon-assisted tunnelling in single and double quantum wells, collective properties and phase transitions of exciton gases in double quantum wells, and luminescence of quantum dots. The results of this research were published in 6 journal papers . Unfortunately, due to serious financial problems which were aggravated in the late 1990's, it was impossible for author to pursue his further research in Russia. Thanks to the invitation of Prof. J. I. Dijkhuis, the author started in 2000 his Ph. D. research in a group of "Atom Optics and Ultrafast Dynamic" as a part of the "Breedtestrategieprogramma" of the Debye Institute and the University of Utrecht. This thesis represents the author's accomplishments during 4 years' research period in Utrecht.